Charles University in Prague

Faculty of Mathematics and Physics

DOCTORAL THESIS

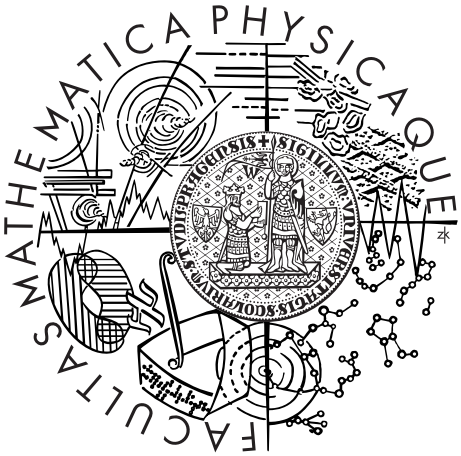

Frank Uhlig

Structure, dynamics and reactivity of the hydrated electron

Institue of Organic Chemistry and Biochemistry
Academy of Sciences of the Czech Republic

Supervisor of the doctoral thesis:	prof. Mgr. Pavel Jungwirth, DSc.
Study program:	Physics
Specialization:	Biophysics, Chemical and Macromolecular Physics

Prague 2014

I hereby declare that I carried out this doctoral thesis independently, and only with the cited sources, literature and other professional sources.

I understand that my work relates to the rights and obligations under the Act No. 121/2000 Coll., the Copyright Act, as amended, in particular the fact that the Charles University in Prague has the right to conclude a license agreement on the use of this work as a school work pursuant to Section 60 paragraph 1 of the Copyright Act.

In ..... date ..... Frank Uhlig

Název práce: Struktura, dynamkia a reaktivita hydratovaného elektronu.

Autor: Frank Uhlig

Katedra: Ústav organické chemie a biochemie, Akademie věd České republiky

Vedoucí disertační práce: prof Mgr. Pavel Jungwirth, DSc.

Abstrakt: Tato práce se zabývá zkoumáním hydratovaného elektronu, který je jedním z produktů ionizace vody a klíčovým meziproduktem radiační chemie ve vodném prostředí. Ačkoli se o existenci hydratovaného elektronu ví již více než 50 let, jeho struktura je těžko postižitelná a je předmětem diskuzí až do současnosti. V této práci jsme ukázali, že pomocí ab initio metod lze získat věrohodný popis hydratovaného elektronu, jeho rovnovážné struktury, jeho dynamiky po zachycení vodou a jeho reaktivity. Za tímto účelem byly zkoumány malé klastrové modely i rozsáhlé systémy modelující jak vnitřek, tak povrch kapaliny s rozpuštěným elektronem.

Klíčová slova: ionizace vody, vnitřek vody, rozhraní vody a páry, teorie funkcionálu hustoty, selfinterakční korekce

Title: Structure, dynamics and reactivity of the hydrated electron.

Author: Frank Uhlig

Department: Institute of Organic Chemistry and Biochemistry, Academy of Sciences of the Czech Republic

Advisor: prof Mgr. Pavel Jungwirth, DSc.

Abstract: In this work, one of the products of ionization of water, namely the hydrated electron, has been investigated. The hydrated electron is a key-intermediate in aqueous radiation chemistry. Although known to exist for over 50 years, its structure remained elusive and under discussion up to the present day. We show in this work, that we can obtain a faithful picture of the hydrated electron, its equilibrium structure, dynamics after attachment to water, and its reactivity, using ab initio methods. To this end, small cluster models and extended bulk and slab geometries of water including an excess electron have been investigated.

Keywords: water ionization, bulk water, air/water interface, density functional theory, self-interaction correction

Dedicated to my loving parents, Gerold and Sabine.

ᚾᛖᛞ ᚠᚢᚱᛁᛟᚢᛋ ᚾᛖᚾᛁᚨᛋ ᛏᚱᛁᚢᛗᛈᚺᚨᛚᛁᛋ ᛞᛖᚨᛏᚺ ᛞᚱᚨᚷᚨᚾ [1]

ᚲᚨᛏᚢᛚᛚᚢᛋ, in the poem ᚨᛞ ᚠᚨᚢᚾᚨᛗ

[1]Pity the warrior who slays all his foes.

Acknowledgements

First and foremost, I thank my advisor Pavel Jungwirth for four splendid years of scientific discussion, guidance, and fun. I thank all my collaborators and colleagues, the group of Pavel Jungwirth, in particular Ondřej Maršálek for his initial guidance on this project. I extend my gratitude to Martina Roeselová for translation of the abstract into Czech. My grateful thanks are also extended to Christopher Mundy, Shawn Kathmann, and Gregory Shenter for intense discussions and sharing their humongous resources.

I express my gratitude to my friends and family for constant support and their illustrious company. I am grateful to Miriam for being the terrific woman, that she is, and for occassionally reminding me that all work and no play would make me a dull boy.

Contents

Chapter 1

Introduction

Life on earth is inherently connected to the most ubiquitous solvent present, water. The body of a grown specimen of homo sapiens consists of about 60 % water (solutions). [1] The human cell's major constituents by mass are water (65 %), proteins (20 %), and lipids (12 %), while DNA only makes up roughly 0.1 %. [2] An illustrative example of DNA damage by ionizing radiation is the ɣ-irradiation of an aqueous solution of 0.5 g/l of DNA. Only about 0.5 % of the radiation is absorbed by the DNA and the rest by water. [3] Hence, in medical applications such as radiation therapy, where ionizing radiation is used to kill malignant cells, detailed understanding of the radiation-induced chemistry of water plays an important role. Below 1 MeV ɣ- and X-rays lead to ionization of water, whereas for higher energies pair-formation between electrons and positrons is observed. The photoionization of water reads in a simplified manner [4, 5]:

$$H_2O \longrightarrow H_2O^{\cdot+} + e^-_{pre} \tag{1.1}$$

$$H_2O^{\cdot+} + H_2O \longrightarrow {}^{\cdot}OH + H_3O^+ \tag{1.2}$$

$$e^-_{pre} \longrightarrow e^-_{aq} \tag{1.3}$$

After the initial electron detachment two components are formed, the "cationic hole" ($H_2O^{\cdot+}$) and a pre-solvated electron e^-_{pre}. The separation between the two species is proportional to the ionization energy as seen in decreasing geminate recombination rates with higher ionization energy. [6] The cationic hole reacts within few tens of femtoseconds to form ·OH radical and solvated proton. If it happens, geminate recombination will to 80 % happen with ·OH radicals and only to 20 % with hydrated protons. [7] The pre-solvated electron e^-_{pre} will at first be delocalized and encompassing several-nm-sized regions of water but will further on localize to form an equilibrated species, namely the hydrated electron e^-_{aq}. [8, 9] Both, ·OH and $e_{aq}{}^-$ were invoked in explanations of DNA damage. [10, 11] However, hydrated electrons cannot be considered to play a primary role in

direct DNA damage, because of their high reactivity towards diverse solutes and hence very short lifetimes. [3, 5] They will even react with water to form H· and OH^-, on a sub-millisecond time scale. [12] Nevertheless, reactions of hydrated electrons with solutes in water can lead to secondary products that can still be harmful.

Besides biological interest, radiolysis of water takes place in applications like nuclear waste remediation. [5] Reactions of the primary products, e.g., the hydrated electron lead to the formation of hydrogen gas which together with oxygen forms explosive gas mixtures that one seeks to avoid, especially in vicinity of nuclear waste. If not quenched, primary products of water radiolysis, in particular hydroxyl radicals, also lead to corrosion in water-cooled nuclear reactors due to the formation of H_2O_2.

Because of the high reactivity of hydrated electrons with a manifold of other solutes, it is important to attain a solid, in-depth understanding of structure and energetics of products of water radio- or photolysis.

In this work, our focus lies on only one of the products of water ionization, namely the hydrated electron. The first overall assumption is that we can treat the species generated by water ionization separately. This works well for high ionization energies when products of water ionization end up far away from each other compared to their individual extent. [6] If no geminate recombination is observed, both the hydrated electron and the cationic hole can be thought of as two more or less independent systems. This allows for focusing our attention on one problem at a time and hence treat the hydrated electron separately as an excess electron in water. Since its first detection over 50 years ago [13], renewed interest was shown in this elusive species, so also recently, as outlined below.

Elucidating the structure of the hydrated electron by experiment is only possible indirectly. One can estimate its overall extent by moment analysis of its optical absorption spectrum which gives a radius of gyration of about 2.4 Å. [14] Intimately connected with the structure is the binding energy of the hydrated electron which can be measured by photoelectron spectroscopy (PES). Up until recently measurements of vertical detachment energies (VDE) were only possible on cluster systems due to the requirement of ultra-high vacuum conditions to detect outgoing photoelectrons. Performing these experiments in a cluster-size dependent fashion can be used to extrapolate measured quantities to the water bulk. [14, 15] Observation of isomers with different binding energies and different extrapolations to infinite cluster size led to the suggestion that in bulk water also two different isomers might be observable - one high-binding isomer in the bulk interior with a VDE of about 3.3 eV and one low-binding isomer at the water surface with a VDE of about 1.6 eV. [16] In the experiment, water clusters are

generated by expansion into vacuum, leading to cooling of the water clusters and thus solidification, so that the investigated clusters are not representative of liquid bulk water. This was recognized in different experimental [17, 18] as well as theoretical studies [19, 20, 21]. Low-binding isomers disappear from the measured spectra by changing the conditions of the vacuum expansion, e.g., use of different carrier gases and pressures. [18] In the same spirit, only high-binding isomers survive upon annealing of the anionic water clusters up to their evaporation-ensemble temperatures after cluster generation. [17] This suggests that low-binding isomers actually exist only due to kinetic trapping in cold water clusters. The formation of metastable structures at low temperatures was observed in theoretical studies of electron attachment to cold water clusters. [19, 20] It was also found that electron attachment depends strongly on the thermal history of the water cluster. [21] Furthermore, at ambient conditions only little correlation is found between the location of an excess electron in medium-sized water clusters and its vertical detachment energies. [22, 23, 24] Rather a correlation between size and VDE is observed, i.e., the larger the hydrated electron the less it is bound and vice versa.

The advent of the liquid microjet technique allowed for actual measurement of VDEs in highly volatile liquids as water, meaning both systems of extended size and at temperatures above the freezing temperature of water. [25] Different groups measured the bulk vertical detachment energy of the hydrated electron to be within 3.3 to 3.6 eV. [26, 27, 28, 29] One of these groups also suggested that there would be a stable low-binding isomer at the water surface, corresponding to before-mentioned extrapolations, at 1.6 eV. [28] This excess electron would have to be delocalized over the water surface according to the correlation between size and VDE. In contrast to that there are surface-sensitive second-harmonic generation spectroscopy measurements, where the hydrated electron was found to be below the dividing surface of water. [30] Neither have the measurements in ref. [28] ever been reproduced nor has anyone else up to now found a second, low-binding isomer in liquid water. In particular, most recent investigations on photoemission near a liquid water surface found no evidence of a low-binding surface-isomer of the hydrated electron. [31]

Sometimes termed the most simple quantum solute in water [28, 32], theoretical description of the hydrated electron has relied to a large degree on the use of so-called one-electron pseudopotential (OEPP) methods. [33] All-electron studies of an excess electron in water have been performed with ab initio methods mainly for small cluster systems [34] and for medium-sized anionic water clusters in the range of a few tens of water molecules. [24, 35] Studies of extended systems with ab initio methods have been performed, but were prone to artifacts due to very limited unit cell sizes. [36, 37] The OEPP methods map the

many-electron problem onto a mixed quantum-classical description, where only the excess electron is treated quantum mechanically. The interaction with the surrounding solute is described by a pre-parametrized pseudopotential and interactions of solute with solute by an effective pair-potential. [1] Quite a few of these pseudopotential parameterizations exist [33], one of which recently initiated a debate about the general structure of the hydrated electron. [38] Since the discovery of the hydrated electron, people were more or less convinced that the electron would localize to a cavity surrounded by water molecules with one OH bond each polarized towards the center of this elusive cavity. [33, 39, 40] Many independent pseudopotential parameterizations show this general picture but differ in details, such as the coordination number of the hydrated electron. [33] The number of water molecules in the first solvent shell is either four or six in these models. [33] A recent pseudopotential on the other hand claimed that the electron would not localize at all in a cavity. [38] Instead, a region of enhanced water density would form over which the excess electron would be spread. Responses to that article showed how sensitive these results are with respect to the parametrization and how, with a little tweaking of the pseudopotential, a cavity-forming hydrated electron would be recovered instead of the delocalized species. [41, 42, 43] Nevertheless, the delocalized model of a hydrated electron is capable of reproducing a number of experimental observables correctly. Whereas vertical detachment energies and optical absorption spectra at ambient conditions are well reproduced with different models [44], the temperature dependence of the optical absorption spectrum and the resonance Raman spectrum are best reproduced with the OEPP yielding the delocalized model of a hydrated electron. [45]

Without relying on artificial splits between the excess electron and electrons constituting the water molecules, in this thesis we explore the structure, dynamics, and reactivity of the hydrated electron with ab initio methods. This shall help us to perform our investigations in an as unbiased way as possible. The work deals, among other things, with the controversial issues outlined above. Thus, we investigate first the structure of the bulk-hydrated electron, and second, how the latter differs from an electron solvated at the water/vapor interface. Small cluster models serve benchmarking purposes as well as model systems for the reactivity of the hydrated electron with different quenchers, such as hydronium cation and nitrous oxide. After having established an ab initio view on the hydrated electron in thermal equilibrium we can then go one step further and investigate the dynamics following water ionization. Again, we restrict ourselves to an excess electron in water, but this time following its time evolution after vertical

[1] To some degree this explains the misconception of the "most simple" quantum solute in water.

attachment to neat water.

Chapter 2

Methodology

In this chapter we explain in detail methods used in this work. It is not intended to give a full review of all computational methods, but rather highlight some of their important aspects and introduce employed approximations. References to detailed reviews and books are provided. The main results of the thesis were produced with ab initio molecular dynamics simulations of bulk and slab systems; minimum energy structures, and reaction paths were established in small cluster systems. This chapter is organized as follows, sec. 2.1 gives an introduction to classical molecular dynamics (CMD), followed by a short introduction to how energies and forces are obtained in the framework of density functional theory (DFT), sec. 2.2. The next sections deal with minimum energy structures and minimum energy paths (sec. 2.3) followed by a brief introduction to time-dependent density functional theory (TDDFT) (sec. 2.4). In sec. 2.5 various solvation models are described. Section 2.6 provides details of the analyzes used to investigate the systems of interest, focusing on particular schemes that are either considered non-standard or very special to the problem at hand, i.e., the hydrated electron. The last subsection (sec. 2.7) gives the specific details of the calculations.

2.1 Classical Molecular Dynamics

All systems in nature are driven by forces stemming from the interactions among their constituents and possibly external potentials. Directly following the resulting time evolution of a system in form of molecular dynamics simulations can be used for sampling of structures belonging to an ensemble in thermodynamic equilibrium or to follow processes like chemical reactions in time. Good resources for a detailed account are refs. 46, 47.

Ignoring relativistic effects and concerning ourselves with the level of detail of electrons and protons, the time evolution of a system is given by the time-

dependent Schrödinger equation (TDSE):

$$i\frac{\partial}{\partial t}\Phi\left(\{\mathbf{r}_i\},\{\mathbf{R}_I\}\right) = \mathcal{H}\Phi\left(\{\mathbf{r}_i\},\{\mathbf{R}_I\}\right). \tag{2.1}$$

Atomic units are used here and in the following. [1] Here, Φ is the wavefunction of our system and $\mathcal{H}$ the Hamiltonian consisting of the bare Coulomb potential for electrons and nuclei and their kinetic energy terms. $\{\mathbf{r}_i\}$ and $\{\mathbf{R}_I\}$ are the collection of electronic and nuclear coordinates, respectively. [2] The electronic coordinates and corresponding indices are given as lowercase letters and the ones for nuclear coordinates and corresponding indices as uppercase letters throughout this work. The total Hamiltonian $\mathcal{H}$ is given as follows

$$\begin{aligned}\mathcal{H}\left(\{\mathbf{r}_i\},\{\mathbf{R}_I\}\right) &= \underbrace{\sum_I \frac{1}{2M_I}\nabla_I^2}_{\mathcal{T}_\mathrm{N}} \underbrace{-\sum_i \frac{1}{2}\nabla_i^2}_{\mathcal{T}_\mathrm{e}} + \underbrace{\sum_i\sum_{j\neq i}\frac{1}{|\mathbf{r}_i-\mathbf{r}_j|}}_{\mathcal{V}_\mathrm{ee}} \\ &- \underbrace{\sum_i\sum_I \frac{Z_I}{|\mathbf{R}_I-\mathbf{r}_i|}}_{\mathcal{V}_\mathrm{eN}} + \underbrace{\sum_I\sum_{J\neq I}\frac{Z_I Z_J}{|\mathbf{R}_i-\mathbf{R}_J|}}_{\mathcal{V}_\mathrm{NN}}.\end{aligned} \tag{2.2}$$

Operators $\mathcal{T}$ represent kinetic energy terms labeled with indices corresponding to electronic (e) or nuclear (N) degrees of freedom and $\mathcal{V}$ represent operators for Coulomb interaction between particles. Z_I is the nuclear charge of atom I. Solving the TDSE represents a complex problem that is tractable analytically only for few model systems and numerically for low-dimensional systems. To tackle this problem for non-trivial systems a set of approximations has to be introduced. Instead of simultaneously solving the full TDSE for nuclei and electrons, one first assumes that one can split the problem into a nuclear and an electronic part and solve the electronic, time-independent Schrödinger equation (TISE) for a fixed nuclear configuration ("clamped nuclei"). The electronic part of the TISE with the Hamiltonian $\mathcal{H}_e = \mathcal{T}_{ee} + \mathcal{V}_{ee} + \mathcal{V}_{eN}$ is:

$$\mathcal{H}_\mathrm{e}\left(\{\mathbf{r}_i\};\{\mathbf{R}_I\}\right)\Psi_k\left(\{\mathbf{r}_i\};\{\mathbf{R}_I\}\right) = E_k\left(\{\mathbf{R}_I\}\right)\Psi_k\left(\{\mathbf{r}_i\};\{\mathbf{R}_I\}\right). \tag{2.3}$$

E_k are the eigenvalues corresponding to Ψ_k. The semicolon indicates a parametric dependence, i.e., although the electronic problem depends on the specific nuclear configuration it is solved for, there is no explicit dependence on them. Knowing the solutions to this equation we can write the full quantum-mechanical wavefunction as expansion in the electronic wavefunctions Ψ_l, where the nuclear

[1] In atomic units the electron mass m_e, elementary charge e, reduced Planck's constant $\hbar$ and Coulomb's constant $1/4\pi\varepsilon_0$ are set to unity.

[2] Vectors are given in bold face.

wavefunctions χ_l can be understood as expansion coefficients:

$$\Phi\left(\{\mathbf{r}_i\},\{\mathbf{R}_I\}\right) = \sum_{l=0}^{\infty} \Psi_l\left(\{\mathbf{r}_i\};\{\mathbf{R}_I\}\right)\chi_l\left(\{\mathbf{R}_I\};t\right). \tag{2.4}$$

Inserting eq. 2.4 into eq. 2.1, multiplying from left with Ψ_k^* and integrating over all electronic coordinates gives:

$$\left[-\sum \frac{1}{2M_I}\nabla_I^2 + E_k\left(\{\mathbf{R}_I\}\right)\right]\chi_k + \sum_l C_{kl}\chi_l = i\frac{\partial}{\partial t}\chi_k. \tag{2.5}$$

These are a set of coupled differential equations with E_k the eigenvalues of Ψ_k in eq. 2.3. The non-adiabatic coupling operator C_{kl} is:

$$C_{kl} = \int \Psi_k^* \left[-\sum \frac{1}{2M_I}\nabla_I^2\right]\Psi_l d^3r + \frac{1}{M_I}\sum_I \left\{\int \Psi_k^*\left[-i\nabla_I\right]\Psi_l d^3r\right\}\left[-i\hbar\nabla_I\right]. \tag{2.6}$$

Up to this point no approximations have been introduced. The time-evolution of the system is governed by the Hamiltonian with an exact wavefunction. This is still too difficult to solve numerically. To make molecular dynamics feasible we have to analyze the terms in C_{kl}. These non-adiabatic coupling elements comprise two contributions. First, the coupling between different electronic states (off-diagonal terms C_{kl}) and second, the coupling between the electronic and nuclear degrees of freedom (diagonal terms C_{kk}). Neglecting the first term will lead to dynamics in only one electronic state without any electronic transitions. This is thus called the "adiabatic" approximation and works well for molecular dynamics in the ground state when it is well separated from higher lying electronic states, e.g., as in insulators like water. The second term can be neglected in most cases and will lead to errors smaller than 0.5% except for very unfavorable situations. [48] The latter is the famous "Born-Oppenheimer" approximation. [49] Together with the adiabatic approximation it allows us to approximate our wavefunction Φ (eq. 2.4) as a single product of one electronic and one nuclear wavefunction:

$$\Phi\left(\{\mathbf{r}_i\},\{\mathbf{R}_I\};t\right) \approx \Psi_k\left(\{\mathbf{r}_i\};\{\mathbf{R}_I\}\right)\chi_k\left(\{\mathbf{R}_I\};t\right). \tag{2.7}$$

Up to this point we are still dealing with nuclear and electronic wavefunctions. The next step, which leads to classical dynamics, is the simplification of the nuclear part of the problem. A rigorous derivation is beyond the scope of this short introduction. For a good review see [47, 50]. For not-explicitly time-dependent Hamiltonians the quantum-mechanical expectation values of position $\mathbf{R}$ and mo-

mentum $\mathbf{P}$, $\langle\mathbf{R}\rangle$ and $\langle\mathbf{P}\rangle$, are given by Ehrenfest's theorem [51] as

$$i\frac{d}{dt}\langle\mathbf{R}_I\rangle = \langle[\mathcal{H},\mathbf{R}_I]\rangle = i\frac{\langle\mathbf{P}_I\rangle}{M_I} \tag{2.8}$$

$$i\frac{d}{dt}\langle\mathbf{P}_I\rangle = \langle[\mathcal{H},\mathbf{P}_I]\rangle = -i\langle\nabla_I E_k(\{\mathbf{R}_I\})\rangle \tag{2.9}$$

where $[,]$ denotes the commutator. Combining these two equations leads to Newtonian equations of motion for the expectation value of the nuclear wavefunction:

$$M_I\frac{d^2\langle\mathbf{R}_I\rangle}{dt^2} = -\langle\nabla_I E_k(\{\mathbf{R}_I\})\rangle\,. \tag{2.10}$$

Substituting for the nuclear wavefunction a product of Dirac's δ-functions centered at the coordinates of the nuclei leads to the "classical-nuclei" approximation. This is often a good approximation for systems at ambient conditions. The error of this approximation is related to the extent of the nuclear wavefunction and is small for tight wavefunctions. This simplification leads to our working equations for the molecular dynamics:

$$M_I\frac{d^2}{dt^2}\mathbf{R}_I(t) = -\nabla_I E_k(\{\mathbf{R}_I(t)\})\,. \tag{2.11}$$

These equations lead to dynamics referred to as "ab initio", "first-principles", or also "Born-Oppenheimer" molecular dynamics (AIMD, FPMD, or BOMD). Various methods are in principle available to solve the right-hand side of eq. 2.11. Throughout this work we work with variational methods, density functional theory in particular, which calculate the forces exerted on the nuclei by solving a variational problem for the ground state wavefunction Ψ_0 and thus eq. 2.11 changes to:

$$M_I\frac{d^2}{dt^2}\mathbf{R}_I(t) = -\nabla_I\min_{\Psi_0}\{\langle\Psi_0|\mathcal{H}_e|\Psi_0\rangle\} \tag{2.12}$$

or in terms of the electron density $n(\mathbf{r})$ in DFT:

$$M_I\frac{d^2}{dt^2}\mathbf{R}_I(t) = -\nabla_I\min_{n_0}\{E_0[n]\}\,. \tag{2.13}$$

Here, $E_0[n]$ represents the energy functional of the electron density n as detailed in section 2.2.

Forces in eq. 2.12 can be calculated by differentiation of the expectation value of the electronic Hamiltonian:

$$\nabla_I\langle\Psi_0|\mathcal{H}_e|\Psi_0\rangle = \langle\nabla_I\Psi_0|\mathcal{H}_e|\Psi_0\rangle + \langle\Psi_0|\mathcal{H}_e|\nabla\Psi_0\rangle + \langle\Psi_0|\nabla\mathcal{H}_e|\Psi_0\rangle\,. \tag{2.14}$$

For stationary-state wavefunctions of $\mathcal{H}_e$ the first two contributions vanish and

only the last term remains. This is true provided a complete basis set is used (the Hellmann-Feynman theorem). [52, 53] In practice the exact ground state cannot be obtained and the wavefunction has to be represented in a finite basis set. Thus, actual force calculations are often more involved than only evaluating the gradient of the Hamiltonian. Additional terms arise for basis functions with an explicit origin (like atom-centered Gaussian functions), but not for originless basis functions (like plane waves). In computational implementations of variational methods errors are introduced due to incomplete self-consistency, but can be made arbitrarily small with high convergence (at increased computational effort). The exact magnitude of this error is unknown, but ways to estimate it exist (see ref. 47 and references therein).

The equations of motion 2.11 have to be solved numerically by discretizing time and step-by-step integration (propagation). Various algorithms exist for that purpose and in this work the velocity-Verlet propagator (VVP) was used throughout. [54] The most important properties that such an algorithm must fulfill are time-reversibility of the continuous equations of motion and good overall energy conservation. Direct propagation of the equations of motion leads to sampling of the microcanonical ensemble (NVE). To account for thermal and pressure coupling additional algorithms are needed influencing the equations motions in a way to reproduce other statistical ensembles like the canonical ensembles (NVT and NpT). [46]

Ab inito molecular dynamics simulations depend only on a few parameters, as the name suggests. Nevertheless, these parameters can be determining for accuracy and efficiency of the calculations. In particular, the convergence criterion of the wavefunction optimization needs to be sufficiently tight to guarantee converged forces and simultaneously not to be so demanding that the calculations become inefficient. Neither should the conserved energy show significant drift, compared to the fluctuations in the potential energy. Even if the wavefunction of the previous MD step is used as initial guess for the current MD step, large drifts in the conserved energy can be observed with tight wavefunction convergence. [55] A method for obtaining good intial guesses for the initial wavefunction that also improves overall energy conservation is the always stable predictor corrector (ASPC) algorithm, developed originally in the context of polarizable force field simulations. [56] Together with the APSC algorithm a convergence criterion of 10^{-6} a.u. on the forces of each orbital represents a good compromise in accuracy and efficiency of AIMD simulations. Furthermore, algorithms that avoid diagonalization of the wavefunction at each step in the self-consistent field cycle can be used to improve overall performance (e.g., the so-called “orbital-transformation” (OT) method [57]).

2.2 How to get proper forces

Many different methods exist to approximately solve the electronic, time-independent Schrödinger equation 2.3. In Hartree-Fock (HF) theory, which is the basis of many other methods, the electronic problem is solved for an electronic wavefunction given by a single Slater determinant. This leads to proper treatment of Pauli repulsion between the electrons. Unless additional (most often perturbative) corrections [1] are introduced, Hartree-Fock calculations lack any electronic correlation. The treatment of correlation effects for wavefunction-based methods is generally very demanding in terms of computer time and has unfavorable scaling with system size. Beyond tens of heavy atoms this very quickly becomes unfeasible and it is intractable for extended systems like bulk water. Hence, the major workhorse for ab initio molecular dynamics nowadays is density functional theory, which allows for accurate calculations in a reasonable time frame and includes electronic correlation effects. For a good review of DFT see ref. 58 or with respect to AIMD refs. 47, 59. DFT is based on two theorems by Hohenberg and Kohn. [60] In brief, the first theorem shows that a direct mapping between the ground state electronic density n_0 and the external potential v_{ext} (the nuclei) exists. The external potential v_{ext} (and thus the Hamiltonian of the system) is a unique functional of the electronic density. Therefore, the total energy of a system can be written as functional of the electron density $E[n]$. The second theorem states that a variational ansatz with respect to the electron density holds. The first theorem leads to an expression of the total, electronic energy $E[n]$ of the system as a functional of the electronic density $n(\mathbf{r})$:

$$E[n] = F[n] + \int n(\mathbf{r})\, v_{\text{ext}}(\mathbf{r})\, d^3r. \tag{2.15}$$

The exact form of the functional $F[n]$ is not known and has to be approximated for actual calculations. It includes the electronic kinetic energy $E_{\text{T}}[n]$ and the interaction between the electrons. The latter is often split into two contributions, the classical electron-electron repulsion E_{H} and the quantum-mechanical exchange and correlation effects E_{XC}. The last term in eq. 2.15 describes the interaction of the electronic density with any kind of external potentials, including the coulombic potential of the nuclei. The energy can be minimized variationally with respect to the density to give the ground state energy E_0:

$$E_0[n] = \min_n \left\{ F[n] + \int n(\mathbf{r})\, v_{\text{ext}}(\mathbf{r}) d^3r \right\}. \tag{2.16}$$

[1] Reference calculations in this work were carried out with second-order Møller-Plesset perturbation theory.

The minimization is subject to the constraint that the electronic density must stem from an antisymmetric wavefunction and integrate to the number of electrons (n-representability). Alone, the two Hohenberg-Kohn theorems do not allow for an accurate computational implementation. The main problem is that the kinetic-energy E_T is not known as a functional of the electron density. To remedy this problem, Kohn and Sham introduced a non-interacting reference system in form of a single Slater determinant $\Psi\left(\{\mathbf{r}_i\}\right)$, constructed from one-particle wavefunctions ψ_i, that reproduces the electron density of the fully interacting system. [61] The electronic density is then given as:

$$n\left(\mathbf{r}\right) = \sum_{i=1}^{n} f_i \left|\psi_i\left(\mathbf{r}\right)\right|^2 , \tag{2.17}$$

where f_i are the occupation numbers of the one-particle orbitals. The kinetic energy E_T^s of the reference system can be calculated as:

$$E_\mathrm{T}^\mathrm{s} = \sum_{i=i}^{n} \left\langle \psi_i\left(\mathbf{r}\right)\right| - \frac{1}{2}\nabla^2 \left|\psi_i\left(\mathbf{r}\right)\right\rangle . \tag{2.18}$$

This is not the full, electronic kinetic energy as it is only that for the non-interacting reference system. It is a good approximation, though. The residual term $E_\mathrm{T}\left[n\right] - E_\mathrm{T}^\mathrm{s}\left[n\right]$ is approximatively included in the so-called exchange-correlation (XC) functional. For interacting, many-electron systems the exact form of the XC functional is not known either. Many approximate forms exist based on different ideas, vide infra. Introduction of the single-particle orbitals ψ_i leads to a set of effective, coupled single-particle equations:

$$\left[\frac{1}{2}\nabla^2 + v^\mathrm{s}\left(\mathbf{r}\right)\right]\psi_i\left(\mathbf{r}\right) = \epsilon_i\psi_i\left(\mathbf{r}\right) \tag{2.19}$$

which have to be solved iteratively. ϵ_i are eigenvalues to the single-particle solutions and v^s is the Kohn-Sham (KS) potential. The KS-potential is constructed from the external potential, the classical electron-electron repulsion, and the exchange correlation potential. Equations 2.19 are then solved iteratively in form of a self-consistent field cycle until convergence is reached.

In the specific CP2K implementation of density functional theory a dual-representation of the electron density is used. [62] Both, an atom-centered basis set of Gaussian-type orbitals (GTO) and a plane-wave (PW) basis set are used to expand the electron density. This way, the most effective procedures connected to either basis-set representation can be used. Multi-center overlap integrals can be calculated efficiently using recurrence relations in the GTO basis set, whereas in

the plane-wave basis set (periodic) electrostatics are calculated using Fast Fourier Transforms (FFT). FFTs are very efficient and linear scaling of computational effort with respect to the system size is possible. The electronic density is given in the GTO basis set as:

$$n(\mathbf{r}) = \sum_{\mu\nu} P_{\mu\nu} \psi_\mu^*(\mathbf{r}) \psi_\nu(\mathbf{r}). \tag{2.20}$$

$P_{\mu\nu}$ are density matrix elements and each orbital ψ_μ is expanded into primitive Gaussian functions g_i with pre-determined coefficients $d_{i\mu}$ as $\psi_\mu(\mathbf{r}) = \sum_i d_{i\mu} g_i(\mathbf{r})$. The expansion coefficients $\bar{n}(\mathbf{G})$ for the density in the plane-wave basis set $\bar{n}(\mathbf{r})$ are chosen to reproduce the density in the GTO basis set $n(\mathbf{r})$ as:

$$\bar{n}(\mathbf{r}) = \frac{1}{\Omega} \sum_{\mathbf{G}} \bar{n}(\mathbf{G}) \exp(i\mathbf{G} \cdot \mathbf{r}). \tag{2.21}$$

Ω is the volume of the unit cell and $\mathbf{G}$ are the reciprocal lattice vectors. The use of the plane-wave basis set has the aforementioned advantage that the classical electrostatic energy can be evaluated efficiently using fast Fourier transforms. The Hartree potential for the electronic density in reciprocal space is $v_{\mathrm{H}}(\mathbf{G}) = 4\pi\bar{n}(\mathbf{G})/\mathbf{G}^2$ and the electrostatic energy of the electron density is then just $\frac{\Omega}{2}\sum_{\mathbf{G}} \bar{n}(\mathbf{G}) v_{\mathrm{H}}(\mathbf{G})$. The use of the plane-wave basis set has the drawback that for all-electron calculations plane waves with high kinetic energy (small grid-spacing in real space) would be needed. For practical calculations the atomic cores are thus substituted by pseudopotentials (PPs). In CP2K, relativistic, norm-conserving pseudopotentials of the Goedecker-Teter-Hutter type are used. [63] This introduces additional terms to the electrostatic energy of the form $P_{\mu\nu} \langle \psi_\mu(\mathbf{r}) | V_{\mathrm{PP}}(r) | \psi_\nu(\mathbf{r}) \rangle$. The pseudopotentials V_{PP} are split into a local and a non-local part. The former consists of a short- and a long-ranged contribution. Additionally, the nuclei are represented by Gaussian functions where parameters for their width and pseudopotential parameters are chosen such that the long-ranged part of the local pseudopotential cancels the respective core charge distribution. This specific choice of parameters makes a range separation possible, such that total electrostatics can be evaluated using the Ewald summation technique, i.e., the short-ranged part is evaluated directly in real space and the long-ranged part in reciprocal space using FFTs as mentioned above (see also sec. 2.5.2).

Despite its overwhelming success, density functional theory has several drawbacks. The exact form of the exchange-correlation functional E_{XC} is not known. Commonly used approximations are the local density approximation (LDA) and the generalized gradient approximation (GGA). The exchange-correlation energy

in the local density approximation depends only on the density at a given point in space **r**:

$$E_{\mathrm{XC}}^{\mathrm{LDA}} = \int d^3 r \varepsilon_{\mathrm{XC}}\left(n\right) n\left(\mathbf{r}\right) \tag{2.22}$$

and for the GGA-type functionals E_{XC} additionally depends on the gradient of the electron density at **r**:

$$E_{\mathrm{XC}}^{\mathrm{GGA}} = \int d^3 r \varepsilon_{\mathrm{XC}}\left(n, \nabla n\right) n\left(\mathbf{r}\right). \tag{2.23}$$

In both eq. 2.22 and 2.23 $\varepsilon_{\mathrm{XC}}$ denotes the energy density per particle. The XC energy definitions are given excluding spin-dependent terms which can be included and one obtains the local spin density (LSD) formalism.

On a general level, two classes of errors can be identified in KS-DFT calculations. As pointed out above, in practical DFT calculations the functional $F[n]$ has to be approximated, say by $\tilde{F}[n]$. Hence the minimizing density in eq. 2.16 is also approximate, denoted as $\tilde{n}(\mathbf{r})$. The resulting error of the DFT calculation can then be given as [64]:

$$\Delta E = \tilde{E} - E = \Delta E_F + \Delta E_D. \tag{2.24}$$

ΔE_F is the error introduced by approximating the exact density functional, i.e., the "functional error" $\tilde{F}[n] - F[n]$ and ΔE_D is the "density-driven" error due to the error in the electron density $n\left(\mathbf{r}\right)$ and is defined by eq. 2.24. In common GGA KS-DFT calculations, the dominating error is usually ΔE_F. [64] LDA and GGA density functionals do not exhibit the correct long-range decay of the XC potential. They decay faster, often in an exponential manner whereas the true potential should decay as $1/r$. [58, 65] Due to the self-interaction error (SIE) the density-driven error can become the prominent problem for open-shell species. The SIE is a remnant of the approximate exchange-correlation functionals used in practice for which electrostatic and exchange-correlation energy do not cancel out for a single electron, as they should in the exact density functional. Various schemes have been introduced to counter this problem, i.e., the so-called self-interaction corrections (SICs). [66, 67, 68] The SIE is in particular prominent for open-shell species, e.g., doublet radicals like the hydrated electron. For AIMD simulations presented in this work a semi-empirical SIC scheme was employed that only acts on the density of the unpaired electron. [68] This is achieved by adding two terms to the original energy functional $E[n]$ that themselves depend on the spin density m:

$$E^{\mathrm{corr}}[n] = E[n] - aE_{\mathrm{H}}[m] - bE_{\mathrm{XC}}[m, 0], \tag{2.25}$$

resulting in a corrected energy functional E^{corr}, which can be tuned by adjusting the two parameters a and b. [1] Corresponding parameter combinations used in this work are given as, e.g., SIC($a = 0.3$, $b = 0.2$). Correcting the spurious self-interaction associated with singly occupied molecular orbital is the most important for systems which are well described without the unpaired electron. [69, 70] The parametrization can be done with respect to correlated ab initio methods as in the original publication [68] and is system-dependent. Although this might be viewed as not being "ab initio", it has the advantage that one can adjust to different situations where other schemes fail or are too costly. This methodology is only slightly more costly compared to an uncorrected calculation with the same density functional.

The SIE can also be reduced by employing hybrid functionals which include, at least partially, exact Hartree-Fock exchange. Going one step further, one can include exact exchange only beyond a specific range as is done in so-called long-range corrected (LRC) hybrid DFs (for a good review see ref. 71). The range-separation of the Coulomb operator takes following form:

$$\frac{1}{r} = \underbrace{\frac{\operatorname{erfc}(\mu r)}{r}}_{\text{short-range}} + \underbrace{\frac{\operatorname{erf}(\mu r)}{r}}_{\text{long-range}}, \tag{2.26}$$

using the error function (erf) and its complimentary function (erfc). The range-separation parameter μ determines the reach of the regular DF description as in eq. 2.22 or 2.23 (short-range part) and from where exact exchange is included (long-range part, e.g., Hartree-Fock exchange). This cures the incorrect decay of the XC potential and reduces the self-interaction error, but at significantly elevated computational cost. The range-separation parameter μ needs to be chosen properly. This can be done by benchmarking against high-level ab initio calculations [72] or by enforcing the IP-theorem from exact density functional theory for the approximate density functionals [71]. The IP-theorem states that for the exact DF the negative of the eigenvalue of the highest occupied molecular orbital ϵ_{HOMO} coincides with the vertical ionization energy E_{IP} [73, 74]:

$$-\epsilon_{\text{HOMO}} = E_{\text{IP}}. \tag{2.27}$$

[1] The SIC is to be used within the restricted open-shell formalism of KS-DFT for doublet radicals only. Artifacts are to be expected for fully spin-polarized wavefunction, where the spin density does not necessarily coincide with the density of the singly occupied molecular orbital.

2.3 Minimum energy structures and paths

Forces calculated according to secs 2.1 and 2.2 can also be used to obtain optimized minimum energy structures. Although relevance of minimum energy structures diminishes with increasing system size as a plethora of local minima close in energy exists and a single optimized structure looses its value, small model systems can be very useful for conceptual understanding and also for benchmarking purposes.

Various algorithms for optimizing a system's energy with respect to its molecular geometry ("geometry optimization") exist. Many of them stem from mathematical function optimizations based on local line-search algorithms [1], like conjugate gradients (CG) or the Broyden-Fletcher-Goldfarb-Shanno (BFGS) algorithm. More detailed information can be found, e.g., in ref. [75]. From these methods only the BFGS algorithm was used in this work, because of its ability to find the deepest local minimum within the vicinity of the starting configuration. It belongs to the class of optimizers based on Newton's method, i.e., approximating the function locally by a quadratic expansion around the current functional value in the optimization procedure. Due to the high cost of calculating the full Hessian matrix it is approximated and approximatively updated in each step of a BFGS optimization.

Other algorithms, specifically designed for the search of minimum energy structures have been designed in analogy to molecular dynamics algorithms. Two examples are the projected velocity Verlet (PVV) algorithm [76] and the fast inertial relaxation engine (FIRE) [77]. The former method propagates the system according to the well-known velocity-Verlet molecular dynamics algorithm, but only includes components of the velocity parallel to the actual force. This projection is done at every time step during the optimization. The velocity is zeroed if force and velocity point in opposite directions, thus avoiding up-hill movements in the respective direction. The latter, FIRE algorithm, also takes dynamical steps according to an MD propagator, but with a variable time step. The velocity and time step are modified according to the projection of force on velocity. The velocity in direction of the projection and the time step are increased if the projection is larger than zero and the velocity is set to zero and the time step decreased if the projection is smaller than or equal to zero. Thus, the optimization avoids up-hill movements similarly to the PVV and, furthermore, speeds up into the direction of decreasing energy. It is driven by the overall inertia of the system and thus capable of handling shallow energy landscapes efficiently.

[1] Global optimization methods based on "trust-regions" or heuristic algorithms like "simulated annealing" or "genetic algorithms" are less common.

The optimization of reaction paths is more involved as the goal is to obtain a full minimum energy path along an, in principle arbitrary, reaction coordinate. The reaction coordinate can be for example the complete nuclear configuration or just the distance between two atoms. Often used is the drag method, which successively increases the reaction coordinate from reactant to product state and at each step optimizes the structure around the constrained reaction coordinate. This can become arbitrarily complex and cumbersome for systems where a reaction coordinate is non-obvious and in principle simultaneous scans along all nuclear degrees of freedom have to be done. Also, the use of pre-defined reaction coordinates biases the optimization of the minimum energy paths without guaranteeing to find a (relevant) transition state. Methods working in the complete configurational space without the need to assign pre-defined reaction coordinates have been developed to circumvent this problem.

Reaction paths throughout this work were calculated with nudged elastic band (NEB) methods. [78, 79] These methods employ a band of images, connected by harmonic springs, that leads from reactants to products of a transformation, not necessarily a chemical reaction. To extract meaningful barriers and relative energetics both reactants and products have to be minimum energy structures. In principle only the initial and final structures need to be known initially. They are then connected by a band of intermediate images which can, e.g., be generated by linear interpolation between initial and final state. The band is optimized with forces from both the potential energy surface of the system as well as forces due to the harmonic springs between neighboring images. The term "nudged" derives from the fact that the force on an image is divided into components perpendicular and parallel to the band. This removes problems with "corner-cutting" in the original implementation of an elastic band. [80] The perpendicular component in the NEB is due to the underlying potential energy surface and the parallel component is due to the harmonic springs. Different ways of estimating the tangent to the band at an image exist. In this work only the so-called "improved tangents" version of the NEB (i.e., IT-NEB) was used. [78] The tangents $\boldsymbol{\tau}$ are calculated as the difference in configuration $\mathbf{R}_i$ [1] between the image and the neighboring image with higher energy $\mathbf{R}_{\mathrm{hi}}$ and normalized to give $\hat{\boldsymbol{\tau}}$:

$$\hat{\boldsymbol{\tau}} = \pm \frac{\mathbf{R}_{\mathrm{hi}} - \mathbf{R}_i}{|\mathbf{R}_{\mathrm{hi}} - \mathbf{R}_i|}. \tag{2.28}$$

The sign depends on whether the previous image to i (minus) or the next image to i (plus) has a higher energy than i. If both neighboring images have a higher

[1] In contrast to before $\mathbf{R}_i$ comprises all nuclear coordinates in one vector and not just the coordinates of one atom.

or lower energy than i, a weighted average of the vectors to the adjacent images is taken. The weights are the relative energy differences between the images. The force acting parallel to the path is calculated as:

$$\mathbf{F}_{i,\text{para}} = k\left(|\mathbf{R}_{i+1} - \mathbf{R}_i| - |\mathbf{R}_i - \mathbf{R}_{i-1}|\right)\hat{\boldsymbol{\tau}}_i. \tag{2.29}$$

The force acting perpendicular to the band $\mathbf{F}_{i,\text{perp}}$ is calculated from the potential energy surface $E(\mathbf{R}_i)$ as:

$$\mathbf{F}_{i,\text{perp}} = \nabla E(\mathbf{R}_i) - \nabla E(\mathbf{R}_i)\,\hat{\boldsymbol{\tau}}_i. \tag{2.30}$$

The band is then optimized with respect to the sum of perpendicular and parallel forces. The construction of the forces ensures equal spacing between the images and that the band converges to the minimum energy path. Estimation of the transition state can be done by interpolation between the optimized energies of the band in the transition state region or by using a climbing image within the band (i.e., CI-NEB). [79] The climbing image is identified as the image in the band with the highest energy and the force on this image is:

$$\mathbf{F}_{i,\text{CI}} = -\nabla E(\mathbf{R}_{i,\text{CI}}) + 2\nabla E(\mathbf{R}_{i,\text{CI}})\,\hat{\boldsymbol{\tau}}_{i,\text{CI}}\hat{\boldsymbol{\tau}}_{i,\text{CI}}. \tag{2.31}$$

The energy of the climbing image thus increases during the optimization. This ensures that after optimization of the band the climbing image is a transition state.

2.4 Time-dependent density functional theory

Time-dependent density functional theory [1] is by far too complex to allow for a comprehensive overview in this section. For good reviews see, e.g., refs. [82, 83] and references therein. Similarly to ground state DFT, TDDFT rests on the proof that the external potential is a functional of the exact density. It can be shown that this also holds for explicitly time-dependent densities and potentials. [84] With this knowledge one can write single-particle equations for the time-evolution of the Kohn-Sham single-particle orbitals analogously to eqs. 2.19:

$$i\frac{\partial\psi_{j\sigma}(\mathbf{r},t)}{\partial t} = \left(-\frac{\nabla^2}{2} + v^{\text{s}}_{\sigma}(\mathbf{r},t)\right)\psi_{j\sigma}(\mathbf{r},t) \tag{2.32}$$

[1] also known as "terribly difficult darned fine theory", a phrase coined by André Bandrauk [81]

but here with a time-dependent external potential v_σ^{s} chosen to reproduce the exact electron densities of the interacting system. σ labels the spin state, either α- or β-spin. As in ground-state DFT, the potential comprises the electric field of the nuclei in the system, the exchange-correlation, and the Hartree potential of the electron density. Furthermore, an additional (commonly electric) field is included. Equations 2.32 can be used to propagate the system forward in time. Following the response of the electronic system then allows to calculate the time-dependent dipole moment and from its Fourier transform the optical absorption cross-section.

In contrast to ground state density functional theory, the potential is in principle a functional of the entire history of electron densities over time, the initial interacting wavefunction, and the initial Kohn-Sham wavefunction. Commonly, the adiabatic approximation is used, i.e., the exact, time-dependent exchange-correlation potential is substituted by the ground state exchange-correleation potential (also termed "adiabatic approximation"). This is exact for infinitely slowly varying external fields and has proven a good approximation also for realistic fields.

In common applications, instead of solving eqs. 2.32, linear response theory is used to obtain excitation energies, oscillator strengths, and properties of an excited state. [85] The first-order response of the electron density to an arbitrarily weak perturbation, commonly an optical field $\delta v_{\mathrm{ext},\sigma}$, is examined:

$$\delta n_\sigma(\mathbf{r},t) = \sum_\sigma \int dt' \int d^3r \chi_{\sigma\sigma'}[n_0](\mathbf{r},\mathbf{r}';t-t')\,\delta v_{\mathrm{ext},\sigma}(\mathbf{r}',t') \tag{2.33}$$

and for applications in Kohn-Sham DFT the field $\delta v_{\mathrm{ext},\sigma}$ is substituted by Kohn-Sham potential v_σ^{s} and the susceptibility $\chi_{\sigma\sigma'}$ by the Kohn-Sham response function $\chi^{\mathrm{s}}_{\sigma\sigma'}$. The response of the electron density $\delta n_\sigma(\mathbf{r},t)$ can also be written in frequency space, expanded into the basis of KS transitions:

$$\delta n_\sigma(\mathbf{r},\omega) = \sum_q \left(P_{q\sigma}(\omega)\,\psi^*_{q\sigma}(\mathbf{r}) + P_{\bar{q}\sigma}(\omega)\,\psi_{q\sigma}(\mathbf{r})\right) \tag{2.34}$$

q is a double-index denoting a transition from an occupied orbital i to an unoccupied orbital a, $q=(i,a)$ and correspondingly the opposite case $\bar{q}=(a,i)$. Together with the response of the KS potential eqs. 2.33 and 2.34 can be combined to yield coupled matrix equations:

$$\left\{\begin{bmatrix}\mathbf{A} & \mathbf{B}\\ \mathbf{B}^* & \mathbf{A}^*\end{bmatrix} - \omega\begin{bmatrix}-1 & 0\\ 0 & 1\end{bmatrix}\right\}\begin{bmatrix}\mathbf{X}\\ \mathbf{Y}\end{bmatrix} = -\begin{bmatrix}\delta\mathbf{v}\\ \delta\mathbf{v}^*\end{bmatrix} \tag{2.35}$$

that need to be solved iteratively. Out of the need to associate a physical interpretation with the terms in eqs. 2.35, **X** and **Y** are commonly referred to as excitations and de-excitations. They correspond to the perturbation in the density matrix **P**, with $X_{q\sigma} = P_{q\sigma}$ and $Y_{\bar{q}\sigma} = P_{\bar{q}\sigma}$. The matrices **A** and **B** are given through the response of the XC kernel f_{XC} to a perturbation:

$$A_{ia,jb} = \delta_{ij}\delta_{ab}\left(\epsilon_a - \epsilon_i\right) + (ia|jb) + (ia|f_{\mathrm{XC}}|jb) \tag{2.36}$$

$$B_{ia,jb} = (ia|bj) + (ia|f_{\mathrm{XC}}|bj) \tag{2.37}$$

The leading term in **A** is the difference in the orbital energies between occupied and unoccupied orbitals, ϵ_i and ϵ_a respectively, and the last terms are two-electron integrals in Mulliken notation. [1] The two-electron integrals in **A** and **B** correspond to the response of the XC potential to the external perturbation. In the adiabatic approximation this response is given by the second functional derivative of the energy functional. At the poles of the dynamic polarizability, i.e., when excitation energy corresponds to a resonance $\delta v = 0$ and eqs. 2.35 can be arranged to give the working equations of linear-response TDDFT:

$$\begin{bmatrix} \mathbf{A} & \mathbf{B} \\ \mathbf{B}^* & \mathbf{A}^* \end{bmatrix} \begin{bmatrix} \mathbf{X} \\ \mathbf{Y} \end{bmatrix} = \omega \begin{bmatrix} 1 & 0 \\ 0 & -1 \end{bmatrix} \begin{bmatrix} \mathbf{X} \\ \mathbf{Y} \end{bmatrix}. \tag{2.38}$$

From these equations excitation energies are calculated and corresponding oscillator strengths obey the Thomas-Reiche-Kuhn sum rule. [85] The neglect of the **B** matrix is known as the Tamm-Dancoff approximation and often leads to comparable results to TDDFT at reduced computational cost. [83]

Calculation of accurate properties in the excited state, like dipole moments or nuclear gradients, necessitates account of electronic relaxation upon excitation. [86] Properties in the excited state are therefore often distinguished into unrelaxed (directly from the solution of eq. 2.38) and relaxed variants. It is possible to reformulate TDDFT into a variational problem which also yields the above linear-response equation. [86, 87] From this formulation of TDDFT one can furthermore derive an additional set of, so-called, "z-vector" equations, solution of which yields relaxed properties (i.e., derivatives of excited-state properties with respect to an external perturbation).

[1] $(ij|kl) = \int\int d^3r d^3r' \psi_i^*(\mathbf{r})\,\psi_j(\mathbf{r})\,\frac{1}{|\mathbf{r}-\mathbf{r}'|}\psi_k^*(\mathbf{r}')\,\psi_l(\mathbf{r}')$

2.5 Extended systems

Treating extended systems, such as bulk water and water surfaces, requires the use of special computational methods. Three different approaches are briefly introduced in the following subsections.

2.5.1 Continuum solvation models

Efficient ways of including solvation effects have been developed in the context of dielectric continuum models, see for example reviews 88, 89 and references therein. These methods avoid explicit treatment of all molecular degrees of freedom of a solvent. The explicit solvent is substituted by a dielectric continuum responding to the charge density of the solute in form of an apparent surface-charge distribution at the interface between implicit solvent and explicit solute. The screening charge density $\sigma(\mathbf{r})$ is given by:

$$4\pi\varepsilon\sigma(\mathbf{r}) = (\varepsilon - 1)\,\mathbf{n}(\mathbf{r})\,\mathbf{E}(\mathbf{r}) \tag{2.39}$$

with $\mathbf{E}(\mathbf{r})$ the electric field inside the solute cavity, $\mathbf{n}(\mathbf{r})$ a surface normal, and ε the dielectric constant of the solvent. For arbitrarily shaped solutes, no closed, analytical solution to eq. 2.39 exists and different approximations have been suggested.

In this work, we employed models based on the screening in a perfect conductor (i.e., $\varepsilon = \infty$), in particular the conductor-like screening model (COSMO) [90] and the conductor-like polarizable continuum model (C-PCM) [91, 92]. The starting point for these models is the calculation of the screening energy ΔE of an arbitrary distribution of point charges q_i (collected in the vector $\mathbf{Q}$) [1] in a spherical cavity of radius R immersed in a dielectric continuum:

$$\Delta E = -\frac{1}{2}\mathbf{QDQ}, \tag{2.40}$$

$$\mathbf{D}_{ij} = \frac{R}{\sqrt{R^4 - 2R^2\mathbf{r}_i\mathbf{r}_j + r_i^2 r_j^2}}. \tag{2.41}$$

Vectors $\mathbf{r}_i$ denote distances of the charges q_i from the center of the sphere. The assumption of a spherical cavity is too severe as most solutes come in more complicated shapes. Thus, generalizations to arbitrary cavity shapes have been introduced with the help of algorithms that construct molecular surfaces according to the geometry of the solute and assumed radii of the constituting atoms (often (scaled) van-der-Waals-radii). For arbitrary surface shapes the charges in

[1] Generalization to continuous charge distributions is straightforward.

expression 2.40 are calculated on planar segments on the surface and further on approximated by point charges at the center of these surface segments. The screening energy is then given by the Coulomb interaction of the source charge distribution and the screening charges. The total energy is then calculated as the sum of the screening energy and the self-energy of all source charges and all surface charges. The screening charges are incorporated in the self-consistent field iterations of variational methods like Hartree-Fock or density functional theory in form of additional external fields.

An important modification is the use of a weakly ε-dependent correction for the treatment of non-conducting solvent media, i.e., common solvents as water and ethanol. For the model of point charges in a spherical cavity eq. 2.40 then changes to:

$$\Delta E = -f(\varepsilon)\,\mathbf{QDQ}. \tag{2.42}$$

The specific form of this so-called reduced screening boundary condition and its implied scaling factor $f(\varepsilon)$ depends on the implementation at hand. The form of the scaling factor is:

$$f(\varepsilon) = \frac{\varepsilon - 1}{\varepsilon + X}. \tag{2.43}$$

For the C-PCM model $X = 0.0$ corresponding to the monopole term in a multipole expansion of the solute's charge density and was chosen for compliance with Gauss's law and $X = 0.5$ in the COSMO model, corresponding to a dipole scaling factor. Both approximations generally work well for solvents with high dielectric constants.

An important modification was introduced to treat vertical, i.e., fast, electronic transitions in continuum models. [93] It is observed that the dielectric constant of a solvent can be split into a fast and a slow part, corresponding to electronic and nuclear response, respectively. For vertical transitions or ionization energies, only the electronic response is to be included as nuclear rearrangement is not possible on this time scale. This split treatment has been included in non-equilibrium variants of the continuum solvents.

The continuum solvation models work well for geometry optimization and energies of bulk-solvated species. Nevertheless, the use of these models always introduces an explicit interface which can lead to artifacts when performing molecular dynamics simulations.

2.5.2 Periodic boundary conditions

A conceptually simple, yet intriguing, way to treat bulk (and slab) systems is the introduction of periodic boundary conditions, i.e., replicating a small system peri-

odically in all three (or two) spatial directions. [46] Explicit interactions are then only included in form of so-called minimum images of the periodic unit cell. That is interactions are directly calculated for particles in range of half the length of the unit cell basis vectors within the unit cell and the closest periodic image. Further corrections for the periodic system are included in various ways. Of paramount importance is the explicit treatment of electrostatic interactions. Summation of coulombic interactions over all replicas of the unit cell is conditionally convergent, i.e., depends on the order of the explicit summation, and converges very slowly. To circumvent this issue, the class of Ewald summation techniques have been introduced. For a good review see, e.g., ref. 94 and references therein. Although originally developed in the context of periodic crystal lattices [95] it is nowadays commonly used for solids and liquids alike. The Ewald summation splits the $1/r$ operator of the Coulomb interaction into two parts by the same decomposition as for range-separated hybrid density functionals in eq. 2.26. The range-separation parameter is commonly denoted by α in literature when dealing with Ewald summation (and not μ as in range-separated hybrid density functionals). The range-separation is facilitated by the addition of Gaussian screening charge distributions (and corresponding canceling distributions) with a width of κ at the position of point charges q_i in the simulation cell. Electrostatics can thus be split into a quickly converging, direct sum within a pre-set cutoff and an also quickly converging sum in reciprocal space for the interaction of particles beyond the cutoff. The total electrostatic energy $E_{\mathrm{ES}}^{\mathrm{tot}}$ for a set of N point charges q_i located at $\mathbf{r}_i$, with r_{ij} the distance between two charges q_i and q_j, can then be written as:

$$E_{\mathrm{ES}}^{\mathrm{tot}} = E_{\mathrm{dir}} + E_{\mathrm{rec}} + E_0 \tag{2.44}$$

$$E_{\mathrm{dir}} = \frac{1}{2}\sum_{i,j=1}^{N}\sum_{\mathbf{n}\in\mathbb{Z}^3} q_i q_j \frac{\mathrm{erf}\left(\alpha r_{ij,\mathbf{n}}\right)}{r_{ij,\mathbf{n}}} \tag{2.45}$$

$$E_{\mathrm{rec}} = \frac{1}{2V_{\mathrm{box}}}\sum_{\mathbf{k}\neq\mathbf{0}}\frac{4\pi}{\kappa^2}\exp\left(-\kappa^2/4\alpha^2\right)\left|\bar{\rho}\left(\mathbf{k}\right)\right|^2 \tag{2.46}$$

$$E_0 = -\frac{\alpha}{\sqrt{\pi}}\sum_{i=1}^{N} q_i^2. \tag{2.47}$$

V_{box} is the volume of the unit cell, $\bar{\rho}$ is the Fourier transform of the real-space charge density ρ and $\mathbf{k}$ are reciprocal lattice vectors. Again, generalization to continuous charge densities is straightforward and is needed for use of the Ewald summation techniques in the context of ab initio molecular dynamics. More efficient treatment in the spirit of the Ewald summation techniques has been introduced through use of grid-based methods that show much better scaling with

system size. Examples are the particle-particle-particle-mesh, particle-mesh, and smooth particle-mesh Ewald summation techniques. [94] For non-neutral systems an additional term has to be included to avoid divergence of the Ewald summation. This correction corresponds to adding a uniform, neutralizing background charge to the system.

A simple approach to treat slab geometries is to increase the lateral dimension of the unit cell and separate the system from its periodic images. Accurate algorithms for descriptions of explicitly 2D-periodic systems have been developed in the context of wavelet-based Poisson solvers [96] and 2D periodic Ewald summation techniques [97], but go beyond the scope of this section. Periodic slab geometries with a net charge demand special attention. A neutralizing background charge can be added as in bulk systems. As a result the distribution of charged species between surface and bulk in 2D-periodic systems is biased by the homogeneously spread background charge in the inhomogeneous dielectric and corrections have been developed to unbias the distribution. [98]

For disordered systems (like liquids) that at maximum have a short-range order, but exhibit long-range disorder, a certain minimum size of the unit cell is required. Also, fluctuations in temperature and pressure depend on the system size and get smaller with increasing system size. For example, for simultaneously well described bulk and surface properties of a water/vapor interface, slab geometries with at least 200 water molecules are needed. [99] Converged number densities of bulk water in an NpT ensemble that compare well to experiment can be achieved with at least 60 water molecules. [100]

2.5.3 Combined quantum mechanics and molecular mechanics

The combination of quantum mechanics with molecular mechanics (QM/MM) originates from the necessity to treat systems of a minimum size. These systems easily get so large that they become prohibitively expensive for treatment with purely quantum-mechanical methods. The basic idea of QM/MM is to neglect the quantum-mechanical nature of a big part of the investigated system and treat this part with force-field based methods with pre-assigned partial charges, pairwise descriptions for van-der-Waals interactions, and (commonly) harmonic bond- and bending potentials (MM subsystem). [101] Only a small subsystem is then treated with quantum-mechanical methods in the field of the surrounding classical system (QM subsystem). The interaction between the two subsystems can be included via mutual electrostatic coupling, i.e., the Coulomb interaction between charge density of the quantum solute and the point charges surrounding

it.

In the specific implementation in the CP2K program suite that we used, the coupling between QM and MM subsystems that are in direct contact are included, as well as long-range corrections in form of the Ewald summation (see sec. 2.5.2). [102, 103] The total energy can then be written as a sum of the energy of the QM subsystem in the field of the MM charges, the energy of the MM subsystem, and a coupling term:

$$E_{\text{tot}}\left(\{\mathbf{R}_\alpha\},\{\mathbf{R}_a\}\right) = E^{\text{QM}}\left(\{\mathbf{R}_\alpha\}\right) + E^{\text{MM}}\left(\{\mathbf{R}_a\}\right) + E^{\text{QM/MM}}\left(\{\mathbf{R}_\alpha\},\{\mathbf{R}_a\}\right) \tag{2.48}$$

where $\mathbf{R}_\alpha$ denotes the positions of the QM nuclei and $\mathbf{R}_a$ of the MM nuclei. The QM subsystem is described using DFT methodology as implemented in the QUICKSTEP module of CP2K and the coupling energy between QM and MM subsystem $E^{\text{QM/MM}}$ is calculated as:

$$\begin{aligned} E^{\text{QM/MM}}\left(\{\mathbf{R}_\alpha\},\{\mathbf{R}_a\}\right) &= \frac{1}{2}\int\int \frac{\rho^{\text{MM}}\left(\mathbf{r},\{\mathbf{R}_a\}\right)\rho^{\text{QM}}\left(\mathbf{r}',\{\mathbf{R}_\alpha\}\right)}{|\mathbf{r}-\mathbf{r}'|} d^3r d^3r' \\ &+ \sum_{a\in MM}\sum_{\alpha\in QM} E_{\text{vdW}}\left(\{\mathbf{R}_\alpha\},\{\mathbf{R}_a\}\right). \end{aligned} \tag{2.49}$$

Here, $\rho^{\text{MM}}(\mathbf{r},\mathbf{r}_a)$ is the charge density of the MM subsystem and $\rho^{\text{QM}}(\mathbf{r}_\alpha,\mathbf{r}_a)$ is the total charge density of the QM part, including the nuclear charge density. The first term of eq. 2.49 is the electrostatic interaction of the QM and MM subsystems, whereas the second term, E_{vdW}, is the van-der-Waals interaction energy between all pairs of QM and MM atoms calculated by a pairwise interaction potential as, e.g., the 12-6 Lennard-Jones potential. To avoid the so-called "electron spill-out" problem, i.e., overpolarization of the QM charge density towards the QM/MM boundary if a point charge representation of $\rho^{\text{MM}}(\mathbf{r},\mathbf{r}_a)$ is used, the MM charge density is represented by Gaussian functions centered at the positions of the MM nuclei:

$$\rho\left(\mathbf{r},\mathbf{r}_a\right) = \frac{1}{\left(\sqrt{\pi}r_{\text{c},a}\right)^3}\exp\left(\left(-\left|\mathbf{r}-\mathbf{r}_a\right|/r_{\text{c},a}\right)^2\right) \tag{2.50}$$

The radius $r_{\text{c},a}$ is an atom-type specific parameter, often close to the covalent radius of the atom. These radii have to be tuned for the investigated system, e.g., against radial distribution functions of an equivalent system described only by MM. Smearing of the MM charges avoids the "spill-out" problem and can also be shown to effectively account for Pauli-repulsion effects. [104] The potential V_{MM} exerted on the QM charge density can then be incorporated into the external potential of a DFT calculation. Collocating this potential is computationally

expensive as it generally scales as the product of the number of MM nuclei and the number of grid points $N_{\mathrm{MM}} N_{\mathrm{grid}}$, where N_{MM} is easily on the order of a few thousand and N_{grid} on the order of a million points. In CP2K this is avoided by expanding the MM electrostatic potential of each MM nucleus into a set of N_{G} Gaussian functions as in eq. 2.51 with different widths G_{G} and corresponding normalization A_{G}, and a residual, smooth function R_{low}. The potential v_a of single Gaussian function as in eq. 2.50 is so given as:

$$v_a\left(\mathbf{r}, \mathbf{r}_a\right) = \frac{\operatorname{erf}\left(\left|\mathbf{r}-\mathbf{r}_a\right| / r_{\mathrm{c},a}\right)}{\left|\mathbf{r}-\mathbf{r}_a\right|} = \sum_{N_{\mathrm{G}}} A_{\mathrm{G}} \exp\left(-\left(\left|\mathbf{r}-\mathbf{r}_a\right| / G_{\mathrm{G}}\right)^2\right) + R_{\mathrm{low}}\left(\left|\mathbf{r}-\mathbf{r}_a\right|\right) \tag{2.51}$$

Then, each Gaussian function can be collocated on a separate grid of different density of grid points according to the width of the Gaussian, i.e., for a wide Gaussian a coarse grid is employed and for a tight Gaussian a fine grid. The residual function R_{low} is collocated on the coarsest grid level as it is constructed to be slowly varying. The data on the individual grids are then put together on the finest grid by interpolation with fast Fourier transform methods.

The expansion of the MM charge density and its electrostatic potential into a sum of Gaussian functions has the distinct advantage that it can be included in Ewald summation techniques. Thus, not just the direct coupling between the MM and QM subsystem can be evaluated, but also contributions arising due to a periodic charge density. The calculation of the MM potential in eq. 2.51 thus has to be performed over the periodic real-space lattice. Then the summation has the same convergence as the infinite sum in the Ewald summation scheme (see sec. 2.5.2). The radii r_{c} can be chosen to make the first part of the summation quickly convergent in real space, whereas the residual term R_{low} is a slowly varying function in real space. The latter property translates to a quickly decaying function in reciprocal space and hence R_{low} can be calculated efficiently by summation over only few reciprocal lattice vectors.

Within this general scheme it is also possible to include the coupling between periodic images of the QM subsystem. This is of particular importance for charged systems due to the long-ranged nature of the Coulomb potential. In CP2K in particular, the electrostatic potential acting on the QM subsystem can be modified by the potential of a model charge density that has the same multipole moments as the original QM charge density. The calculation of the model charge density was originally introduced to decouple periodic images in calculations using plane waves. [105] This decoupling of the periodic images has to be performed anyway in QM/MM calculations in CP2K because of the use of intrinsically periodic plane wave basis set. The potential from the model charge density

can then be re-incorporated into the electrostatic potential with periodicity of the full system (re-coupling).

2.6 Analysis

Many structural analyzes like radial distribution functions were developed in the context of spherical point particles. [46] An atom can be treated as point-like particle also in molecules. This makes sense not just for the nuclei, but also for the electronic distribution, which peaks at the corresponding positions of the nucleus and both core and electrons can be identified together as a point-like particle at the position of the nucleus. A hydrated electron, however, is one of the odd cases where one is interested in a species that is not associated with a specific nucleus and is far from being spherically distributed under finite temperature conditions. In our molecular dynamics simulations a restricted open-shell formalism was used (details see sec. 2.7), meaning that all electrons are treated as pairs and only the singly occupied molecular orbital is described separately. The hydrated electron is then identified as the spin density of the system and hence subsections below deal mainly with analysis of the spin density itself.

Center and extent of the spin density are given by standard moment analysis, sec. 2.6.1. We developed in this work a splitting scheme of the spin density into different parts, sec. 2.6.2. This was specifically designed for analysis of the hydrated electron and serves as semi-quantitative comparison for its structure in different environments. Furthermore, the so-called "instantaneous liquid interface" as introduced in ref. 106 is explained briefly in sec. 2.6.3 as it has been introduced quite recently and is needed for the dissection of the spin density at an interface. Lastly, the evaluation of excited state spin densities is presented in sec. 2.6.4.

For all the below presented analysis electron and spin density distribution were collected along ab initio molecular dynamics simulations in Gaussian cube file format [107]. These are plain text files that contain data points distributed over the unit cell of the simulation in form of voxels. That implies that every data point encompasses the same volume. Every integral over the cube files is calculated numerically using the mid-point rule.

2.6.1 Moment analysis of the spin distribution

The nth moment of the spin density $m(\mathbf{r})$ [1] about $\mathbf{c}$ is given by:

$$\mu_n = \int_\Omega (\mathbf{r} - \mathbf{c})^n m(\mathbf{r})\, d^3r. \tag{2.52}$$

The norm N of the spin density distribution $m(\mathbf{r})$ is the 0th moment. For the moment analysis of the hydrated electron the spin density is normalized to the 0th moment, which is only different from 1 due to numerical imprecision. The first moment μ_1 is used as the center of the spin density distribution $\mathbf{r}_\mathrm{c}$, with $\mathbf{c}$ being all zeros in eq. 2.52, and serves as point-particle descriptor of the hydrated electron in calculations of radial distribution functions. The radius of gyration r_g is used to quantify the extent of the spin density distribution with respect to its center $\mathbf{r}_\mathrm{c}$. As the second moment μ_2 represents a symmetric, real-valued matrix, we can determine its eigenvalues λ_1^2, λ_2^2, and λ_3^2. r_g is then evaluated as:

$$r_\mathrm{g} = \sqrt{\lambda_1^2 + \lambda_2^2 + \lambda_3^2} \tag{2.53}$$

or simply as the square root of the trace of μ_2 as it is invariant under a unitary transformation.

2.6.2 Dissection of the spin density distribution

The analysis presented in this section can be regarded as a population analysis of the spin density, specifically tailored to the hydrated electron. It is an artificial splitting that is only possible computationally and not experimentally observable. Experimentally only the full electron density is accessible. This is similar to atomic population analyzes that split the full electron density into atomic contributions. These are in principle capable of describing the charge transfer to the water molecules surrounding the hydrated electron, but will attribute all spin density $m(\mathbf{r})$ to the atoms surrounding the hydrated electron. Under the assumption that something like a "cavity" exists, as has been the picture of the hydrated electron over many decades, it is imperative to see how much of the hydrated electron is located within this cavity. Comparison of the absolute values from the below decomposition only makes sense for the hydrated electron in different situations like in bulk water and at the water/vapor interface.

First, the spin density located on water molecules is identified. A reference calculation is performed without the hydrated electron, at the geometry obtained from molecular dynamics including the hydrated electron. This is the neutral

[1] and in general any real-valued, continuous functions

reference system. The next step is to identify an isosurface of the electron density in the reference system that encompasses a certain amount of its electron density. A value of 90% of the total integrated electron density of the neutral reference system was chosen. [1] The fraction of the spin distribution attributed to water molecules is the part of $m(\mathbf{r})$ that is encompassed by the aforementioned isosurface. Secondly, in case an interface is present (in our simulations the water/vapor interface), the instantaneous liquid interface (sec. 2.6.3) is determined and the spin distribution located beyond this interface in the vapor phase is assigned to the "surface contribution". Thirdly, the Voroni polyhedron generated by the oxygen atom positions around the center of the spin density distribution is constructed. The spin density contained in this polyhedron is what we refer to as the "cavity contribution". The remaining unassigned spin density is located in interstitial spaces between water molecules and is called the "diffuse part" as these are places where the spin distribution overall attains comparably small values.

2.6.3 Instantaneous liquid interface

It is common to identify interfaces such as the water/vapor interface by Gibbs' dividing surface. This does not account for the instantaneous fluctuations of the molecular dynamics as it is calculated a posteriori to a simulation from the average density profile and is then taken as the plane at half the bulk density value. A flexible, molecularly based description of the water/vapor interface was introduced recently. [106] Here, the coarse-grained density $\bar{\rho}$ of the liquid is given as a scalar field constructed by the superposition of normalized Gaussian functions centered at the positions of the atoms i in the simulation. The coarse-grained density $\bar{\rho}$ is then:

$$\bar{\rho}(\mathbf{r}) = \sum_i \frac{1}{\left(\sqrt{2\pi}\zeta\right)^3} \exp\left(-\left|\mathbf{r}_i - \mathbf{r}\right|^2 / 2\zeta^2\right) \tag{2.54}$$

The parameter ζ has to be determined for the system under investigation. It has to be optimized to give as few voids as possible in the bulk of the liquid with the smallest possible ζ in eq. 2.54. One can then compute the scalar field $\bar{\rho}(\mathbf{r})$ and identify the instantaneous interface by an isosurface of $\bar{\rho}$ with a given value c. This value is set to half the bulk density. For the specific case of a water/vapor interface these parameters have been determined in the original publication and are $\zeta = 2.4$ Å for all oxygen atoms [2] and a value of $c = 0.016$ Å^{-3} for the

[1] The influence of this parameter on the overall analysis is shown in the supporting material of ref. 108.

[2] No Gaussian functions are located on the hydrogen atoms.

isosurface.

2.6.4 Excited state spin density

In the linear-response formulation of time-dependent density functional theory introduced in section 2.4 excitation energies and oscillator strengths can be calculated. From these calculations one also obtains coefficients of the unrelaxed density difference matrix U, i.e., how much electron density is transferred from, in the ground state calculation, occupied to unoccupied molecular orbitals:

$$U_{ab\sigma} = \frac{1}{2}\sum_{i}\left(x_{ia\sigma}x_{ib\sigma} + y_{ia\sigma}y_{ib\sigma}\right) \tag{2.55}$$

$$U_{ij\sigma} = -\frac{1}{2}\sum_{a}\left(x_{ia\sigma}x_{ja\sigma} + y_{ia\sigma}y_{ja\sigma}\right) \tag{2.56}$$

$$U_{ia\sigma} = U_{ai\sigma} = 0 \tag{2.57}$$

Occupied molecular orbitals are labeled with indices i and j and unoccupied orbitals with a and b. Equations are given in spin-polarized form with the corresponding index σ. The coefficients $x_{ia\sigma}$ and $y_{ia\sigma}$ are given as:

$$x_{ia\sigma} = X_{ia\sigma} + Y_{ia\sigma} \tag{2.58}$$

$$y_{ia\sigma} = X_{ia\sigma} - Y_{ia\sigma}. \tag{2.59}$$

$X_{ia\sigma}$ and $Y_{ia\sigma}$ are deformation densities and are given here in the nomenclature used in articles [83] and books [82] about TDDFT. Substituting eqs. 2.58 and 2.59 into eqs. 2.56 and 2.57 leads to:

$$U_{ab\sigma} = \sum_{i}\left(X_{ia\sigma}X_{ib\sigma} + Y_{ia\sigma}Y_{ib\sigma}\right) \tag{2.60}$$

$$U_{ij\sigma} = -\sum_{a}\left(X_{ia\sigma}X_{ja\sigma} + Y_{ia\sigma}Y_{ja\sigma}\right) \tag{2.61}$$

which can then directly be seen to be the difference in the density matrix upon excitation. The unrelaxed difference density n_{u} can then be constructed as:

$$n_{\mathrm{u}}\left(\mathbf{r}\right) = \sum_{rs\sigma} U_{rs\sigma}\psi^{*}_{r\sigma}\left(\mathbf{r}\right)\psi_{s\sigma}\left(\mathbf{r}\right), \tag{2.62}$$

with indices r and s running over all occupied and unoccupied molecular orbitals. As mentioned in sec. 2.4 the linear response theory and the reconstruction of the excited state density does not take into account any electronic relaxation upon excitation. The change in electron density due to electronic relaxation n_{r} can be calculated [86, 87] as pointed out in sec. 2.4. One can then reconstruct the full

electron density in the excited state n_{exc} from the ground-state electron density n_{gs}:

$$n_{\mathrm{exc}} = n_{\mathrm{gs}} + n_{\mathrm{u}} + n_{\mathrm{r}}. \tag{2.63}$$

In the case of the TDDFT calculations applied to structures of the hydrated electron only excitations from the singly occupied molecular orbital were observed. This, together with the fact that no significant spin-contamination was observed, allows us to reconstruct the spin density of the excited state m_{exc} simply as:

$$m_{\mathrm{exc}}(\mathbf{r}) = m_{\mathrm{gs}}(\mathbf{r}) + n_{\mathrm{u}}(\mathbf{r}) + n_{\mathrm{r}}(\mathbf{r}). \tag{2.64}$$

2.7 Practical aspects and computational setup

In this section the practical schemes of the computations are detailed, i.e., the approximations explained in the preceding sections are put together in their respective context to provide working computational setups. Each type of calculation, be it ab initio molecular dynamics simulations, minimum energy path optimization, or time-dependent density functional calculations is kept as consistent as possible with the respective other types of calculations. Generally, the force calculations for the molecular dynamics simulations, and structure and MEP optimizations use Born-Oppenheimer and adiabatic approximations as described in sec. 2.2. The Born-Oppenheimer potential energy E_k is described differently though in these calculations. Due to reasons of computational efficiency, e.g., different basis sets were used for different systems. The density functional of choice differs between AIMD and TDDFT due to spurious charge-transfer excitations observed in TDDFT calculations with regular GGA density functionals. This is a common observation for GGA density functionals, see, e.g., refs. 83, 109.

We start with the description of the setup for obtaining minimum energy structures and optimizations of minimum energy paths in sec. 2.7.1, followed by details on the ab initio molecular dynamics in sec. 2.7.2, and close with the setup of the TDDFT calculations in sec. 2.7.3.

2.7.1 Minimum energy structures and reaction path optimizations

Geometry optimizations of individual structures were performed with the Broyden-Fletcher-Goldfarb-Shanno algorithm as implemented in the Atomic Simulation Environment (ASE). [110] For the minimum energy path calculations, geometries of the reactants and products were optimized and an intial guess for the band was obtained from linear interpolation between the structures. Minimum

energy paths were obtained by first optimizing the band with the IT-NEB. A climbing image was included after convergence of the IT-NEB calculation and the band was again optimized to obtain the correct transition state. Optimizations of the bands were performed in ASE with the FIRE optimization when post-Hartree-Fock methods were used to calculate forces and with the BAND module in CP2K with a projected velocity Verlet optimizer for the band optimization with forces from DFT as described in the next section (only the quantum mechanics part).

Forces within the adiabatic and Born-Oppenheimer approximations were calculated with second-order Møller-Plesset perturbation theory on a Hartree-Fock reference wavefunction (MP2). For structures presented in sec. 3.1 the resolution of identity was used and compares well with plain MP2. RI-MP2 calculations were performed with the TURBOMOLE program package. [111] The wavefunction was expanded into atom-centered dual-ζ basis sets with polarization and diffuse functions (aug-cc-pVDZ). [112] For the systems presented in sec. 3.2 the MEPs were optimized with plain MP2 as implemented in ORCA [113] and the wavefunction was also expanded into a double-ζ basis set with polarization and diffuse basis functions on all atoms (6-31++G**). [114, 115] Basis sets used in sec. 3.1 and sec. 3.2 do not differ significantly in the relative energetics in the band optimization. The 6-31++G** basis set was more efficient for the calculations of the larger cluster system in sec 3.2. Also, the cluster systems in sec. 3.2 were embedded in a conductor-like solvent model for optimization and in a non-equilibrium variant for calculation of vertical detachment energies and optical spectra (see sec. 2.7.3).

2.7.2 Ab initio molecular dynamics simulations

All molecular dynamics simulations of extended systems were performed with the QM/MM module of CP2K. Input structures were taken from force-field molecular dynamics (FFMD) simulations of 1024 water molecules described by an extended simple point charge (SPC/E) model. The bulk water systems were equilibrated in the canonical, NpT, ensemble using both thermostat [116] and barostat [117] resulting in densities around 1 g/cm^3 (cubic unit cell with side length of 31 Å). For simulations of a water slab the z-dimension of the unit cell was elongated to 100 Å and the system was again equilibrated, but only coupled to a thermostat [116] (i.e., NVT ensemble). These calculations were performed with the GROMACS program. [118]

Several QM/MM molecular dynamics simulations were conducted of an excess electron in both bulk and slab geometries of water. The QM system was either

located in the water bulk or at the surface of the water slab. Statistics were collected along trajectories of in total 10 ps simulation time each. In the production QM/MM simulations QM and MM subsystems were coupled electrostatically and also the periodicity of the QM subsystem was taken into account. Periodic electrostatics were calculated using the smooth particle-mesh Ewald summation technique. [119] Newton's equations of motion were integrated with the velocity Verlet propagator coupled to a global thermostat [116]. Again, point charges and Lennard-Jones parameter from the SPC/E model were used to obtain forces on the MM subsystem and describe non-bonded interactions between QM and MM subsystem. The covalent radii of the hydrogen atoms in the MM subsystem were 0.44 Å and those of oxygen atoms 0.78 Å. These parameters lead to radial distribution functions between QM and MM subsystem comparable to those from pure force-field calculations for the flexible variant of the SPC/E water model we used. The wavefunction of the QM subsystem was expanded into a triple-ζ basis set with two polarization functions (molopt-TZV2P). [120] The basis set was specifically optimized for condensed phase systems, both with respect to computational efficiency and accuracy. An additional set of space-fixed, diffuse functions was placed in the middle of the QM subsystem to support the diffuse parts of the hydrated electron (denoted as GGG, "grid of Gaussian ghosts"). Each of these diffuse functions is spherically symmetric and constructed from single Gaussian function with an exponent of 0.1 a.u. The kinetic energy cutoff for the auxiliary plane-wave basis set was 280 Ry throughout the calculations. The collocation of the electronic density on the corresponding grid was done using 4 multigrids with different cutoffs for efficient calculations. All 1s core-electrons were replaced by relativistic pseudopotentials of Goedecker-Teter-Hutter type. [63] Forces on the QM atoms were obtained from the combined Becke exchange [121] and the Lee-Yang-Parr correlation functional (BLYP) [122]. The density functional was augmented with a semi-empirical self-interaction correction (SIC). Parameters for the SIC were $a = 0.3$ and $b = 0.2$. The results compare well with results from RI-MP2 calculations of MEPs (see sec. 3.1). For calculation of the exchange-correlation potential on a grid, the density was smoothed with a nearest-neighbor method with 20 points and the derivatives were smoothed using cubic splines. This was necessary for the combination of kinetic energy cutoff of the plane-wave basis set and BLYP density functional. The smoothing procedures remove artifacts in the exchange-correlation potential in the vicinity of the core region and provide results comparable to much higher (and much more costly) plane-wave cutoffs. [123] An additional, semi-empirical term was included to effectively account for dispersion interactions between the nuclei, but had no direct influence on the electron density. [124] The combination of BLYP density functional and aforementioned

dispersion correction was shown to give water structure and number densities close to experimental references. [125] In all the simulations the ASPC algorithm in third order was used for wavefunction extrapolation together with the orbital transformation method for wavefunction optimization and a preconditioner for the minimization constructed from a Cholesky inversion of the overlap and kinetic energy matrices. The convergence criterion of the wavefunction optimization was 10^{-6} a.u. for forces on each orbital.

2.7.3 Optical properties

Optical absorption spectra were calculated with TDDFT in its fully spin-polarized, linear response formalism. Bulk and slab geometries were extracted from the molecular dynamics simulations and similarly sized QM subsystems were used (either the same size or larger). The MM subsystem was described by point charges from a simple point charge model (SPC). [126] As we are currently unaware of an implementation that explicitly treats periodic QM/MM systems in the context of TDDFT, the unit cell was simply replicated and included as point charges in the calculation. For production runs different density functionals were used. Long-range corrected hybrid density functionals LRC-BLYP [72] and LRC-μBOP [127] were used for equilibrium spectra (secs. 3.2 and 3.6). The Tamm-Dancoff approximation was used for all the final equilibrium spectra. Along trajectories after vertical attachment of an excess electron to a neat water system, the B3LYP [128, 129] density functional was used (sec. 3.7). For QM/MM calculations a basis set with polarization functions only on the heavy nuclei was used (6-31++G*). [114, 115] In small cluster systems, the wavefunction was expanded into a double-ζ basis set with polarization and diffuse functions on all atoms (6-31++G**).

TDDFT calculations were performed with NWChem [130], QChem [131] and also Gaussian 09 [107]. Both NWChem and QChem were used for the QM/MM TDDFT calculations and Gaussian 09 was used in the context of small, embedded cluster systems coupled to a non-equilibrium solvent model [93].

Chapter 3

Results

This chapter provides an overview of the publications that comprise this thesis. Each publication is introduced in brief and key points are highlighted. In case previously unpublished results are included, this is highlighted. All presented papers are attached in full.

The ordering corresponds to increasing system sizes investigated and complexity of the topic of the publications. The first two publications deal with cluster models of the hydrated electron and their reactivity, secs. 3.1 and 3.2. Two publications about the bulk- (sec. 3.3) and surface-solvation (sec. 3.4) of an excess electron follow. The next section gives a brief introduction to a review article on theoretical description of ions at the water/vapor interface, containing as a case study a discussion of the similarity of bulk- and surface-hydrated electron and implications for its surface propensity (sec. 3.5). We finish with two publications about optical properties of the hydrated electron, in thermal equilibrium (sec. 3.6) and after attachment of an excess electron to bulk water (sec. 3.7).

3.1 From a localized H_3O radical to a delocalized $H_3O^+ \cdots e^-$ solvent-separated pair by sequential hydration

Two issues are addressed in this publication. [132] First, the change in electronic structure upon microsolvation of an H_3O radical and second, the corresponding change in reactivity and similarity to that of a hydrated electron.

Fig. 3.1 shows optimized molecular geometries of clusters investigated in this publication together with isosurfaces of the spin density. Mimicking bulk solvation of H_3O by adding more water molecules to the isolated H_3O moiety at the dangling OH bonds, as shown in Fig. 3.1, leads to the formation of three hydrogen bonds with H_3O^+ acting as donor and water molecules as acceptors. In the isolated H_3O radical the spin density is located mainly on the hydrogen atoms. Adding more water molecules leads to a shift of the spin density towards the dangling OH-bonds of the water molecules and between them. The addition of only one water molecule donating a hydrogen bond to the H_3O moiety does not lead to a significant change in electronic structure. If a single water molecule is added, accepting a hydrogen bond from H_3O, the H_3O moiety still resembles a H_3O radical, with the spin density located mainly on the two dangling OH of H_3O. The latter structure is lower in energy than the former by about 0.3 eV. Thus the addition of a hydrogen bond donated by H_3O is favored compared to the inverse case. Upon further addition of water molecules the spin density shifts towards the dangling OH bonds of the water molecules. The transition to a hydrated H_3O^+ cation and a hydrated electron in form of a solvent-separated pair is complete after the addition of three water molecules accepting hydrogen bonds from the H_3O moiety. The change in electronic structure is accompanied by a change in VDE from 5.9 eV to 4.1 eV in $H_3O^+(H_2O)_3e^-$. The latter value is close to the VDE of a bulk-hydrated electron of 3.3 to 3.6 eV [26, 27, 28, 29], with additional stabilization in the small model system from the positive charge on H_3O^+. Without the stabilization due to the hydronium cation, the VDE of an isolated system of four water molecules and an excess electron is about 0.2 eV. [34]

The change in character from a localized H_3O radical to a model of the hydrated electron ($H_3O^+(H_2O)_3e^-$) is accompanied by a change in reactivity. The isolated H_3O radical dissociates by cleavage of one of its OH-bonds upon formation of hydrogen and water. The minimum energy paths for this process are comparable between RI-MP2, CCSD(T), and CASPT2 (CASPT2 data from ref. 133). Neglect of dynamic correlation effects (MEP calculated with UHF) results in a higher barrier for the reaction. These two observations illustrate that

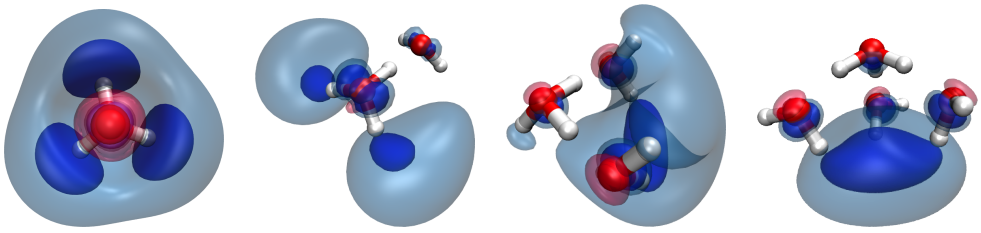

Figure 3.1: Minimum energy structures of isolated clusters $H_3O^+(H_2O)_n \cdots e^-$ with $n = 0 - 3$ increasing from left to right. Vertical detachment energies of the respective structures are given below the individual pictures. Isosurfaces of the spin density are shown at ± 0.001 a_0^{-1} (transparent) and ± 0.003 $a_0{}^{-1}$ (diffuse). Red isosurfaces correspond to negative and blue isosurface to positive isovalues.

treatment of dynamic correlation effects is important and sufficient at the level of RI-MP2 and that no significant multi-determinantal character is observed. Clusters containing one additional H_2O molecule decompose similarly to the isolated H_3O radical as the H_3O moiety still resembles an H_3O radical as can be seen in Fig. 3.1. As soon as two or three water molecules are added to the H_3O moiety the reactivity changes towards the recombination of a hydrated proton and electron. One proton initially located on the H_3O moiety transfers to one of the water molecules and then one proton of the corresponding water molecule recombines with the excess electron to form a hydrogen atom. During the reaction the spin density becomes compact at the transition state. This is similar to what has been observed in medium-sized clusters for this recombination reaction. [134] The small model system works well, because the solvation structure is close to the situation in bulk water both for a hydronium cation and an excess electron.

Fig. 3.2 shows minimum energy paths for the recombination reaction of a proton with the hydrated electron in $H_3O^+(H_2O)_3e^-$ obtained with different methods. The paths were calculated independently with forces from DFT with optimized SIC parameters (blue) and RI-MP2 (black) (see sec. 2.7 for details). Both paths have comparable relative energetics in the region of reactant state and the barrier for the reaction. The products of the reaction are overstabilized by the DFT setup by about 0.15 eV. The minimum energy paths were also used to re-evaluate the DFT methodology in terms of basis set and SIC parametrization. Fig. 3.2 also shows energies re-evaluated with different DFT setups along the MEP optimized with SIC($a = 0.3$, $b = 0.2$) and molopt-TZV2P with GGG basis set. Neglecting the SIC (red) leads to an artificial destabilization of the hydrogen atom and shifted relative energetics that favor the reactant state. The original parametrization of the SIC($a = 0.2$, $b = 0.0$) [68] (green) underestimates the barrier height of the reaction and stabilizes the products even further than with SIC($a = 0.3$, $b = 0.2$). The inclusion of diffuse basis functions is needed as

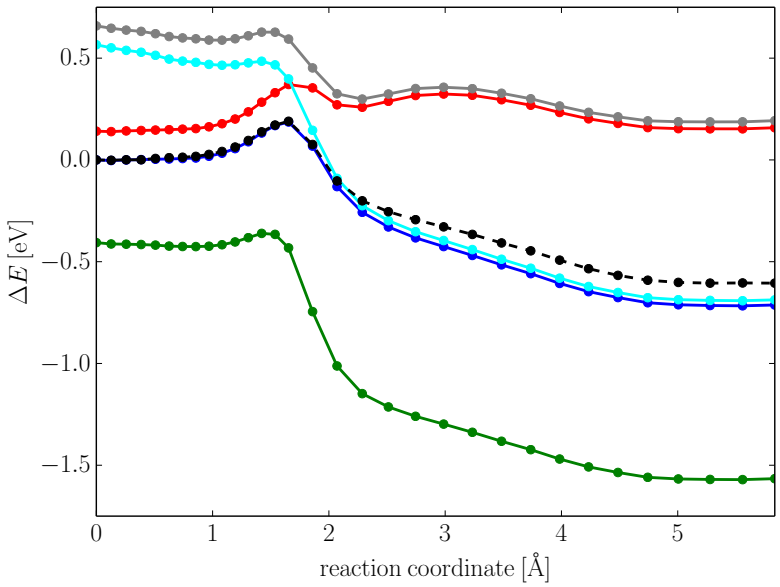

Figure 3.2: Energies along the minimum energy path of hydrogen formation in $H_3O^+(H_2O)_3e^-$ (blue line, calculated with molopt-TZV2P basis + additional space-fixed basis set GGG) and energies re-evaluated along this path with different basis sets and parameters for the self-interaction correction (solid lines). Three paths with molopt-TZV2P and GGG basis set were calculated with SIC($a = 0.3$, $b = 0.2$) (blue), SIC($a = 0.2$, $b = 0.0$) (in green) and no SIC (red). Path with only molopt-TZV2P basis set and SIC($a = 0.3$, $b = 0.2$) in cyan and with molopt-TZV2P basis set and no SIC in gray. For comparison the path independently calculated with RI-MP2 and aug-cc-pVDZ basis set is shown as dashed, black line.

the excess electron localizes to a large extent between the molecules. Without the additional set of diffuse basis functions the process of hydrogen formation is barrier-less (cyan curve). Additionally ignoring the SIC leads to correct trends in the relative energetics and a barrier for the reaction due to fortuitous error canceling (gray).

The RI-MP2 MEP presented here compares well to previously reported reaction profiles calculated with multi-reference methods including treatment of dynamic correlation effects. [133] This, and the good correspondence between optimized DFT setup and RI-MP2 calculations led to the choice of SIC parameters and basis set throughout this work.

3.2 Embedded cluster models for reactivity of the hydrated electron

Similarly to the previous section, this publication [135] addresses model systems of the hydrated electron and their reactivity. In contrast to the previous section the model systems considered here are immersed in a continuum solvation environment. This way, we can obtain stable and localized strutures of the hydrated electron in small cluster systems of a few water molecules. It has been a controversial issue whether the hydrated electron at ambient conditions is solvated in its first solvent shell by four or six water molecules. Experimental measurements in concentrated alkaline glasses at low temperatures suggested a coordination of the excess electron by six water molecules. [40] Computational studies supported this claim [136] or could not locate a stable minimum for a four-fold coordinated excess electron [137]. One-electron pseudopotential models yield mainly a coordination number of four water molecules in the first solvent shell around a bulk-hydrated electron, but some yielded the number of six. [33] We were able to obtain minimum energy structures for systems with both four and six water molecules solvating an excess electron. The two minimum energy structures of $(H_2O)_4^-$ and $(H_2O)_6^-$ are shown in Fig. 3.3. In terms of experimental observables these structures do not differ significantly. VDEs are similar for both structures, 2.9 eV for $(H_2O)_4^-$ and 3.2 eV for $(H_2O)_6^-$. The first three excitation energies are similar as well. The first excited state for $(H_2O)_4^-$ is at 1.5 eV and for $(H_2O)_6^-$ at 1.7 eV. The next two higher lying states are degenerate for both structures and are at 1.9 eV.

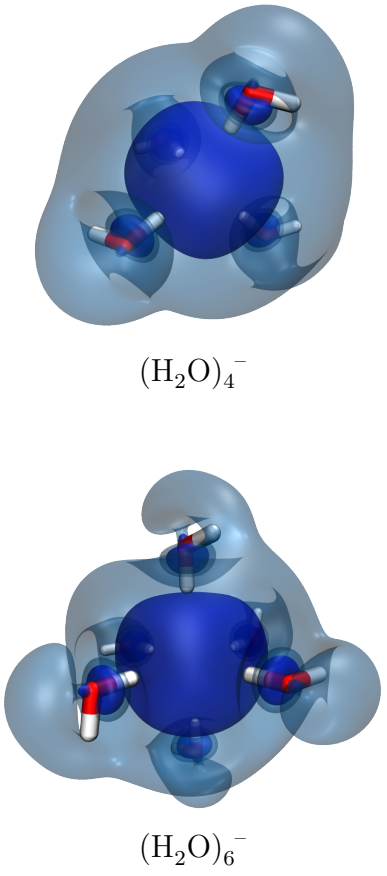

$(H_2O)_4^-$

$(H_2O)_6^-$

Figure 3.3: D_{2d}-symmetrical minimum structure of $(H_2O)_4^-$ (top) and S_6-symmetrical minimum structure of $(H_2O)_6^-$ (bottom) embedded in a conductor-like screening model. Isosurfaces of the spin density shown in blue at 0.001 a_0^{-1} (diffuse) and 0.0001 a_0^{-1} (transparent).

Division of the spin density according to the scheme in sec. 2.6.2 shows no significant difference between the two model systems. About half of the spin density is located within a cavity, about a tenth on water molecules, and 40 % are within

interstitial space. The diffuse contribution is overestimated and the contribution on water molecules underestimated because explicit solvation is missing beyond the first solvent shell around the excess electron.

The recombination reaction between a hydrated proton and electron was modeled in similarly sized, embedded cluster models. Structures were prepared from the optimized geometries shown in Fig. 3.3 by addition of H_3O^+ and additional water molecules. No stable structure could be obtained for a hydronium cation solvated at the six-fold coordinated excess electron. In preparatory energy minimizations positions of the oxygen atoms forming the solvation cage of the excess electron were fixed and only relaxation of hydrogen atoms and H_3O^+ was allowed. Energy minimization started from these pre-optimized structures relaxed to structures with four-fold coordination of the excess electron. In the optimized structures the excess electron was either solvated by four water molecules or three water molecules and the hydronium cation. This is an indication that including further solvation shells beyond the first one leads to a four-fold coordinated excess electron. Final MEPs for the recombination reaction were calculated for a cluster consisting of six water molecules, a hydronium cation and an excess electron. The excess electron is four-fold coordinated by water molecules. The H_3O^+ is coordinated to one water molecule directly solvating the excess electron and two water molecules solvating the solvation cage of the excess electron. The reaction itself then proceeds in a comparable manner as before; a proton is transferred from the hydronium cation to one of the water molecules solvating the excess electron followed by a proton transfer from the newly formed hydronium to the excess electron under formation of hydrogen and water. One-to-one comparison of this reaction model and the $H_3O^+(H_2O)_3e^-$ model (sec. 3.1) is difficult quantitatively due to the different solvation environments and cluster sizes. A compression of the solvation cage and thus also the spin density can be observed at the transition state of the reaction, as for the $H_3O^+(H_2O)_3e^-$ model. The barrier of the process is higher by 0.1 eV than for the isolated cluster system $H_3O^+(H_2O)_3e^-$ and the relative energies of reactants and products are shifted due to the stronger solvation in the larger cluster models and additional stabilization of the reactants by the continuum solvation model.

A second reaction investigated in this study was the addition of the excess electron to an N_2O molecule coordinated to the solvation cage pertinent to the hydrated electron. This reaction is used in experimental studies to scavenge hydrated electrons and form ·OH radicals. [138] The addition of an excess electron to N_2O leads to the formation of ·OH radical and OH^- anion:

$$N_2O_{aq} + {e_{aq}}^- \longrightarrow N_2 + {OH_{aq}}^{\cdot} + {OH_{aq}}^- \tag{3.1}$$

The reaction is close to being diffusion-limited. However, it is not truly diffusion-limited due to a barrier associated with desolvation of the hydrated electron. [139] Several clusters were optimized with N_2O attached to the solvation cage and also including several more water molecules solvating the N_2O. The geometry optimizations all led to transfer of the excess electron to the N_2O moiety under formation of a bent N_2O^- anion. The reaction paths obtained for this species are very similar to those of an N_2O^- anion solvated solely in a continuum solvation model. [139] A small barrier of 0.1 eV, associated with the cleavage of NO, is present and subsequent stabilization is accompanied by rearrangement of water molecules solvating the O^- anion. Modeling of this reaction including the actual separated species thus requires larger systems to completely solvate both excess electron and N_2O. A further reaction between water and O^- is expected and would produce $^{\cdot}OH$ radical and OH^- anion [1], but was not observed in the cluster systems.

[1] Only at high pH, pH≥12, the solvated O^- anion can be observed. [3]

3.3 Unraveling the complex nature of the hydrated electron

The traditional picture of the hydrated electron is that of an excess electron located in a polarized cavity, i.e., space not occupied by water molecules, with OH bonds of water pointing towards the center of the cavity. This model was questioned recently by simulations of a specific parametrization of a one-electron pseudopotential that predicts that the hydrated electron would not occupy a cavity, but would rather be delocalized around a region of enhanced water density. [38] We performed QM/MM molecular dynamics simulations of a bulk-hydrated electron, among other things, to address this issue. [108] To be as unbiased as possible towards the discussion in the literature, a single excess electron was attached to structures from molecular dynamics simulations of neat water obtained with the same QM/MM methodology. The attachment of the electron is simply performed by decreasing the charge by one in the input and following the subsequent molecular dynamics. The excess electron initially delocalizes over the QM region but forms within a few picoseconds structures that resemble the traditional picture of an electron solvated in a cavity, as depicted in Fig. 3.4. About four

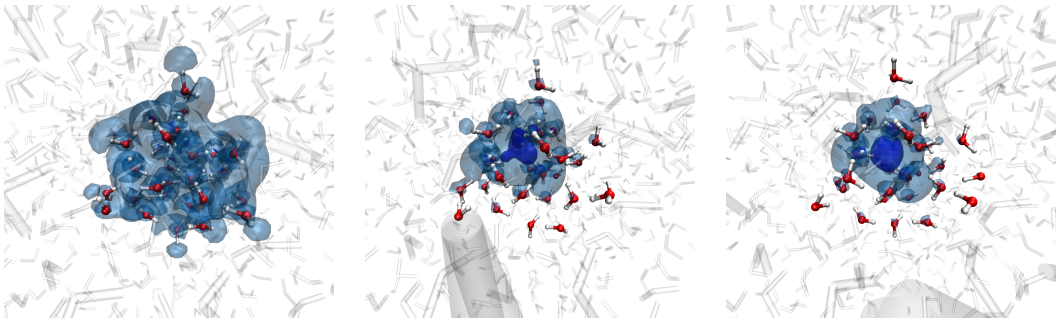

0 ps 1.5 ps 3 ps

Figure 3.4: Snapshots after decreasing charge of neat water QM/MM system by one and follow-up dynamics at 0 ps, 1.5 ps and 3 ps. Water molecules treated with QM methodology are shown as opaque balls and sticks and water molecules treated with MM methodology as transparent sticks. Spin density is depicted as isosurfaces at values of 0.0001 a_0^{-1} (transparent blue) and 0.001 a_0^{-1} (diffuse blue).

water molecules are on average located within the first solvent shell, which compares well with many of the one-electron pseudopotential calculations [33] and the model systems in sec. 3.2. This number was obtained from integrating the radial distribution functions of oxygen and hydrogen atoms up to their respective first minima. The RDFs indicate zero distribution of hydrogen atoms up to 0.6 Å and of oxygen atoms up to 1.6 Å distance from the center of the spin density distribution. Together with the localization depicted in Fig. 3.4 this is a very strong indication of the presence of a cavity. The use of RDFs implies the treatment

of the hydrated electron as a spherical point particle with a well-defined center. This is a somewhat oversimplified representation of the hydrated electron as it is far from spherical at each instant in the molecular dynamics simulations and also rather diffuse, as can be seen from the snapshot at 3 ps in Fig. 3.4. Only upon averaging the structure over the whole trajectory one would obtain a spherically symmetric picture of the hydrated electron. The hydrated electron is intrinsically coupled to all other electrons in the system and important contributions to its structure and energetics arise from the charge transfer of parts of the excess electron to the surrounding water molecules. From our spin decomposition scheme explained in sec. 2.6.2 one can determine that about 40 % of the spin density are located within the cavity, about 25 % on the water molecules and about 35 % within interstitial space between the water molecules. Although the part of the hydrated electron located in a cavity is larger than all other parts individually, it contributes less than half to the whole spin density and the large amount of the excess electron located on water molecules indicates that a treatment of the species in full detail requires an approach that includes the quantum nature of the water molecules. Spin density located in the cavity has higher values in a smaller volume than the other two parts which contribute with smaller values over a larger volume. Hence the large contributions outside of the cavity are a mere volume effect.

The hydrated electron in our simulations also reproduces several experimental quantities. In particular, the radius of gyration r_g is on average about 2.8 Å (thermal spread about 0.4 Å) while from moment analysis of the experimental, optical absorption spectra one can determine an r_g of about 2.4 Å. [14] Also, the optical absorption spectrum is well reproduced as detailed in sec. 3.6. The vertical detachment energies are on average 3 eV (thermal spread about 0.5 eV) while the experimental value is between 3.3 and 3.6 eV. As previously reported, the size and vertical detachment energy show an anti-correlation, i.e., the larger the electron in size, the weaker it is bound and vice versa. [22]

These simulations highlight the complex character of the hydrated electron. Using the ab initio description a picture of the hydrated electron emerges that is somewhat between the results from different one-electron pseudopotential calculations. A cavity is present, as in many of the pseudopotential calculations [33], but the ab initio description also shows a certain similarity to a delocalized electron [38] due to its significant contributions from the diffuse, interstitial parts and overlap with water molecules.

3.4 Electron at the surface of water: Dehydrated or not?

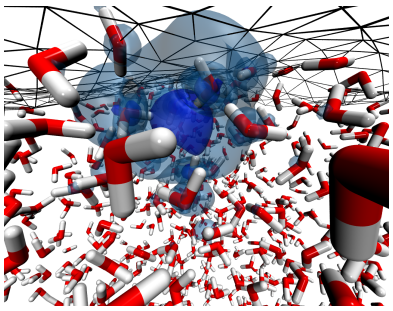

Figure 3.5: Snapshot of an excess electron solvated at the water/vapor interface. Black wireframe depicts the instantaneous liquid interface and isosurfaces of the spin density are shown at 0.0001 a_0^{-1} (transparent blue) and 0.001 a_0^{-1} (diffuse blue).

The hydrated electron is a highly polarizable charged particle due to the lack of an associated nucleus and it is known that large and polarizable ions have a propensity to accumulate at the water/vapor interface. [140] Nevertheless, the view of the hydrated electron at the water/vapor interface is not well established and computational studies have mainly focused on cluster systems or liquid bulk water. One study using one-electron pseudopotential description showed that an excess electron attached to neutral water system localizes to the interface and subsequently transfers to the bulk interior. [141] We reported simulations of a hydrated electron at the water surface [142] with the same QM/MM methodology as before for the bulk-hydrated electron, see sec. 3.3.

Neat water simulations were performed, now with the QM subsystem directly being part of the water surface. Decreasing the charge of the QM system by one led to an initial attachment of the excess electron in a delocalized fashion, which quickly localized (within 1-2 ps) to form a hydrated electron solvated, at least partially, in a cavity. The properties of the hydrated electron at the water/vapor interface are very similar to that in bulk water solution. The excess electron is comparable in size ($r_g = 2.9$ Å) and has a similar VDE (3.3 eV) to an excess electron in bulk water. [1] No stable low-binding isomers with a VDE on the order of 1.6 eV as suggested in ref. 28 were observed. The anti-correlation of size of the hydrated electron and its binding energy is observed as in bulk water [108] and in anionic water clusters [22].

The average solvation structure of the excess electron at the water surface is similar to that of a bulk-hydrated electron with about four water molecules in its first solvent shell. Due to the flexible/polarizable nature of the hydrated electron, large fluctuations in the spin density can be observed and hence also in the parts

[1] The inconsistency of a similarly sized excess electron at the water surface with higher vertical detachment energy compared to the simulations of the hydrated electron in bulk water is due to the different boundary conditions in simulations of bulk and slab geometries. For more information see sec. 4.1.

protruding into vapor phase. Compared to the bulk-hydrated electron, only minor differences are observed in parts of the spin density within the cavity, on the water molecules, and in the diffuse part. All decrease by about 3-4 % compared to the hydrated electron in bulk water, due to the anisotropy of the water/vapor interface and thus the part of the spin density protruding into the vapor phase. The latter part amounts on average to 11 %. Fig. 3.6 shows the percentage of spin density in the vapor phase in dependence of the distance of the center of the spin density distribution from the instantaneous liquid interface. The hydrated electron is mainly located between 1 and 2.5 Å from the instantaneous interface with only about 10 % or less of its spin density protruding into the vapor phase. Rarely, the electron is closer to the interface, but if so, the spin density in the vapor phase can gain up to 30 %. The inset of Fig. 3.6 shows correlated distributions of the VDE of the hydrated electron and its distance to the surface of water. No systematic correlation is observed for these two quantities. This is in stark contrast to the suggestion that the hydrated electron at the water surface would be weakly bound (1.6 eV) [28].

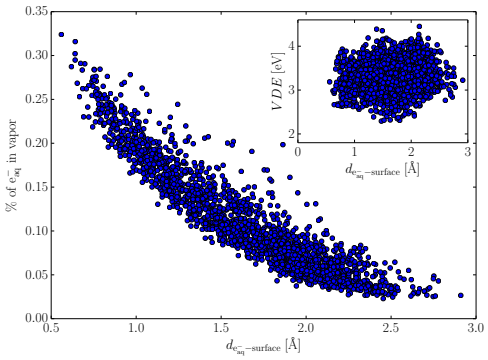

Figure 3.6: Correlated distributions of distance of hydrated electron to instantaneous liquid interface $d_{e^-_{aq}-surface}$ and percentage of spin density protruding into vapor phase. Inset shows correlated distributions of $d_{e^-_{aq}-surface}$ and vertical detachment energy VDE.

In summary, an excess electron, when solvated at the water/vapor interface, is structurally and energetically very similar to that of a bulk-hydrated electron. The first solvation shell is kept upon surface-hydration and only starting from the second solvation shell the anisotropy due to the interface present causes changes.

3.5 Charges at aqueous interfaces: Development of computational approaches in direct contact with experiment

This review [143] highlights some of the latest developments in molecular dynamics simulations of ions in solutions with emphasis on the behavior of different ions with respect to interfacial hydration (in particular at the water/vapor interface). Traditionally, derived from continuum theories, the water/vapor interface was thought to be free of ions. [144] Recent investigations show the contrary, in particular large and soft (polarizable) ions show a propensity to accumulate at the water/vapor interface. [140] Small and hard (less polarizable) ions on the other hand stay within the bulk solution. Thus proper treatment of polarization effects is of paramount importance to capture these differences.

In the realm of force-field based methods several options to explicitly account for polarization effects exist. For a comparative review see, e.g., ref 145. Most of them are based on linear response to the field of the surrounding molecules and the corresponding response of the surrounding molecules to this induced change. Hence, this leads to self-consistent procedures that significantly increase the computational time and can in principle not just be added on top of existing models. Existing, non-polarizable models often effectively include polarization effects due to their parametrization with respect to experimental data.

Proper treatment of electronic polarization is included in AIMD simulations, from which nowadays only the ones using DFT for force calculations are affordable. As a showcase for proper treatment of polarization in the context of AIMD simulations, we chose the surface- vs. bulk-solvation of the hydrated electron. The hydrated electron can be seen as "poster-child" for polarizable ions due to the absence of an associated nucleus. Similarly to the two preceeding sections the almost non-existent differences in the structure and energetics of an excess electron in bulk water vs. at the water surface were detailed. As the hydrated electron keeps its first solvation shell when solvated at the water/vapor interface the differences between bulk- and surface-solvation are negligible. The structural and energetical similarities between bulk- and surface-solvation led to the conclusion that no, or only little, energetic preference with respect to either of those should be observed.

3.6 Optical spectroscopy of the bulk and interfacial hydrated electron from ab initio calculations

The optical absorption spectrum of the hydrated electron is an important experimental observable and serves both for general detection and time-dependent monitoring. In an effort to further validate our methodology and strengthen our argument of the minimal differences between bulk and surface solvation of a hydrated electron, the optical absorption spectrum along the trajectories of the bulk- and surface-solvated electron, presented in secs. 3.3 and 3.4, were carried out. [146] This allowed us to obtain spectra appropriate to the thermal equilibrium and corresponding line-broadening. Previously, spectra of bulk-hydrated electrons were calculated either directly from one-electron pseudopotentials or with TDDFT along trajectories obtained from one-electron pseudopotential calculations [44] and to the best of our knowledge never for an excess electron located at the water/vapor interface.

Benchmark calculations are provided for the small cluster $(H_2O)_4^-$ (see sec. 3.2) in a non-equilibrium continuum solvent, for five isolated, distinct $(H_2O)_6^-$ clusters, and for structures from the bulk-hydrated electron presented in sec. 3.3 with a QM region reduced to the first solvent shell (i.e., four QM water molecules and 1020 MM water molecules). Summarizing the results of the benchmarking, excitation energies are converged within tenths of eV for the investigated systems with dual-ζ basis sets with polarization functions on all atoms and diffuse functions on the oxygen atoms. Hybrid density functionals, in particular their long-range corrected versions, are needed for excitation energies that compare well with equation-of-motion coupled cluster calculations with singles and doubles (EOM-CCSD).

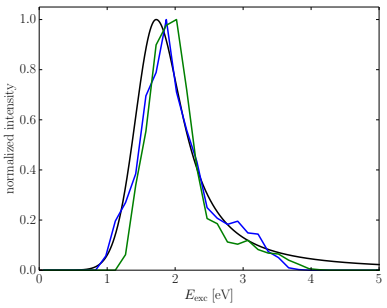

Figure 3.7: Optical absorption spectra of the hydrated electron at 300 K from experiment (black) and from calculations on structures of bulk- (blue) and surface-hydrated (green) electron.

All employed hybrid functionals perform well for the small benchmark systems. The situation is more complicated when turning to production TDDFT calculations on bulk- and surface-hydrated electron with QM subsystems of simi-

lar size as in the original molecular dynamics simulations. For the bulk-hydrated electron the B3LYP density functional underestimates the peak of the optical absorption spectrum, but has a width comparable to the experimental spectrum. Also, calculations with the B3LYP density functional show artificial transfer of spin density in the excited state beyond the QM/MM boundary. This can be seen by calculating the amount of the excited state spin density located beyond the instantaneous liquid interface as generated by the molecules in the MM subsystem (i.e., providing a representation of the QM/MM interface). About 40 % of the excited state spin density are contained within the MM region in calculations with B3LYP, while only 20 % in calculations with LRC-BLYP. This charge-transfer and accompanied underestimation of excitation energies is a well known problem for density functionals like BLYP and B3LYP. [83, 109] Long-range corrected hybrid density functionals remove this artifact. Both LRC-BLYP and LRC-μBOP density functionals in their standard parametrization overestimate the maximum of the absorption spectrum by about 1 eV. The default range-separation parameter μ of these functionals was optimized with respect to sets of small molecules and provides the lowest average errors for diverse properties of these systems. [72, 127] μ is system- and especially system-size dependent. To obtain good agreement with the experimental spectrum tuning of this range-separation parameter proofed to be of paramount importance. As explained in sec. 2.2 the tuning is performed with respect to the ionization theorem in DFT, eq. 2.27. For the small QM/MM benchmark systems the optimal range-separation is similar to the default parameter, i.e., the optimized $\mu = 0.30 a_0^{-1}$ and the default $\mu = 0.37 a_0^{-1}$, for the LRC-μBOP functional. The tuning procedure was repeated for the bulk- and surface-hydrated electron. The optimal parameter for the bulk system is $\mu = 0.165 a_0^{-1}$ and for the interfacially hydrated electron $\mu = 0.180 a_0^{-1}$. With these optimized parameters good comparison to the experimental spectrum can be obtained as can be seen from the calculated and experimental optical absorption spectra shown in Fig. 3.7. The computed spectra are histograms of the first 15 excitation energies weighted by their respective oscillator strengths. The differences in the spectra in bulk and at the interface are in the onset of the spectra, which is steeper for the hydrated electron at the water/vapor interface and in the high-frequency tail, which is less pronounced for the surface-hydrated electron. Latter can be due to an insufficient basis set at the water surface. For the calculations in the water bulk, space is equally well filled with basis functions. At the interface, not as many basis functions penetrate into the vapor phase which may lead to artifacts in the more diffuse excited states.

Radial profiles of the first three excited states in bulk water and at the water surface are shown in Fig. 3.8. Degeneracies in the first three excited states as for the small model system $(H_2O)_4^-$ (D_{2d} symmetry with two degenerate excited states) are lifted due to the finite temperature in the molecular dynamics simulations. Both for bulk- and surface-hydrated electron, the first three excited state spin densities are all of comparable extent, amongst each other as well as compared between surface and bulk. The excited state spin densities are slightly more diffuse at the surface. Dissecting the first three excited state spin densities at the water surface according to sec. 2.6.2 shows that upon excitation about 25 % of the spin densities protrudes into the vapor phase. Only minor parts are left in the original cavity (≈ 5 %), the amount of spin density on water is comparable (≈ 30 %) and the diffuse/interstitial part gains about 10 % compared to the ground state and thus totals to about 40%. For the next two higher lying excited states at the water surface, the average contribution of the spin density in the vapor phase is 5 % less than for the first three excited states. This suggest that artifacts due to insufficient basis sets may not be too pronounced for the first few excited states, but become important only for the very diffuse, high-lying states.

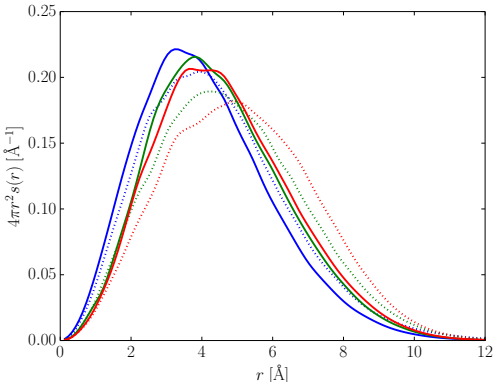

Figure 3.8: Averaged radial profiles of spin density in the first three excited states for the bulk- (solid lines) and surface-hydrated (dotted lines) electron. The origin is set to the center of the respective excited-state spin density.

In summary, when benchmarked properly, TDDFT calculations on structures of the hydrated electron obtained from AIMD simulations compare well to experimental data. The optical absorption spectrum is strikingly similar between a hydrated electron in bulk water and at the water/vapor interface.

3.7 Direct observation of the collapse of the delocalized excess electron in water

When water is ionized an initially delocalized electron is observed which gradually shrinks in size to form the hydrated electron. [9] During the localization not only the size, but also the optical absorption of the excess electron changes dramatically. The localization after electron attachment can thus be monitored in different frequency regimes. Starting from a delocalized and weakly bound electron absorbing at low frequencies in the radio frequency range, localization of the excess electron leads to the hydrated electron, absorbing in the near-IR/VIS region. Here [147], we caught the electron in the initial stages after water ionization. Experimentally, this is achieved with pump-probe spectroscopy on a time-scale of a few ps, where relaxation of the excess electron is primarily due to solvent relaxation in the ground state. The lifetime of an initially photo-excited electron was recently observed to be ≈75 fs. [32] In the experimental part of the present work [1] different photon energies were used for water ionization and the probe frequency was at 1.5 THz. Computationally, the attachment of an excess electron to bulk water is probed for seven trajectories similar to those used for the preparation of the bulk- and surface-hydrated electron in secs. 3.3 and 3.4. A single excess electron was vertically attached to geometries from neat water simulations and the subsequent ground-state dynamics were recorded. TDDFT calculations were performed along these "localization" trajectories to obtain the time-dependent spectra. The average time-evolution of the radius of gyration r_g and the corresponding average first excitation energy E_{exc} are shown in Fig. 3.9. The excess electron localizes on average within 1-2 ps to form the bulk-hydrated electron which is in good comparison to previous exper-

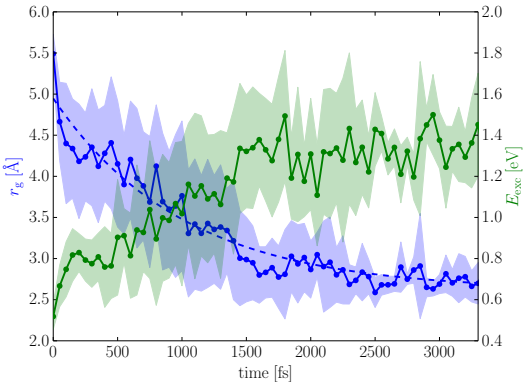

Figure 3.9: Average radius of gyration r_g as a function of time (solid blue), from seven independent molecular dynamics simulations. Exponential fit with time constant $\tau = 1$ ps (dashed blue). Average first excitation energy E_{exc} along these trajectories in green. Standard deviation of the datasets is indicated by shaded areas.

[1] Experiments were carried out by the group of Peter Hamm at the University of Zürich.

iments. [9] As the excess electron shrinks in size the first excitation energy rises until both r_g and optical absorption correspond to that of a hydrated electron in thermal equilibrium (for comparison see also spectra in Fig. 3.7 in sec. 3.6). In these simulations the r_g of the excess electron is limited by the size of the QM region in the QM/MM simulations. The range of sizes was extended by vertically attaching an excess electron to neat water systems with larger QM subsystems. An excess electron was attached along trajectories of systems with 64 QM and 960 MM water molecules and 256 QM and 3886 MM water molecules, but only the state of the excess electron at $t = 0$ was analyzed. The first excitation energy after vertical electron attachment was estimated for these system from their HOMO/LUMO gap. [1] Artifacts due to spurious charge-transfer excitations are not as pronounced for a delocalized excess electron in neat water as for an equilibrated hydrated electron. For comparison of excited state spin densities with different density functionals see Appx. A. Excitation energies E_{exc} and radii of gyration r_g from all simulations are plotted as correlated distributions in Fig. 3.10. An anti-correlation similar to that observed between r_g and VDE is present for the first excitation energy and radius of gyration. Namely, the larger the excess electron is, the smaller is its first excitation energy. This dependence has been observed also in anionic water clusters. [23] The functional form of this dependence is the same as for the correlation between the first excitation energy of particle in a box and its radius of gyration (shown in green in Fig. 3.10 and derivation given in Appx. B). [2] The data from our simulations can be fitted well to this functional form, i.e., a/r^2, which is also shown in Fig. 3.10 (red line). The good correspondence between the particle in a box model and our ab initio data is encouraging in that the fit is meaningful and can be used further on. The fit can be employed to extrapolate to excitation energies used to detect the excess electron in the THz experiments. According to this extrapolation the excess electron has $r_g \approx 40$ Å at the peak intensity of the THz beam (at $E_{exc} = 1.5$ THz). Via the extrapolation we can provide estimates for the size of the excess electron over a wide range of frequencies during the process of localization.

[1] The HOMO/LUMO gap was scaled down according to a factor obtained from comparison to TDDFT calculations in smaller systems.

[2] Data from the particle-in-a-box model was not included in the original publication.

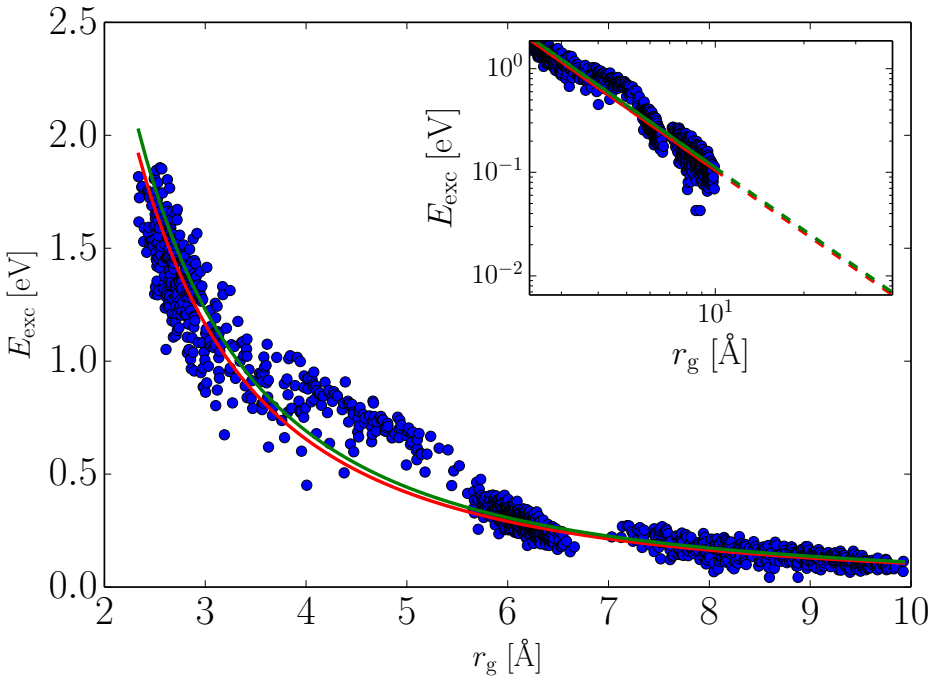

Figure 3.10: Correlated distributions of first excitation energy E_{exc} and radius of gyration r_{g} (blue dots). Fit of the this data to a/r^2 with $a = 10.5$ eVÅ^2 (red line) and the analytical relationship for a particle in a box (green line) are also shown. The inset depicts the same data on a double-logarithmic scale and extrapolation of both particle in a box and fitted relationship shown as dashed lines (same color-coding as in large plot).

Chapter 4

Tying up loose ends

This last chapter gives information on currently unfinished and ongoing work and addresses some problematic issues of the work presented in chap. 3. We start with a discussion on the direct comparison of vertical detachment energies of a bulk- and surface-hydrated electron and corrections to their absolute values in sec. 4.1. Section 4.2 gives an overview of current work related to the calculation of absolute hydration free energies of a bulk-hydrated electron and differences between bulk- and surface-hydration. Section. 4.3 illustrates re-parametrization of the self-interaction correction to remedy artifacts observed in ab initio molecular dynamics simulations.

4.1 Effect of boundary conditions and finite concentration on bulk vertical detachment energy

The direct comparison of structure and energetics of an excess electron solvated in bulk water (sec. 3.3) and at the water/vapor interface (sec. 3.4) is hampered by the different boundary conditions used in these simulations. Simulations of a bulk-hydrated electron were carried out for 3D-periodic systems with no interface while simulations of a surface-hydrated electron were done in periodic systems with elongated lateral dimensions to provide a water/vapor interface. This has an effect both on the vertical detachment energy and on the normalization of the radial distribution functions. Two additional QM/MM molecular dynamics simulations were conducted with consistent boundary conditions. One with an electron in the bulk and one at the surface of a water slab geometry. Unit cells were of the same size in both cases (cell dimensions: 31.4 Å, 31.4 Å, and 100.0 Å). The systems consisted again of 1024 water molecules, from which 32 were treated with the QM

and 992 with the MM methodology. Results after equilibration were collected in short runs of 2.5 ps length. Fig. 4.1 shows the radial distribution functions of oxygen atoms around the center of the excess electron both in bulk water (blue) and at the water/vapor interface (green). Even for the short simulation time, these RDFs closely resemble those obtained from our production simulations of a bulk- and surface-hydrated electron with a length of about 10 ps. The direct comparison illustrates how close to each other the solvation structure are in the two hydration environments. Four water molecules comprise the first solvent shell in both cases and only at larger distances from the excess electron the asymmetry of the water/vapor interface leads to significant differences in the RDFs.

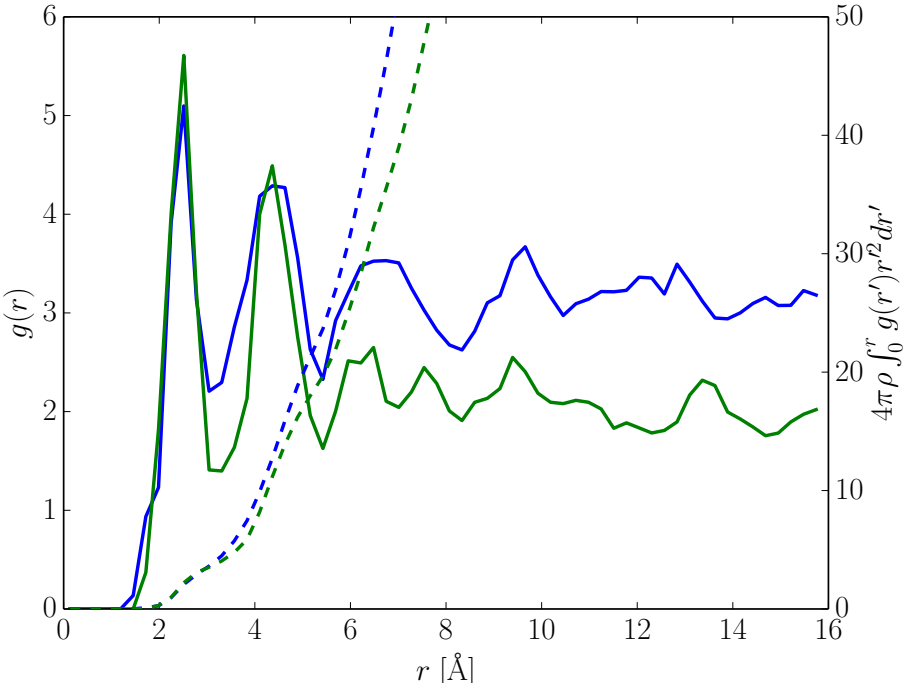

Figure 4.1: Radial distribution functions $g(r)$ of oxygen atoms around center of the spin density $\mathbf{r}_c$ (solid lines) of an excess electron solvated in bulk water (blue) and at the water/vapor interface (green). Running coordination numbers ($4\pi\rho\int_0^r g(r')r'^2dr'$) are shown as dashed lines in respective color coding. ρ is the number density of water molecules in the simulations.

The consistent boundary conditions now allow for a direct comparison between vertical detachment energies of an excess electron at the water surface and in bulk water. Furthermore, corrections to the VDE that account for effects of finite concentration can be introduced and compared. In published articles VDEs were calculated as the difference between periodic neutral and periodic anionic system, i.e., the difference in potential energies upon removal of an effectively infinite number of electrons from the system. Two options are available to rem-

Table 4.1: Differences in vertical detachment energies obtained from "finite concentration" and "infinite dilution" corrections as introduced in the text. All energy differencs in eV. The corrections are given as differences of corrected and uncorrected VDE. For the periodic inifinte dilution correction, differences are not uniformly positive or negative and corresponding percentages of structures are indicated.

correction	bulk	water/vapor interface
non-periodic infinite dilution	90 %: 0.32 10 % -0.11	80 %: 0.19 20 % -0.09
periodic infinite dilution	-0.06	-0.05
finite concentration	-0.07	-0.06

edy resulting artifacts. First, one could run molecular dynamics simulations of a non-periodic QM system in a periodic MM system (i.e., "non-periodic infinite dilution"). As the systems investigated here carry a net charge, this will likely lead to other artifacts. Trajectories of the fully periodic QM/MM system were hence only resampled ignoring the periodicity of both anionic and neutral QM subsystem. Second, a correction can be added taking into account the periodic nature of the system. The QM/MM framework as implemented in CP2K is well suited for this and we implemented a modification to the electrostatic coupling of periodic QM subsystems. As explained in sec. 2.5.3, in a general QM/MM calculation the QM charge density is first decoupled from its periodic images which have the periodicity of the QM subsystem and then re-coupled with the periodicity of the full QM/MM system. The re-coupling is performed using the electrostatic potential of a model charge density that reproduces the multipole moments of the original charge density of the QM subsystem. In principle any model charge density can be included in this routine. If the model charge density for re-coupling of the anionic and neutral system comes from a calculation including the excess electron, the resulting VDE corresponds to removing one electron from the system. Similarly, if the QM charge densities are re-coupled to the model charge density of the neutral system, we obtain a periodic version of the "infinite dilution" correction. Again, trajectories obtained from the fully periodic simulations were resampled, now re-coupling the charge density of the QM subsystem to either the model charge density obtained for the QM subsystem containing the excess charge (referred to as "finite concentration") or to the model charge density of the neutral system ("periodic infinite dilution").

The resulting corrections to the VDEs are collected in Table 4.1. The non-periodic infinite dilution leads to a non-uniform trend in the difference in VDE. Resulting VDEs are higher than uncorrected ones by 0.2-0.3 eV for 80-90 % of the resampled structures. For 10-20 % of the structures corrected VDEs are

about 0.1 eV lower. This already points to artifacts in the calculations due to the neglect of periodicity of the QM subsystem. Both periodic infinite dilution and finite concentration correction lead to lower VDEs by about 0.1 eV compared to uncorrected ones. The former increases the energy of the anionic system and the latter decreases the energy of the neutral system, while energies of neutral and anionic system stay the same, respectively. This is somewhat counterintuitive as one could expect lowering of the energy of the anionic system for the periodic infinite dilution due to missing repulsion between excess electron and its periodic images. The situation is complicated by the homogeneous, neutralizing background charge in the anionic system. The effect on the energies has not yet been accounted for in our correction scheme. Nevertheless, from our initial correction scheme it can be seen that effects on the VDEs are small at the unit cell sizes employed in the QM/MM calculations.

Figure 4.2 shows the correlated distributions of r_g and VDE including the finite concentration correction, again for the excess charge in bulk water (blue) and at the water vapor interface (green). The consistent boundary conditions in both simulations lead to a close match in distributions of VDE for both bulk- and surface-hydrated electron. The average VDE for bulk- and surface-hydrated electron are 3.2 and 3.4 eV, respectively. Further sampling is required to obtain fully converged distributions of VDE and r_g. In particular, the tail towards lower VDEs and higher r_g is more pronounced in our production simulations of a surface-hydrated electron in ref. 142. This would lead to a lower average VDE of the surface-hydrated electron and hence to even better agreement between bulk- and surface-hydration of the excess electron upon additional sampling. The direct comparison nevertheless illustrates convincingly how closely energetics match between bulk- and surface-hydration.

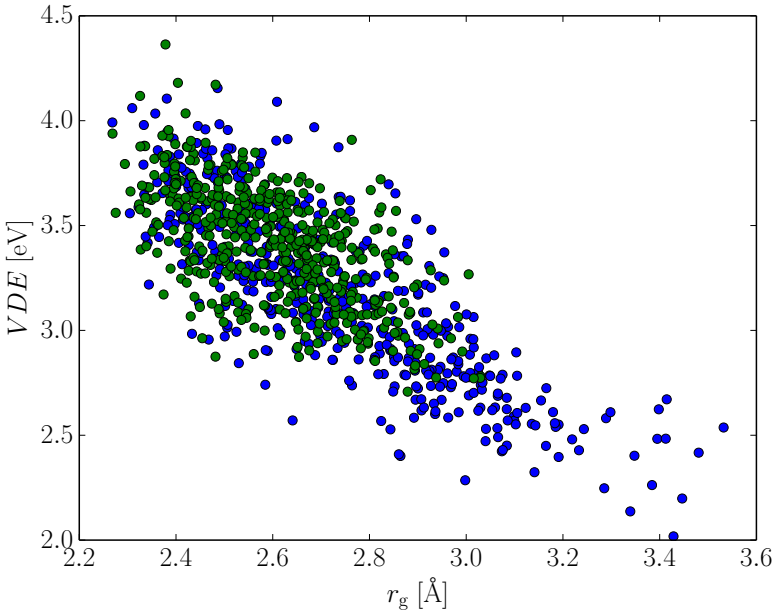

Figure 4.2: Correlated distributions of VDE and r_g of bulk- (blue) and surface-hydrated (green) electron.

4.2 Free energy of hydration of a solvated electron

The similarity in energetics of bulk- and surface-solvation of a hydrated electron serves as strong argument for a negligible difference in hydration free energies in the two environments. Nevertheless, determining the absolute numbers and difference upon moving an electron from bulk water to the water surface is of great interest. The experimental value of the hydration free energy of an excess electron in bulk water was determined by different groups to be −39.4 kcal/mol [148] or −34.6 kcal/mol [149]. The former is based on extrapolations from aqueous monoatomic cations [150] while the latter on extrapolations from cluster ion data [151]. A value of −35.5 kcal/mol was determined from quantum chemistry studies of small, anionic water clusters. [137] The spread in experimental values illustrates the order of errors that range up to a few kcal/mol. These errors are common for both calculations and experimental measurements.

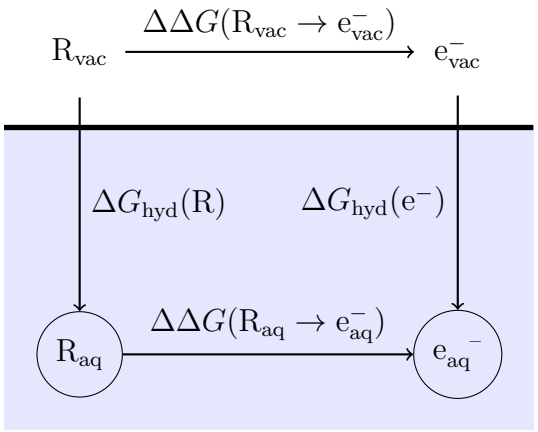

Figure 4.3: Thermodynamic cycle for free energy perturbation calculations. The aqueous phase is indicated by the blue area. R is a reference system. $\Delta G_{\mathrm{hyd}}(\mathrm{R})$ is the hydration free energy of the reference system, while $\Delta G_{\mathrm{hyd}}(\mathrm{e^-})$ the one of an excess electron. $\Delta\Delta G\,(\mathrm{R_s} \rightarrow \mathrm{e_s^-})$ is the difference in free energies of the reference and the excess electron. The subscript s indicates the phase the reference or excess electron are in.

One can construct a thermodynamic cycle as shown in Fig. 4.3 which allows to calculate the absolute free energy of hydration of an excess electron using a reference species R. If the absolute hydration free energy is known for this reference, one can obtain the free energy of hydration of an excess electron. $\Delta\Delta G(\mathrm{R_{aq}} \rightarrow \mathrm{e_{aq}}^-)$ can be calculated with free energy perturbation [152] by alchemically changing R into a hydrated electron. The free energy of hydration of the hydrated electron can then be calculated as $\Delta G_{\mathrm{hyd}}(\mathrm{e_{aq}}^-) = \Delta\Delta G(\mathrm{R_{aq}} \rightarrow \mathrm{e_{aq}}^-) -$

$\Delta\Delta G(\mathrm{R_{vac}} \rightarrow \mathrm{e^-_{vac}}) + \Delta G(\mathrm{R_{aq}})$. The choice of reference system is of particular importance as the perturbation should be small. After perturbation from R, the resulting structures need to be representative of structures sampled by a hydrated electron. Resampling of trajectories from the solvated reference system, with the reference substituted by a single excess electron yields potential energy differences ΔU that are input to the free energy perturbation formula:

$$\Delta\Delta G\left(\mathrm{R} \rightarrow \mathrm{e^-}\right) = -k_\mathrm{B}T \ln \left\langle \exp\left(-\frac{\Delta U}{k_\mathrm{B}T}\right)\right\rangle_\mathrm{R}, \tag{4.1}$$

with the difference in potential energies ΔU defined in our case as:

$$\Delta U = E_\mathrm{pot}\left(\mathrm{e^-_{aq}}\right) - E_\mathrm{pot}\left(\mathrm{R_{aq}}\right). \tag{4.2}$$

In eq. 4.1 k_B is the Boltzmann constant, T is the temperature, and $<>_\mathrm{R}$ represents the ensemble average taken over structures extracted from the equilibrium ensemble of the solvated reference system. These equations hold for calculations with the same methodology for both hydrated reference and hydrated electron. If perturbation is performed from a reference described with a different methodology than the hydrated electron, this change needs to be accounted for as well. This can be done by subtracting the potential energies of the systems without the reference or excess electron from respective potential energies including reference or excess electron. Thus ΔU then corresponds to the difference in the interaction energies of hydrated reference and hydrated electron with the surrounding solvent. The interaction energy of a hydrated electron is the negative of its VDE.

Two reference systems were considered. The first reference system is a fluoride ion in water (AIMD simulations of 95 water molecules and one fluoride ion). [1] 270 structures in a stride of 50 fs along the MD trajectory were taken as input for the free energy perturbation. Structurally, the hydrated electron is somewhat similar to a hydrated fluoride ion. The electron is more diffuse in nature, but the average solvation structure of both ions is comparable. The second reference system is a hypothetical particle in water, called "HYP", which was parametrized to provide water structures that resemble those surrounding a hydrated electron. [2] Force-field molecular dynamics simulations in the NVT ensemble were performed for one HYP in 1024 SPC/E water molecules, after NpT equilibration. The SPC/E geometry was slightly modified to reproduce bond lengths and angles of AIMD simulations of neat water and thus reduce errors in the perturbation. [3] This had a negligible effect on properties of the water

[1] Courtesy of Christopher Mundy.
[2] Parameters for Lennard-Jones 12-6 potential are: $q = 0.6\,\mathrm{e}$, $\sigma = 3.15\,\text{Å}$, $\epsilon = 0.05\,\mathrm{kJ/mol}$
[3] OH bond length of 1.00 Å and HH distance of 1.59 Å.

model like number densities and dielectric constant. 500 structures with a stride of 2 ps were taken as input for the free energy perturbation. Perturbation from both reference systems results in structures that closely resemble the ones of a hydrated electron. Figure 4.4 shows radial distribution functions of oxygen atoms around the hydrated electron from our bulk production simulations [108] and after perturbation to the hydrated electron from both above mentioned reference systems. Radial distribution functions from both references are more structured than that of the hydrated electron (blue). The position of the first peak in the RDF of a bulk-hydrated electron is well reproduced with the HYP model (red), but the number of water molecules in the first solvent shell is slightly higher for the latter structures. Structures after perturbation from the fluoride simulations (green) give a slightly shifted peak position for the first maximum, but better reproduce the coordination numbers in the first solvent shell. The RDF beyond the first solvent shell is better reproduced with the HYP model.

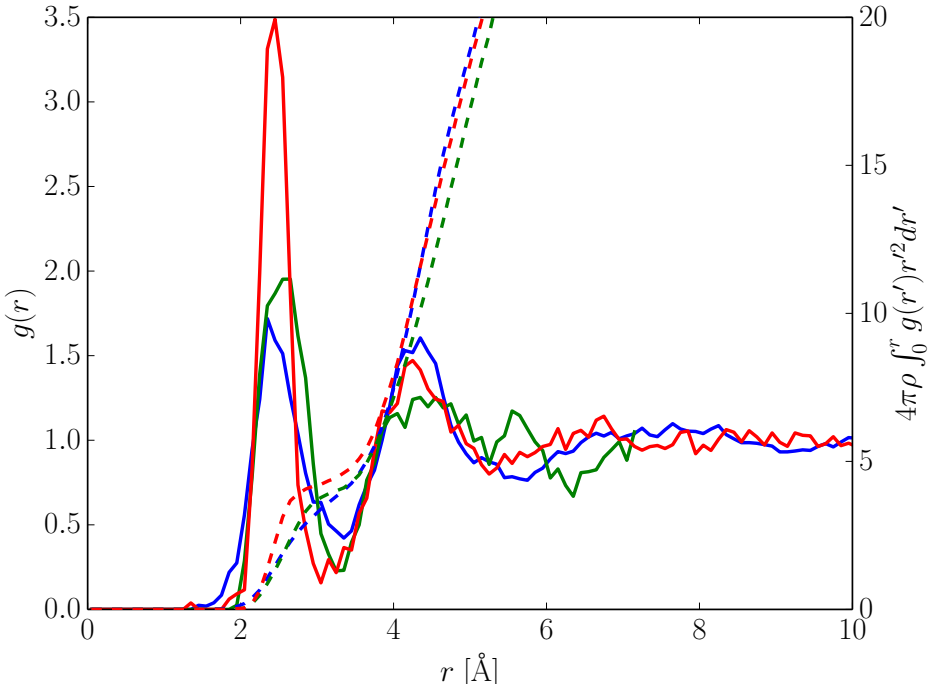

Figure 4.4: Radial distribution functions of oxygen atoms around the center of spin density from bulk-hydrated electron (blue), after perturbation from hydrated fluoride (green), and after perturbation from hydrated hypothetical particle HYP (red). Running coordination numbers ($4\pi\rho\int_0^r g(r')r'^2dr'$) are shown as dashed lines in respective color coding. ρ is the number density of water molecules in the respective simulations.

Free energies of hydration of the solvated electron $\Delta G_{\mathrm{hyd}}(\mathrm{e_{aq}}^-)$ calculated with the above mentioned reference systems are given in Table 4.2. Also included are

Table 4.2: Free energies of hydration of hydrated electron (in kcal/mol) with different references and methods.

from	to	$\Delta G_{\mathrm{hyd}}^{\mathrm{e_{aq}}^-}$
QM/MM e_{aq}^{-} [a]	QM/MM F^- @ e_{aq}^{-} [a]	-33.8
QM/MM e_{aq}^{-} [a]	QM/MM Cl^- @ e_{aq}^{-} [a]	-55.1
QM F^-	QM e_{aq}^{-}	-41.6
MM HYP [b]	QM/MM e_{aq}^{-} [c]	-33.1

[a] 64 QM water molecules and 960 MM water molecules

[b] 1024 MM water molecules

[c] 32 QM water molecules and 992 MM water molecules

perturbations starting from dynamics of a bulk-hydrated electron to fluoride and chloride ion in water (structures taken every 5 fs from bulk QM/MM simulations of e_{aq}^{-}). The chloride and fluoride ions were put at the center of the spin density in these calculations. The value of the hydration free energy of the fluoride and chloride ion were taken from ref. 153. Hydration free energies based on perturbation calculations from a hydrated electron to a chloride ion lead to a too low hydration free energy of -55 kcal/mol of the excess electron. Perturbation to fluoride leads to a hydration free energy of about -34 kcal/mol which is in good agreement with literature values mentioned at the beginning. The chloride ion as a reference system is included mainly for comparison and illustrates the importance of a proper choice for the reference system. Perturbation from AIMD simulations of a hydrated flouride to a hydrated electron yielded a hydration free energy $\Delta G_{\mathrm{hyd}}(e_{aq}^{-})$ of about 42 kcal/mol. This value is about 8 kcal/mol lower than perturbation performed vice versa. Last, but not least, perturbation from the HYP reference system (MM) to a hydrated electron (QM/MM) yielded a hydration free energy of about 33 kcal/mol.

Statistical convergence of the presented values can be estimated from the difference in ΔG values when only half the number of snapshots are included. This difference is on the order of 0.5 kcal/mol for perturbation from hydrated HYP and fluoride. It is larger, about 1 kcal/mol, for perturbation from hydrated electron to fluoride. Structures used for the latter calculations were taken with a smaller stride and are likely more correlated. Free energy perturbation should give the same hydration free energies when performed from a hydrated fluoride ion to electron and vice versa. Nevertheless, it is known that in practice convergence depends on the direction of the perturbation. [154]

Following sources of errors exist in the computations. The free energy perturbation calculation involving QM/MM calculations depends on the convergence

of the interaction energies of hydrated reference and electron with respect to size of QM subsystem. If convergence is the same for both species, then this effect will cancel. This is not the case for the systems considered here. The convergence differs due to the diffuse nature of the hydrated electron compared to a more compact hydrated fluoride (and HYP). Vertical detachment energies (and hence interaction energies) of the hydrated electron are converged within 0.3 to 0.4 eV for QM subsystems consisting of 32 water molecules compared to systems with up to 300 QM water molecules. As the interaction energies between excess electron and surrounding water molecules get smaller in magnitude with larger QM size, the difference to the reference system gets larger. Fully converged VDEs will thus lead to an increase in hydration free energy of the hydrated electron. A counteracting effect is observed for the HYP model. It does not take into account the flexible nature of the water molecules. If it were accounted for, the VDE would increase. Thus, the hydration free energy would decrease. The change in water geometry around a hydrated electron is nevertheless a local effect. This is evident from the red-shift in OH-stretch frequencies observed only for water molecules directly surrounding a hydrated electron. The corresponding power spectra are given in ref. 143. The good agreement with literature values of hydration free energies calculated with the HYP reference is hence to some degree due to fortuitous error cancellation of the two counteracting effects of not fully converged VDEs and the not accounted for local change in water geometry around the HYP model. Both effects will cancel individually when investigating the difference in free energies of a hydrated electron in bulk water and at the water/vapor interface.

The difference in free energies for a bulk- and surface-hydrated electron were calculated with the HYP model. First, the free energy profile along the distance of one HYP from the center of a water slab consisting of 215 water molecules was calculated with umbrella sampling [155] (using 50 windows and 10 ns simulation time each). Second, two free energy perturbation calculations were performed. The reference system was one HYP solvated in a slab geometry of 1024 water molecules (32 QM and 992 MM). In one calculation HYP was located in the middle of the slab of water and in the other about 3 Å from Gibbs' dividing surface. The free energy difference upon moving HYP up to this distance from the interface is about 0.5 kcal/mol. With the latter value the free energy perturbation calculations give a preference for surface solvation of the excess electron by about 0.2 kcal/mol, which is within the error of the calculation. This value is not yet unbiased for the spurious effect of the uniform background charge. [98] Removing the bias will lead to a smaller difference or even inverted tendencies.

Computations are currently being extended also to other reference systems

that avoid the mixture of methods. The small difference in hydration free energy also suggests that a direct sampling approach to the free energy difference would be feasible. Methods to enhance sampling are designed to effectively flatten the free energy landscape and have no direct benefit for an already flat landscape. [1] The remaining problem is the computational cost associated with running these molecular dynamics simulations. Namely, at least 200 water molecules are needed to simultaneously get converged bulk properties in presence of a water surface.

[1] These methods also involve constraints or restraints on the coordinate of interest. This could in principle be achieved with constraints/restraints on occupation numbers, or similar schemes. It would nevertheless involve computationally intense benchmarking.

4.3 Why not full ab initio molecular dynamics?

The original plan of this work was to carry out straightforward ab initio molecular dynamics simulations with pure QM methods of an excess electron solvated in bulk and slab geometries. This failed with regular GGA density functionals. Running direct dynamics led to delocalization of the excess electron over the whole simulation box within picoseconds. Figure 4.5 shows the radius of gyration as function of time for several such simulations. Two simulations were carried out using the BLYP density functional plus SIC($a = 0.3$, $b = 0.2$), one in a 3D periodic bulk system consisting of 96 water molecules (green) and one in a 2D periodic slab geometry of 128 water molecules (cyan). The initial conditions for both systems were prepared from force-field based MD simulations that included either the HYP particle introduced in the previous section (bulk system) or an iodide ion (slab system). These ions were removed for the AIMD simulations and substituted by a single electron. This preparation provides an initial cavity for the excess electron to localize in. Although this initial localization happened in all cases, subsequently the excess electron delocalized over the whole simulation cell. In both simulations a strong increase in radius of gyration of the spin density r_g up to about half the cell lengths is observed. The density in the bulk system corresponds to water density at 300 K but with one water molecule removed and substituted by a single electron. Delocalization of the excess electron in the slab geometry excludes the possibility of a significant influence due to the wrong number density. Also simulations of a bulk-hydrated electron in an NpT ensemble were carried out and yielded a persistently delocalized excess electron (data not shown). The two AIMD simulations of 96 water molecules in bulk and 128 molecules in a slab geometry are short and one could potentially expect a return to a more localized species. Thus we performed simulations of an excess electron vertically attached to a neat water system. The inset in Fig. 4.5 shows the radius of gyration after electron attachment to a 3D-periodic system consisting of 64 water molecules at a density of 1 g/cm^3. The radius of gyration fluctuates around half the cell lengths for over 10 ps and shows no localization of the excess electron.

The delocalization is understood as artifact in the simulations. The delocalized excess electron is different from structures observed with a particular parametrization of a one-electron pseudopotential [38]. In the above described AIMD simulations, the spin density is spread over interstitial space and (what would be) anti-bonding orbitals of water molecules. The center of the spin density [1] shows erratic movement from one water molecule to another, which are not

[1] The center of the periodic spin density in one unit cell is estimated using minimum images

necessarily close to each other. The delocalization artifact was to some extent observed in other publications [36, 37] as exemplified by the short lifetimes of tens of femtoseconds of a localized excess electron in these AIMD simulations. Additionally, the parameter combination of the SIC($a = 0.2$, $b = 0.0$) (red in Fig. 4.5) led to generation of hydrogen. This is also seen as an artifact in the simulations and it is attributed to an overly localized electron with the SIC($a = 0.2$, $b = 0.0$). Although the reaction between an excess electron and neat water is observed in experiment, it happens on a much slower, sub-millisecond time scale. [12]

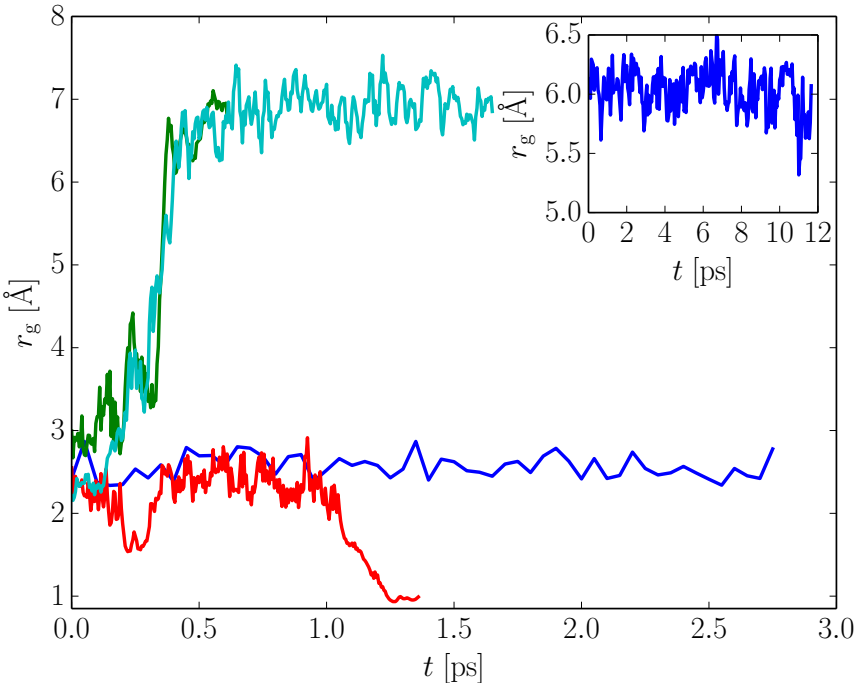

Figure 4.5: Radius of gyration r_g along trajectories of 96 bulk water molecules calculated with PBE0 (blue), BLYP + SIC($a = 0.3$, $b = 0.2$) (green) BLYP + SIC($a = 0.2$, $b = 0.0$) (red) and for an electron in a slab geometry of 128 water molecules (cyan), also with BLYP + SIC($a = 0.3$, $b = 0.2$) methodology. The inset shows the time evolution of r_g for an equilibrated system of 64 water molecules after vertical attachment of one excess electron with BLYP + SIC($a = 0.3$, $b = 0.2$).

The artificial delocalization of the excess electron can be avoided by switching to a density functional which includes to some extent exact Hartree-Fock exchange, which is, however, at a high computational cost. Therefore, another AIMD simulation of 96 water molecules and an excess electron was conducted using the hybrid density functional PBE0 [156]. The simulation was started from

around the highest value of the spin density. Only considering the original unit cell for a delocalized electron leads to the center of the spin density always being close to the center of the unit cell.

the same initial conditions as the previously mentioned bulk simulations of 96 water molecules and one excess electron. PBE0 includes 25 % of exact Hartree-Fock exchange. No delocalization of the excess electron was observed in this simulation in 2.5 ps (blue curve in Fig. 4.5). The average radius of gyration of the spin density in this simulation is about 2.6 Å, i.e., only about 0.2 Å smaller than in our bulk QM/MM simulations. The average amount of spin density in a cavity is 45 %, on water 25 %, and in interstitial space 30 %. The cavity is slightly more pronounced than in the QM/MM simulations in favor of a reduced amount of spin density in interstitial space. The success of this simulation, even on the short time scale, points to a problem related to the self-interaction error in the simulations using BLYP + SIC. The partial inclusion of exact Hartree-Fock exchange is known to reduce the self-interaction error. Thus, we re-examined the parametrization of the self-interaction correction.

In the further discussion we refer to classical electrostatic self- and exchange-correlation energy of a single electron. In reality these do not exist for a single electron and should cancel out in calculations with the exact density functional. In computations they are explicitely calculated and do not cancel out due to the approximate nature of the density functional. Hence, from a purely electrostatic point of view it is favorable for a single electron to delocalize to minimize its associated self-energy. This effect is in general present in all GGA density functionals. The extent to which artifacts are observed depends among other things on the size of the system. The delocalization is enhanced in small periodic simulation cells, compared to larger ones (vide infra). In our QM/MM simulations the electron could in principle delocalize as well over the QM subsystem, but artifacts are reduced due to the large unit cells employed. Brief delocalization of the excess electron occurred occasionally in these simulations, but was always followed by re-localization within tens of femtoseconds.

The SIC was re-parametrized for both bulk and small cluster geometries. The BLYP density functional was used throughout. Optimal parameters for the PBE density functional [157] are similar to those for BLYP. Parametrization of the self-interaction correction was previously done in comparison to reaction profiles in small cluster systems, see sec. 3.1. Another way of parameterizing the SIC is to enforce the IP theorem (eq. 2.27) as in benchmarking done for long-range corrected density functionals in sec. 3.6 and in literature (e.g., ref. 71 and references therein). Figure 4.6 (top) shows the absolute values of sums of vertical detachment energies and eigenvalues of the singly occupied molecular orbital for the cluster $H_3O^+(H_2O)_3e^-$ as shown in Fig. 3.1 in sec. 3.1. The calculations were performed in a periodic cubic box of 16 Å side length. Thus, possible artifacts due to periodic boundary conditions are included. The periodic boundary conditions

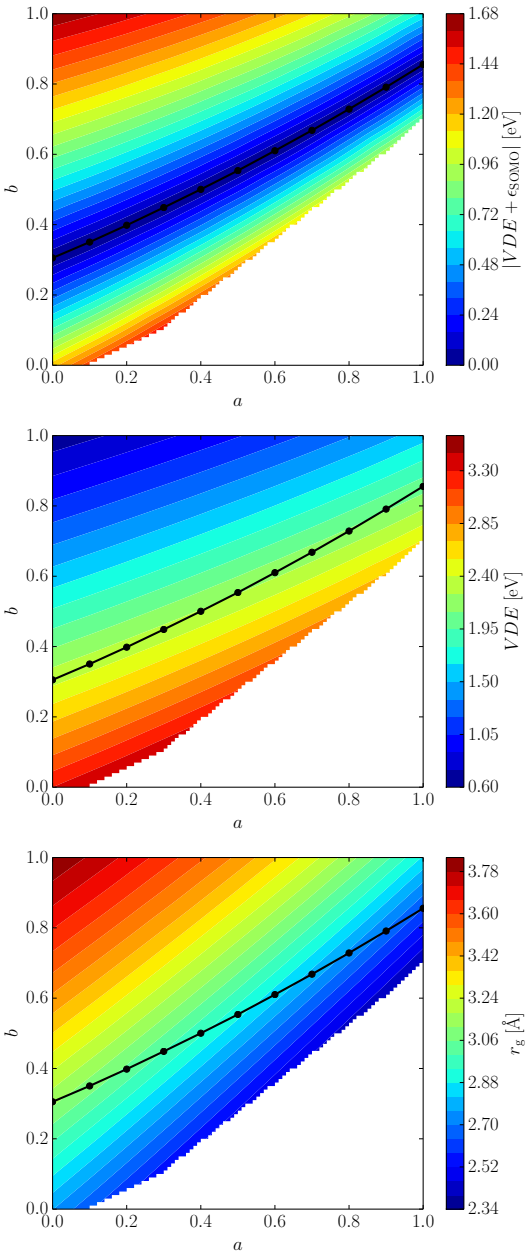

Figure 4.6: Several quantities for $H_3O^+(H_2O)_3e^-$ cluster (see sec. 3.1) calculated with different parameter combinations in self-interaction correction in ref. 68. Top panel shows absolute values of sum of VDE and ϵ_{SOMO}, middle panel the VDE itself, and bottom panel the r_{g} of the spin density. Parameter combinations that lead to compliance with IP theorem in DFT are plotted as black dots in each plot. The empty region is due to non-convergent self-consistent field cycle within 50 iterations (using diagonalization of Fock matrix, started from optimized wavefunction obtained with orbital-transformation in preparatory calculations).

at this cell size lead to lower VDEs (calculated as difference in potential energy of periodic neutral and periodic anionic system) compared to those in isolated clusters. Energies were calculated for combinations of a and b with a stride of 0.1. For each value of the parameter a there is an optimal value of b that leads to compliance with the IP theorem, i.e., $VDE + \epsilon_{\mathrm{SOMO}} = 0$ (given by black dots in Fig. 4.6). Energies of the singly occupied molecular orbital and vertical detachment energy in dependence of b are smooth and can be fitted using cubic splines to facilitate estimation of the optimal parameter combination. For $a = 0.3$ the optimal value of $b = 0.45$. The same parameter combination was obtained in analogous parameter scans for the cluster model $(H_2O)_4^-$ in sec. 3.2. Figure 4.6 also shows the VDE (middle panel) and radii of gyration (bottom panel) for the different parameter combinations. Parameter combinations leading to compliance with the IP theorem are again indicated by black dots. VDEs are similar along the course of optimal parameter combinations for the SIC. In contrast, tendencies within r_g are more skewed with respect to the optimal SIC parameters. Larger artifacts are thus to be expected for the extent of the spin density when deviating from the optimal parameters.

Along the line of optimal parameter combinations an increase in r_g and a decrease in VDE can be seen towards smaller a. Generally, r_g tends to smaller values for larger values of a at constant b and to larger values vice versa. The reverse holds, and to a larger extent, for the VDEs. Hence, relative deviations in VDE and r_g along optimal parameter combinations are similar, nevertheless still larger for r_g. For none of the parameter combinations electrostatic and exchange-correlation energy of the spin density cancel out perfectly (see Fig. C.1 in Appx. C). Deviations from complete cancellation of the latter energies are larger for parameter combinations complying with the IP theorem with small a. These deviations along the path of optimal SIC parameters point to the fact that simulations with different parameter combinations that all comply with the IP theorem need not yield equivalent results. Furthermore, calculations with SIC($a = 0.3$, $b = 0.45$) in unit cells of 10 Å side lengths gave radii of gyration about 10 % larger than in the larger unit cells. Corresponding calculations with SIC($a = 1.0$, $b = 0.86$) gave relative errors of about 25 % in r_g in the smaller unit cells. The r_g in the small unit cells is comparable for both parameterizations. It is significantly smaller for SIC($a = 1.0$, $b = 0.86$) in the larger unit cell compared to SIC($a = 0.3$, $b = 0.45$) (see Fig. 4.6). The finite size of the unit cells thus also affects the delocalization of the excess electron.

A similar self-interaction correction was proposed in the literature that also removes the electrostatic self-energy of the spin density, but substitutes the exchange-correlation energy of the full system by the one for the system without

the unpaired electron. [67] This SIC can also be cast into a parametrized form similar to ref. 68 with parameters a for scaling the removal of electrostatic self-energy and b for the exchange-correlation contribution. At $a = 1.0$ and $b = 1.0$ the parametrization corresponds to its original form in ref. 67. We performed the same parameter-scan as above for this SIC (shown in Fig. C.2 in Appx. C). The parameter combination $a = 1.0$ and $b = 1.0$ is one of those that comply with the IP theorem. Nevertheless, the resulting VDE is artificially low due to the complete neglect of exchange-correlation interaction between the unpaired and all other electrons in the system. The unpaired electron thus effectively behaves as a single electron in the electric field of all other electrons. And for all one-electron systems the parameter combination of SIC($a = 1.0$, $b = 1.0$) gives the exact solution. The VDEs between the two variants of SIC hence also differ by about 2 eV for parameters close to unity. This shows that these parameter combinations are not suited for use with the SIC in ref. 67. The SIC used throughout this work [68] generally includes the exchange-correlation interaction between all electrons and can hence also be used for parameters close to unity as both electrostatic and exchange-correlation interactions between the unpaired and all other electrons are present.

The parametrization may show a significant size dependence similar to the one observed in parametrization of the range-separation parameter in long-range corrected hybrid density functionals. Thus it needs to be repeated for the bulk systems. Parameter scans were performed for five snapshots extracted from the bulk simulation using the PBE0 density functional. Energies were calculated for combinations of a and b with a stride of 0.1 for b, and a set to either 0.3 or 1.0. Figure 4.7 shows the resulting absolute values of sums of vertical detachment energies and eigenvalues of the singly occupied molecular orbital for five individual snapshots (gray) and their average (blue) for $a = 0.3$. The average optimal value of b for the five snapshots is 0.30. The resulting SIC($a = 0.3$, $b = 0.3$) is close to our original parametrization (SIC($a = 0.3$, $b = 0.2$)). Simulations with both parameter combinations led to delocalization of an excess electron in water in the purely QM simulations within less than a picosecond. This is in accord with the artificially large r_g observed in the small cluster system for optimized parameter combinations with small a. It suggests that, as in the small cluster, not all parameterizations of the SIC with respect to the IP theorem lead to the correct cancellation of electrostatic and exchange-correlation energy of a single electron. On the other hand, setting $a = 1.0$ guarantees the complete removal of the electrostatic self-energy of the single electron. For BLYP the optimal parameter combination then is SIC($a = 1.0$, $b = 0.74$). [1] Figure 4.8 shows the

[1] The tuning was repeated for the same snapshots with PBE density functional. The average

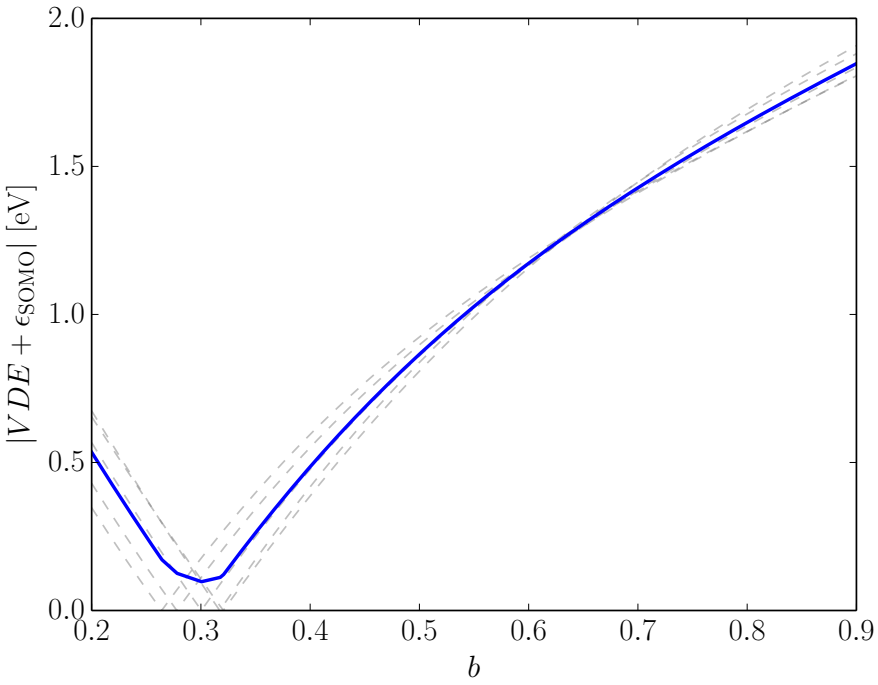

Figure 4.7: Plot of absolute values of sum of vertical detachment energy and eigenvalue of singly occupied molecular orbital ϵ_{SOMO} as a function of SIC parameter b at a constant value of $a = 0.3$. Curves for five individual snapshots shown as gray dashed lines and their average as blue line.

difference in spin densities calculated with optimized parameter combinations I: SIC($a = 0.3$, $b = 0.3$) and II: SIC($a = 1.0$, $b = 0.74$) for one particular snapshot. The red isosurface encompasses regions where the spin density in I attains higher values than in II and vice versa for the blue isosurface. The calculations with SIC($a = 1.0$, $b = 0.74$) yields a much more compact electron with higher values of the spin density inside the cavity of the hydrated electron. In contrast, the density is much more diffuse with SIC($a = 0.3$, $b = 0.3$). The latter parametrization shows significant charge transfer to water molecules in the second solvent shell around the hydrated electron. The radius of gyration of the spin density is 4.0 Å for SIC($a = 0.3$, $b = 0.3$) and 2.6 Å for SIC($a = 1.0$, $b = 0.74$). The delocalization is thus still favored for SIC($a = 0.3$, $b = 0.3$) and points again to a residual influence of the not completely canceled classical self-energy of the spin density. We are currently in the progress of generating trajectories of a bulk-hydrated electron with the newly parametrized SIC($a = 1.0$, $b = 0.74$). Further simulations with SIC($a = 1.0$, $b = 0.7$) and SIC($a = 1.0$, $b = 0.8$) are being produced to check sensitivity of results with respect to b parameter. Up to now all of these simulations produced trajectories with excess electrons localized within a cavity for at least 3 ps, similar to our bulk QM/MM calculations. They are currently being extended.

In summary, two different ways exist to avoid the delocalization artifact. First, large unit cells as in the QM/MM simulations lead to reduced finite-size effects. Second, careful re-parametrization of the SIC that avoids spurious effects due to the electrostatic self-repulsion lead to stable simulations of a bulk-hydrated electron, even in comparably small unit cells. It should also be noted that a minor residual effect of the self-interaction error might still be present in our QM/MM simulations due to the use of SIC with small values of a leading to more extended spin densities. This explains the slightly larger radii of gyration in the QM/MM simulations compared to experimental values and values obtained from AIMD simulations using the PBE0 density functional. Nevertheless, the qualitative structure of the spin density in the QM/MM simulations compares well to the simulations with the PBE0 density functional.

optimal parameter combination for these is SIC($a = 1.0$, $b = 0.72$).

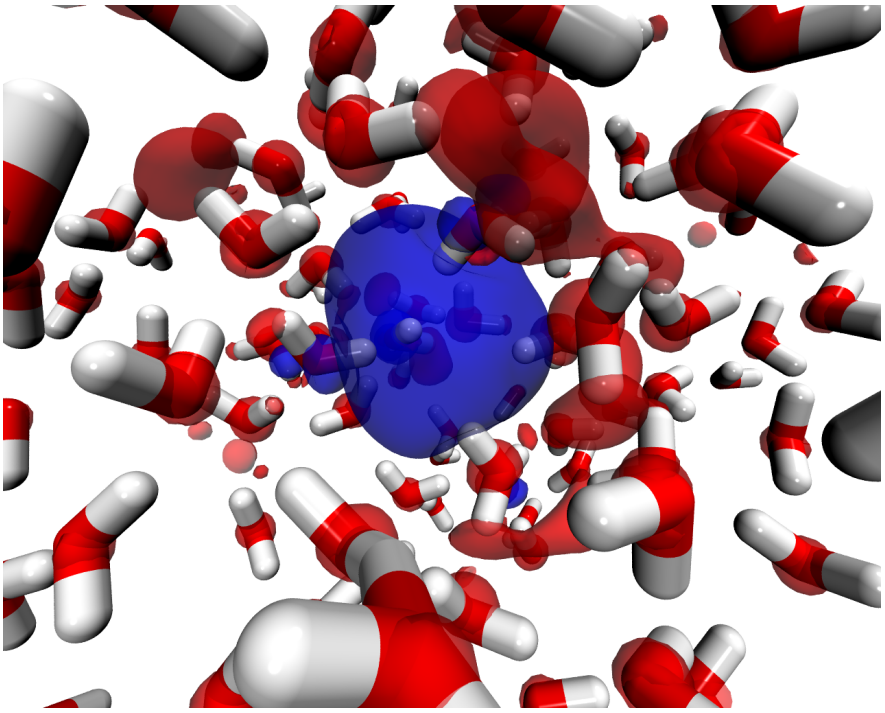

Figure 4.8: Difference density between two SIC parametrizations calculated for a snapshot from AIMD simulation with PBE0 DF. Isosurfaces show difference in spin density re-calculated with two SIC parameter sets I: SIC($a = 0.3$, $b = 0.3$) and II: SIC($a = 1.0$, $b = 0.74$). The difference density $\Delta m\,(\mathbf{r})$ is calculated as $m^{\mathrm{I}}\,(\mathbf{r}) - m^{\mathrm{II}}\,(\mathbf{r})$. Red isosurface is at a value of 0.0005 a.u. and blue isosurface at -0.0005 a.u.

Chapter 5

Conclusions and outlook

The presented work provides a detailed view on the structure, dynamics, and reactivity of an excess electron in water, i.e., the hydrated electron using ab initio methods. Calculations on small clusters allowed us to benchmark the DFT methodology which could then be transferred to model equilibrium properties of an excess electron in bulk water and at the water/vapor interface. Furthermore, dynamics after vertical electron attachment to neat water could be modeled with the same DFT methodology in bulk water. The small cluster systems themselves also yielded results relevant for the reactivity of a hydrated electron.

An excess electron in small water clusters already resembles to some extent a bulk-hydrated electron. Such systems can thus also be used to investigate the reactivity of the hydrated electron. By successive solvation of an H_3O radical a solvent-separated pair of hydrated proton and electron can be obtained. The main features of the recombination reaction between the latter two can be recovered in this small cluster system as both electron and proton are already well solvated. The reaction is thus not barrierless, because of the penalty associated with desolvating the reaction partners (similarly observed in medium-sized water cluster anions [134]).

Cluster models of pure water and an excess electron were obtained by embedding structures in a continuum solvent. Stable structures can be obtained for both a four- and six-fold coordination of an excess electron by water molecules. Nevertheless, extending the cluster sizes led to re-arrangement to clusters that support a four-fold coordination of the excess electron. This is in good correspondence to most simulations with one-electron pseudopotentials [33] and actually corresponds well to one of the earliest suggestions for the structure of a hydrated electron [39]. Properties like vertical detachment energy and main features of the optical absorption spectrum are in good comparison to experimental data.

The hydrated electron is a diffuse species and explicit account of solvent shells beyond the first one is needed to completely describe its solvation. We mod-

eled the hydrated electron using QM/MM molecular dynamics simulations. In the water bulk this elusive species can be decomposed into three spatially non-overlapping parts. First and foremost, about 40 % of the hydrated electron is localized in a cavity-like structure surrounded by water molecules with OH bonds polarized towards the center of this cavity. Albeit being the largest contribution overall, more than half of the electron spreads elsewhere. Namely, part of it overlaps with water molecules (25 %) and the rest is found between the water molecules (35 %). Due to their comparable magnitudes all these contributions are equally important and can only be faithfully recovered using ab initio methods that treat not only the excess electron, but also the surrounding water molecules quantum mechanically. The picture of the hydrated electron we obtained can be seen as a happy medium between the traditional view of a hydrated electron mainly solvated in a cavity [33] and a recent model of a largely delocalized hydrated electron [38].

Upon moving the electron to the water surface only little change is observed in comparison to bulk solvation. The hydrated electron keeps its first solvent shell and thus contributions from parts of the electron in cavity, on water, and in interstitial space stay on average similar to those for bulk solvation. Only about 10 % of the electron leaks beyond the water/vapor interface. This similarity in solvation structures leads to comparable vertical detachment energies for bulk- and surface-hydrated electron. The VDEs show no correlation to the position of the hydrated electron with respect to the interface. Thus it is to be expected that preferences towards solvation either in bulk water or at the water surface are minimal. Initial investigations indeed show that the difference in hydration free energies between bulk- and surface-solvation is about 0 kcal/mol. We are currently in the process of extending these calculations. Overall, these findings do not support the existence of a stable, weakly hydrated excess electron at the surface with low binding energies, that was suggested in ref. 28.

Monitoring dynamics after the attachment of an excess electron to neat water allowed us to model processes following photoionization for the first time in bulk solution using ab initio methods. The electron attachment is followed by a fast localization of the spin density to a cavity within 1-2 ps and hence the formation of the hydrated electron. Due to reasons of computational expense, modeling the process in the regime of our experimental colleagues (i.e., THz absorption and several-nm-sized excess electrons) is not possible. Nevertheless, employing an analogy to a particle in a box allows for extrapolations over a wide frequency range of the absorption spectrum and provides reasonable estimates for the size of the excess electron during the localization process. These extrapolations yield an estimate for r_g of about 40 Å for an excess electron absorbing at 1.5 THz.

Validity of the present conclusions on a hydrated electron in equilibrium and its dynamics after vertical attachment to water is supported by the fact that the simulations reproduce several experimental observables well. Quantities like vertical detachment energy, radius of gyration, and optical absorption spectrum of the hydrated electron are all in accord with experimental data. Finite concentration corrections to the VDE have been introduced. As it turns out, these corrections are minimal for the simulation cell sizes employed. The radii of gyration in our QM/MM simulations tend to slightly larger values compared to the experiment. Our latest results concerning benchmarking of the self-interaction correction indicate that some residual, albeit small, size and methodological effects are present in both VDE and radius of gyration. The new parameterizations suggest a slightly smaller and more strongly bound excess electron, which is in even better correspondence to the experiment.

The calculated optical absorption spectrum is in quantitative agreement with the experimental one. Extensive benchmarking was carried out to obtain the former and the good agreement can only be achieved with tuned, range-separated hybrid density functionals. This adjustment of the range-separation parameter μ to comply with the IP theorem in DFT is of paramount importance. In our large systems, the optimal value of μ is only about half of its default value. The tuning procedure has proven to be a reliable benchmark for our large systems, for which comparison to calculations with highly correlated quantum chemistry methods are hardly possible due to their prohibitive computational expense.

Similar re-parametrization of the self-interaction correction [68] with respect to the IP theorem, while enforcing the complete removal of the spurious electrostatic self-energy of the spin density, looks also very promising. Further AIMD simulations are necessary to investigate the long-term stability of corresponding simulations of an excess electron in water. Although in a different sense, long-term stability is also an issue in QM/MM simulations. In these simulations it can happen that the excess electron diffuses to the boundary between QM and MM regions on a time-scale of tens of picoseconds which then leads to artifacts. However, such long simulation times are needed, e.g., to determine the difference in free energy of hydration of an excess electron in bulk water and at the water/vapor interface by direct molecular dynamics simulations.

The new parametrization of the SIC could be useful to investigate reactions of a bulk-hydrated electron with various quenchers. Two interesting cases are reactions of a hydrated electron with nitrous oxide (N_2O) and hydroxyl radical ($\cdot OH$). Modeling the reaction of an excess electron with N_2O was already attempted in this work. The reaction cannot be described fully in small cluster systems, but only the cleavage of ON-bond after electron attachment to N_2O. Hydration of

both N_2O and the excess electron must be accounted for simultaneously. N_2O is not a strongly hydrated species and larger systems are thus required to separate and solvate both nitrous oxide and hydrated electron. The reaction of the latter with ·OH is more complicated from a methodological point of view as it proceeds from a singlet bi-radical (·OH and e_{aq}^-) to a closed-shell species (OH^-). Currently, the SIC employed throughout this work is not suitable for this case. Nevertheless, a self-interaction correction is needed for proper description of both ·OH [68] and e_{aq}^-. One possiblity would be to use a scaled, orbital-dependent SIC (i.e., a combination of refs. 66 and 68) that only acts on the two highest-lying electrons or, the much more costly alternative, hybrid density functionals. Further investigations on the reactivity of the hydrated electron are needed and can help to stimulate methodological development as these problems go beyond capabilities of affordable, present-day density functional theory.

In summary, the results in this thesis are a showcase example of, first, the necessity of using ab initio methods in a particular context, here the hydrated electron, and second, usefulness of these methods in providing detailed molecular information that is not easily accessible from experiment or more approximate computational methods.

Appendix A

Comparison of excited state spin density after vertical electron attachment

Two figures are included in this appendix. Both, Fig. A.1 and A.2, show excited-state spin densities after vertical attachment of an excess electron to neat water. The origin of the radial profiles is set to the center of the respective ground-state spin density. The time-dependent density functional theory calculations were performed with three different density functionals, BLYP, B3LYP and LRC-BLYP. Figure A.1 shows the excited state spin density 0 fs after attachment of the excess electron and Fig. A.2 after 500 fs. The comparison illustrates that the different density functionals provide comparable excited state spin densities for a delocalized excess electron at 0 fs. Artificial charge transfer of the excited state spin density beyond the QM/MM boundary is observed for both BLYP and B3LYP density functionals as the ground state excess electron shrinks in size after its vertical attachment to water. The excited state spin densities are much more extended when calculated with BLYP and B3LYP than with the LRC-BLYP density functional 500 fs and later on after vertical attachment of an excess electron. Thus, less artifacts are to be expected for calculations with the computationally cheaper BLYP and B3LYP density functionals immediately after vertical excess electron attachment.

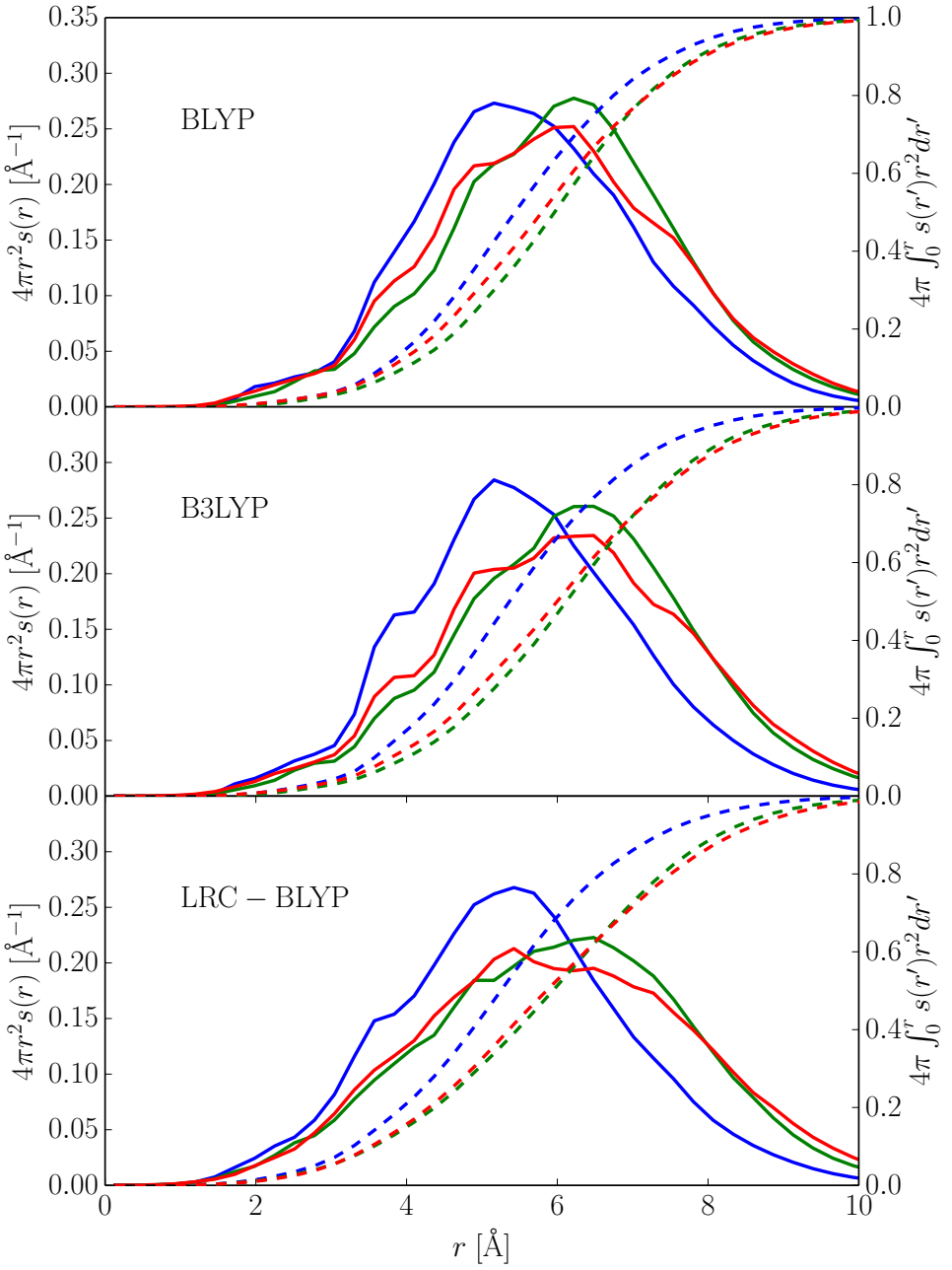

Figure A.1: Radial profiles of the first three excited-state spin densities with respect to the center of the ground-state spin density 0 fs after vertical excess electron attachment (solid lines). The cumulative integrals of the radial profiles are shown as dashed lines. The excited state spin densities were calculated with different density functionals, BLYP (top), B3LYP (middle) and LRC-BLYP (bottom).

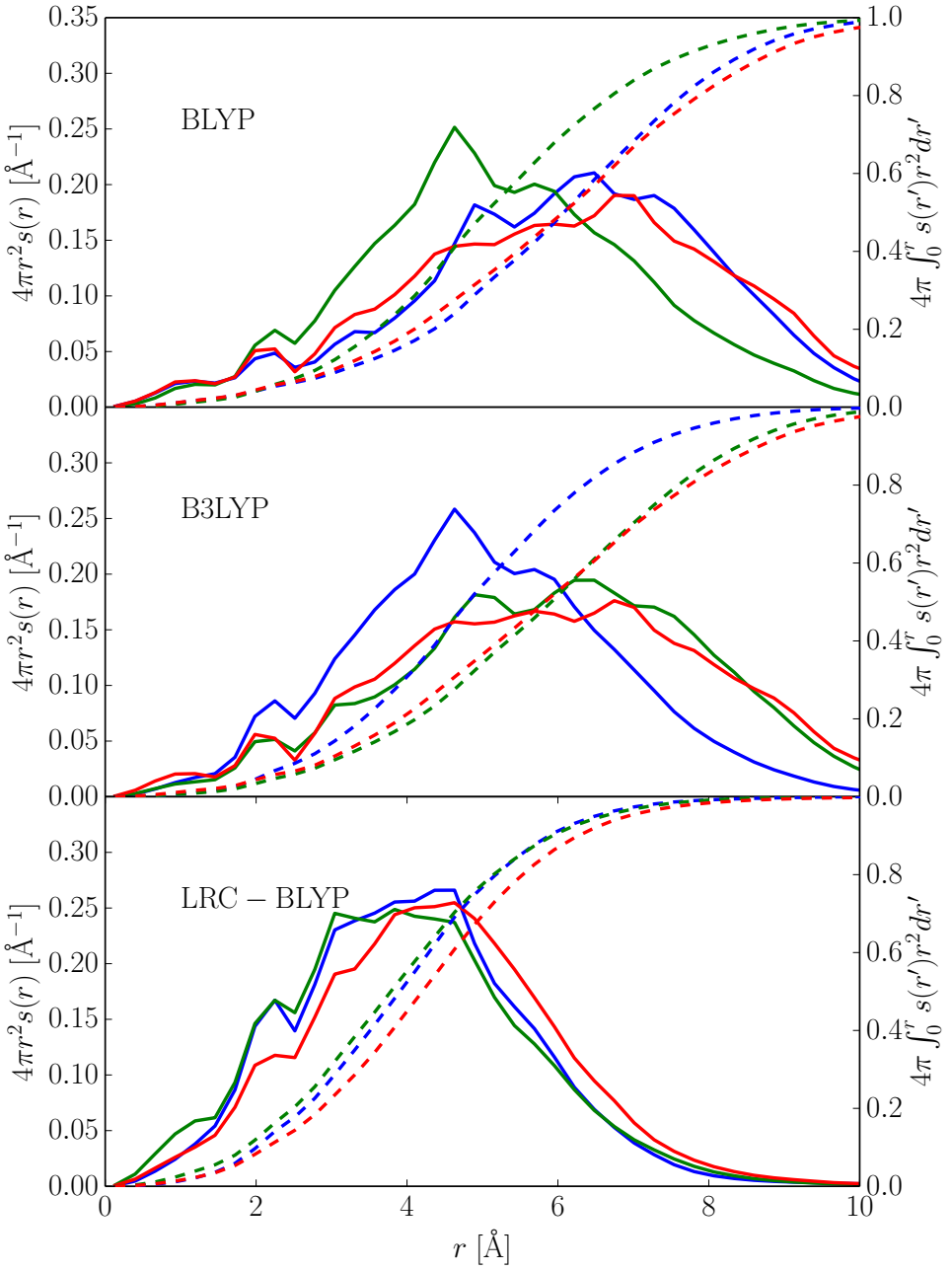

Figure A.2: Radial profiles of the first three excited-state spin densities with respect to the center of the ground-state spin density 500 fs after vertical excess electron attachment (solid lines). The cumulative integrals of the radial profiles are shown as dashed lines. The excited state spin densities were calculated with different density functionals, BLYP (top), B3LYP (middle) and LRC-BLYP (bottom).

Appendix B

Relationship between first excitation energy and radius of gyration for particle in a box

Here follows the derivation of the relationship between radius of gyration r_{g} and the first excitation energy for a particle in a (cubic) box. For a one-dimensional particle in a box of length L, the wavefunction ψ_0 reads:

$$\psi_0(x) = \sqrt{\frac{2}{L}} \sin\left(\frac{\pi x}{L}\right); \tag{B.1}$$

and the density:

$$\rho_0(x) = |\psi_0(x)|^2 = \frac{2}{L} \sin^2\left(\frac{\pi x}{L}\right). \tag{B.2}$$

The first moment μ_1 of this distribution is half of the box length L:

$$\mu_1 = \int_0^L \frac{2}{L} x \sin^2\left(\frac{\pi x}{L}\right) dx \tag{B.3}$$

$$= \frac{L}{2}. \tag{B.4}$$

The second moment of the distribution, μ_2, is related to the radius of gyration (r_{g}):

$$\mu_2 = r_{\mathrm{g}}^2 \tag{B.5}$$

and is for the one-dimensional particle in a box:

$$\mu_2 = \int_0^L \frac{2}{L} \sin^2(\left(\frac{\pi x}{L}\right))(x-\mu_1)^2 dx \tag{B.6}$$

$$\mu_2 = \frac{(\pi^2-6)}{12\pi^2} L^2 = r_{\mathrm{g}}^2. \tag{B.7}$$

The energies for a one-dimensional particle of mass m in a box are:

$$E(n) = \frac{hn^2}{8mL^2}. \tag{B.8}$$

Here, n is the quantum number. The excitation energy for a one-dimensional particle in a box from the ground to the first excited state is:

$$\Delta E\,(1 \to 2) = \frac{3h^2}{8mL^2} \tag{B.9}$$

and can be used to eliminate the box length L in eq. B.7 to give:

$$r_{\mathrm{g}}^2 = \frac{(\pi^2-6)\,\hbar^2}{8m\Delta E}. \tag{B.10}$$

With a Hartree $E_{\mathrm{h}} = \frac{\hbar^2}{m_e a_0}$ and a_0 being the Bohr radius this gives:

$$\Delta E = \frac{(\pi^2-6)\,E_{\mathrm{h}}}{8\,(r_{\mathrm{g}}/a_0)^2}. \tag{B.11}$$

Now, this was all for a particle in a 1D box. For a particle in a cubic 3D box eq B.7 changes to:

$$r_{\mathrm{g}}^2 = \frac{3\,(\pi^2-6)}{12\pi^2} L^2 \tag{B.12}$$

with the 3 lowest excitation energies being degenerate but still equal to B.9 and thus the relation B.10 changes to:

$$\Delta E = \frac{3\,(\pi^2-6)\,E_{\mathrm{h}}}{8\,(r_{\mathrm{g}}/a_0)^2}. \tag{B.13}$$

Appendix C

Additional figures for tuning of self-interaction correction

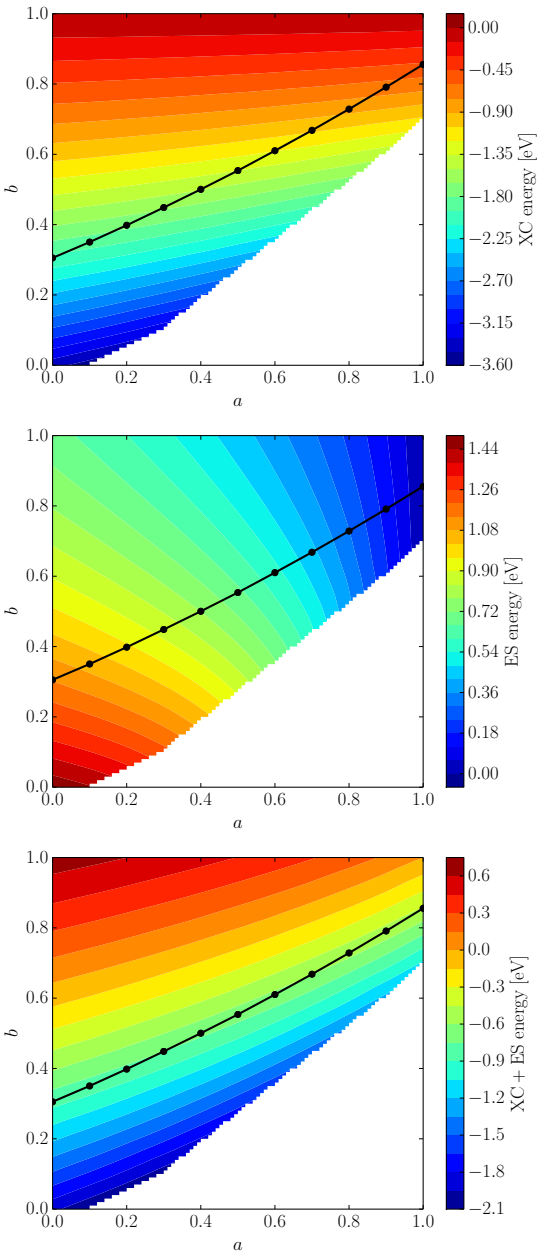

Figure C.1: Several quantities for $H_3O^+(H_2O)_3e^-$ cluster (see sec. 3.1) calculated with different parameter combinations in self-interaction correction from ref. 68. Top panel shows exchange-correlation (XC) energy of the spin density, middle panel the electrostatic (ES) self-energy of the spin density and bottom panel the sum of both quantities. Parameter combinations that lead to compliance with IP theorem in DFT are plotted as black dots in each plot. The empty region is due to non-convergent self-consistent field cycle within 50 iterations (using diagonalization of Fock matrix, started from optimized wavefunction obtained with orbital-transformation in preparatory calculations).

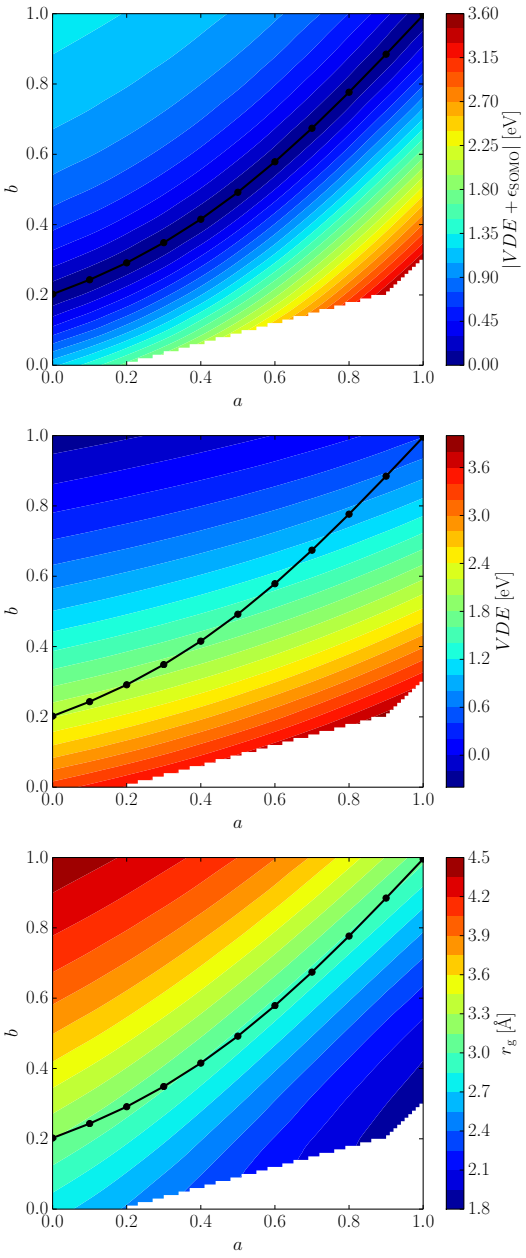

Figure C.2: Several quantities for $H_3O^+(H_2O)_3e^-$ cluster (see sec. 3.1) calculated with different parameter combinations in self-interaction correction from ref. 67. Top panel shows absolute values of sum of VDE and ϵ_{SOMO}, middle panel the VDE itself, and bottom panel the r_g of the spin density. Parameter combinations that lead to compliance with IP theorem in DFT are plotted as black dots in each plot. The empty region is due to non-convergent self-consistent field cycle within 50 iterations (using diagonalization of Fock matrix, started from optimized wavefunction obtained with orbital-transformation in preparatory calculations).

References

[1] A. C. Guyton and J. E. Hall. *Textbook of Medical Physiology*. Elsevier, Philadelphia, Pennsylvania, 2006. 1

[2] R. A. J. Freitas. *Nanomedicine*. Landes Bioscience, Austin, Texas, 1999. 1

[3] C. von Sonntag. *Free-Radical-Induced DNA Damage and Its Repair*. Springer, Berlin, 2006. 1, 2, 42

[4] W. Stiller. *Nichtthermisch aktivierte Chemie*. Birkhäuser Verlag, Basel, 1987. 1

[5] B. C. Garrett, D. A. Dixon, D. M. Camaioni, D. M. Chipman, M. A. Johnson, C. D. Jonah, G. A. Kimmel, J. H. Miller, T. N. Rescigno, P. J. Rossky, S. S. Xantheas, S. D. Colson, A. H. Laufer, D. Ray, P. F. Barbara, D. M. Bartels, K. H. Becker, H. Bowen, S. E. Bradforth, I. Carmichael, J. V. Coe, L. R. Corrales, J. P. Cowin, M. Dupuis, K. B. Eisenthal, J. A. Franz, M. S. Gutowski, K. D. Jordan, B. D. Kay, J. A. LaVerne, S. V. Lymar, T. E. Madey, C. W. McCurdy, D. Meisel, S. Mukamel, A. R. Nilsson, T. M. Orlando, N. G. Petrik, S. M. Pimblott, J. R. Rustad, G. K. Schenter, S. J. Singer, A. Tokmakoff, L. S. Wang, C. Wittig, and T. S. Zwier. Role of water in electron-initiated processes and radical chemistry: Issues and scientific advances. *Chem. Rev.*, 105(1):355–389, 2005. doi: 10.1021/cr030453x. 1, 2

[6] X. Chen and S. E. Bradforth. The ultrafast dynamics of photodetachment. *Annu. Rev. Phys. Chem.*, 59:203–231, 2008. doi: 10.1146/annurev.physchem.58.032806.104702. 1, 2

[7] C. L. Thomsen, D. Madsen, S. R. Keiding, J. Tho/gersen, and O. Christiansen. Two-photon dissociation and ionization of liquid water studied by femtosecond transient absorption spectroscopy. *J. Chem. Phys.*, 110(7):3453–3462, 1999. doi: 10.1063/1.478212. 1

[8] D. H. Son, P. Kambhampati, T. W. Kee, and P. F. Barbara. One-photon

UV detrapping of the hydrated electron. *Chem. Phys. Lett.*, 342(56):571 – 577, 2001. doi: 10.1016/S0009-2614(01)00167-1. 1

[9] P. Kambhampati, D. H. Son, T. W. Kee, and P. F. Barbara. Solvation dynamics of the hydrated electron depends on its initial degree of electron delocalization. *J. Phys. Chem. A*, 106(10):2374–2378, 2002. doi: 10.1021/jp014291p. 1, 51, 52

[10] X. Pan, P. Cloutier, D. Hunting, and L. Sanche. Dissociative electron attachment to DNA. *Phys. Rev. Lett.*, 90:208102, 2003. doi: 10.1103/PhysRevLett.90.208102. 1

[11] J. Gu, J. Leszczynski, and H. F. Schaefer. Interactions of electrons with bare and hydrated biomolecules: From nucleic acid bases to DNA segments. *Chem. Rev.*, 112(11):5603–5640, 2012. doi: 10.1021/cr3000219. 1

[12] H. A. Schwarz. Reaction of the hydrated electron with water. *J. Phys. Chem.*, 96(22):8937–8941, 1992. doi: 10.1021/j100201a044. 2, 66

[13] E. J. Hart and J. W. Boag. Absorption spectrum of hydrated electron in water and in aqueous solutions. *J. Am. Chem. Soc.*, 84(21):4090–4095, 1962. doi: 10.1021/ja00880a025. 2

[14] J. V. Coe, S. M. Williams, and K. H. Bowen. Photoelectron spectra of hydrated electron clusters vs. cluster size: Connecting to bulk. *Int. Rev. Phys. Chem.*, 27(1):27–51, 2008. doi: 10.1080/01442350701783543. 2, 44

[15] G. Lee, S. Arnold, J. Eaton, H. Sarkas, K. Bowen, C. Ludewigt, and H. Haberland. Negative ion photoelectron spectroscopy of solvated electron cluster anions, $(H_2O)_n^-$ and $(NH_3)_n^-$. *Z. Phys. D Atom. Mol. Cl.*, 20 (1):9–12, 1991. doi: 10.1007/BF01543925. 2

[16] J. R. R. Verlet, A. E. Bragg, A. Kammrath, O. Cheshnovsky, and D. M. Neumark. Observation of large water-cluster anions with surface-bound excess electrons. *Science*, 307(5706):93–96, 2005. doi: 10.1126/science.1106719. 2

[17] L. Ma, K. Majer, F. Chirot, and B. von Issendorff. Low temperature photoelectron spectra of water cluster anions. *J. Chem. Phys.*, 131(14):144303–144309, 2009. doi: 10.1063/1.3245859. 3

[18] R. M. Young, M. A. Yandell, S. B. King, and D. M. Neumark. Thermal effects on energetics and dynamics in water cluster anions $(h_2o)_n$. *J. Chem. Phys.*, 136(9):094304, 2012. doi: 10.1063/1.3689439. 3

[19] O. Marsalek, F. Uhlig, and P. Jungwirth. Electrons in cold water clusters: an ab initio molecular dynamics study of localization and metastable states. *J. Phys. Chem.*, 114:20489–20495, 2010. doi: 10.1021/jp1049028. 3

[20] O. Marsalek, F. Uhlig, T. Frigato, B. Schmidt, and P. Jungwirth. Dynamics of electron localization in warm versus cold water clusters. *Phys. Rev. Lett.*, 105(4):43002, 2010. doi: 10.1103/PhysRevLett.105.043002. 3

[21] A. Madarász, P. J. Rossky, and L. Turi. Response of observables for cold anionic water clusters to cluster thermal history. *J. Phys. Chem. A*, 114 (6):2331–2337, 2010. doi: 10.1021/jp908876f. 3

[22] T. Frigato, J. VandeVondele, B. Schmidt, C. Schutte, and P. Jungwirth. Ab initio molecular dynamics simulation of a medium-sized water cluster anion: From an interior to a surface-located excess electron via a delocalized state. *J. Phys. Chem. A*, 112(27):6125–6133, 2008. doi: 10.1021/jp711545s. 3, 44, 45

[23] L. D. Jacobson and J. M. Herbert. Theoretical characterization of four distinct isomer types in hydrated-electron clusters, and proposed assignments for photoelectron spectra of water cluster anions. *J. Am. Chem. Soc.*, 133: 19889–19899, 2011. doi: 10.1021/ja208024p. 3, 52

[24] O. Marsalek, F. Uhlig, J. VandeVondele, and P. Jungwirth. Structure, dynamics, and reactivity of hydrated electrons by ab initio molecular dynamics. *Acc. Chem. Res.*, 45(1):23–32, 2012. doi: 10.1021/ar200062m. 3

[25] B. Winter and M. Faubel. Photoemission from liquid aqueous solutions. *Chem. Rev.*, 106(4):1176–1211, 2006. doi: 10.1021/cr040381p. 3

[26] A. T. Shreve, T. A. Yen, and D. M. Neumark. Photoelectron spectroscopy of hydrated electrons. *Chem. Phys. Lett.*, 493(4-6):216–219, 2010. doi: 10.1016/j.cplett.2010.05.059. 3, 36

[27] Y. Tang, H. Shen, K. Sekiguchi, N. Kurahashi, T. Mizuno, Y.-I. Suzuki, and T. Suzuki. Direct measurement of vertical binding energy of a hydrated electron. *Phys. Chem. Chem. Phys.*, 12(15):3653–5, 2010. doi: 10.1039/b925741a. 3, 36

[28] K. R. Siefermann, Y. X. Liu, E. Lugovoy, O. Link, M. Faubel, U. Buck, B. Winter, and B. Abel. Binding energies, lifetimes and implications of bulk and interface solvated electrons in water. *Nature Chem.*, 2(4):274–279, 2010. doi: doi:10.1038/nchem.580. 3, 36, 45, 46, 75

[29] F. Buchner, T. Schultz, and A. Lubcke. Solvated electrons at the water-air interface: Surface versus bulk signal in low kinetic energy photoelectron spectroscopy. *Phys. Chem. Chem. Phys.*, 14:5837–5842, 2012. doi: 10.1039/C2CP23305C. 3, 36

[30] D. M. Sagar, C. D. Bain, and J. R. R. Verlet. Hydrated electrons at the water/air interface. *J. Am. Chem. Soc.*, 132(20):6917–6919, 2010. doi: 10.1021/ja101176r. 3

[31] Y.-I. Yamamoto, Y.-I. Suzuki, G. Tomasello, T. Horio, S. Karashima, R. Mitríc, and T. Suzuki. Time- and angle-resolved photoemission spectroscopy of hydrated electrons near a liquid water surface. *Phys. Rev. Lett.*, 112:187603, 2014. doi: 10.1103/PhysRevLett.112.187603. 3

[32] M. H. Elkins, H. L. Williams, A. T. Shreve, and D. M. Neumark. Relaxation mechanism of the hydrated electron. *Science*, 342(6165):1496–1499, 2013. doi: 10.1126/science.1246291. 3, 51

[33] L. Turi and P. J. Rossky. Theoretical studies of spectroscopy and dynamics of hydrated electrons. *Chem. Rev.*, 112(11):5641–5674, 2012. doi: 10.1021/cr300144z. 3, 4, 40, 43, 44, 74, 75

[34] V. P. Vysotskiy, L. S. Cederbaum, T. Sommerfeld, V. K. Voora, and K. D. Jordan. Benchmark calculations of the energies for binding excess electrons to water clusters. *J. Chem. Theory Comput.*, 8(3):893–900, 2012. doi: 10.1021/ct200925x. 3, 36

[35] R. N. Barnett, R. Giniger, O. Cheshnovsky, and U. Landman. Dielectron attachment and hydrogen evolution reaction in water clusters. *J. Phys. Chem. A*, 115(25):7378–7391, 2011. doi: 10.1021/jp201560n. 3

[36] M. Boero, M. Parrinello, K. Terakura, T. Ikeshoji, and C. C. Liew. First-principles molecular-dynamics simulations of a hydrated electron in normal and supercritical water. *Phys. Rev. Lett.*, 90(22):226403, 2003. doi: 10.1103/PhysRevLett.90.226403. 3, 66

[37] M. Boero. Excess electron in water at different thermodynamic conditions. *J. Phys. Chem. A*, 111(49):12248–12256, 2007. doi: 10.1021/jp074356. 3, 66

[38] R. E. Larsen, W. J. Glover, and B. J. Schwartz. Does the hydrated electron occupy a cavity? *Science*, 329(5987):65–69, 2010. doi: 10.1126/science.1189588. 4, 43, 44, 65, 75

[39] M. Natori and T. Watanabe. Structural model of the hydrated electron. *J. Phys. Soc. Jpn.*, 21(8):1573–1578, 1966. doi: 10.1143/JPSJ.21.1573. 4, 74

[40] D.-F. Feng and L. Kevan. Theoretical models for solvated electrons. *Chem. Rev.*, 80(1):1–20, 1980. doi: 10.1021/cr60323a001. 4, 40

[41] L. Turi and A. Madarasz. Comment on "Does the hydrated electron occupy a cavity?". *Science*, 331(6023):1387–c, 2011. doi: 10.1126/science.1197559. 4

[42] L. D. Jacobson and J. M. Herbert. Comment on "Does the hydrated electron occupy a cavity?". *Science*, 331(6023):1387–d, 2011. doi: 10.1126/science.1198191. 4

[43] R. E. Larsen, W. J. Glover, and B. J. Schwartz. Response to comments on "Does the hydrated electron occupy a cavity?". *Science*, 331(6023):1387, 2011. doi: 10.1126/science.1197884. 4

[44] J. M. Herbert and L. D. Jacobson. Structure of the aqueous electron: Assessment of one-electron pseudopotential models in comparison to experimental data and time-dependent density functional theory. *J. Phys. Chem. A*, 115(50):14470–14483, 2011. doi: 10.1021/jp206391d. 4, 48

[45] J. R. Casey, A. Kahros, and B. J. Schwartz. To be or not to be in a cavity: The hydrated electron dilemma. *J. Phys. Chem. B*, 117(46):14173–14182, 2013. doi: 10.1021/jp407912k. 4

[46] M. P. Allen and D. J. Tildesley. *Computer Simulation of Liquids*. Oxford Science Publications, Oxford, 1986. 6, 10, 23, 27

[47] D. Marx and J. Hutter. *Ab Initio Molecular Dynamics - Basic Theory and Advanced Methods*. Cambridge University Press, Cambridge, 2009. 6, 8, 10, 11

[48] N. C. Handy and A. M. Lee. The adiabatic approximation. *Chem. Phys. Lett.*, 252(56):425 – 430, 1996. doi: 10.1016/0009-2614(96)00171-6. 8

[49] M. Born and R. Oppenheimer. Zur Quantentheorie der Molekeln. *Ann. Phys.*, 389(20):457–484, 1927. doi: 10.1002/andp.19273892002. 8

[50] D. J. Tannor. *Introduction to Quantum Mechanics - A Time-dependent Perspective*. University Science Books, Sausalito, California, 2007. 8

[51] P. Ehrenfest. Bemerkung über die angenäherte Gültigkeit der klassischen Mechanik innerhalb der Quantenmechanik. *Z. Physik*, 45(7-8):455–457, 1927. doi: 10.1007/BF01329203. 9

[52] H. Hellmann. *Einführung in die Quantenchemie*. Deuticke, Leipzig, 1937. 10

[53] R. P. Feynman. Forces in molecules. *Phys. Rev.*, 56:340–343, 1939. doi: 10.1103/PhysRev.56.340. 10

[54] W. C. Swope, H. C. Andersen, P. H. Berens, and K. R. Wilson. A computer simulation method for the calculation of equilibrium constants for the formation of physical clusters of molecules: Application to small water clusters. *J. Chem. Phys.*, 76(1):637–649, 1982. doi: 10.1063/1.442716. 10

[55] J. Hutter. Car-parrinello molecular dynamics. *WIREs Comput. Mol. Sci.*, 2(4):604–612, 2012. doi: 10.1002/wcms.90. 10

[56] J. Kolafa. Time-reversible always stable predictor-corrector method for molecular dynamics of polarizable molecules. *J. Comput. Chem.*, 25(3): 335–342, 2004. doi: 10.1002/jcc.10385. 10

[57] J. VandeVondele and J. Hutter. An efficient orbital transformation method for electronic structure calculations. *J. Chem. Phys.*, 118(10):4365–4369, 2003. doi: 10.1063/1.1543154. 10

[58] W. Koch and M. C. Holthausen. *A Chemist's Guide to Density Functional Theory*. Wiley-VCH, Weinheim, 2002. 11, 14

[59] J. Kohanoff. *Electronic Structure Calculations for Solids and Molecules*. Cambridge University Press, Cambridge, 2006. 11

[60] P. Hohenberg and W. Kohn. Inhomogeneous electron gas. *Phys. Rev.*, 136: B864–B871, 1964. doi: 10.1103/PhysRev.136.B864. 11

[61] W. Kohn and L. J. Sham. Self-consistent equations including exchange and correlation effects. *Phys. Rev.*, 140:A1133–A1138, 1965. doi: 10.1103/PhysRev.140.A1133. 12

[62] J. VandeVondele, M. Krack, F. Mohamed, M. Parrinello, T. Chassaing, and J. Hutter. QUICKSTEP: Fast and accurate density functional calculations using a mixed gaussian and plane waves approach. *Comput. Phys. Commun.*, 167(2):103–128, 2005. doi: 10.1016/j.cpc.2004.12.014. 12

[63] S. Goedecker, M. Teter, and J. Hutter. Separable dual-space gaussian pseudopotentials. *Phys. Rev. B*, 54(3):1703–1710, 1996. doi: 10.1103/PhysRevB.58.3641. 13, 33

[64] M.-C. Kim, E. Sim, and K. Burke. Understanding and reducing errors in density functional calculations. *Phys. Rev. Lett.*, 111:073003, 2013. doi: 10.1103/PhysRevLett.111.073003. 14

[65] R. G. Parr and W. Yang. *Density-Functional Theory of Atoms and Molecules*. Oxford Science Publications, Oxford, 1989. 14

[66] J. P. Perdew and A. Zunger. Self-interaction correction to density-functional approximations for many-electron systems. *Phys. Rev. B*, 23:5048–5079, 1981. doi: 10.1103/PhysRevB.23.5048. 14, 77

[67] M. D'Avezac, M. Calandra, and F. Mauri. Density functional theory description of hole-trapping in SiO_2 : A self-interaction-corrected approach. *Phys. Rev. B*, 71(20):205210, 2005. doi: 10.1103/PhysRevB.71.205210. 14, 70, 85, 106

[68] J. VandeVondele and M. Sprik. A molecular dynamics study of the hydroxyl radical in solution applying self-interaction-corrected density functional methods. *Phys. Chem. Chem. Phys.*, 7:1363–1367, 2005. doi: 10.1039/B501603G. 14, 15, 37, 68, 70, 76, 77, 84, 104, 105

[69] G. Pacchioni, F. Frigoli, D. Ricci, and J. A. Weil. Theoretical description of hole localization in a quartz Al center: The importance of exact electron exchange. *Phys. Rev. B*, 63:054102, 2000. doi: 10.1103/PhysRevB.63.054102. 15

[70] J. Lægsgaard and K. Stokbro. Hole trapping at Al impurities in silica: A challenge for density functional theories. *Phys. Rev. Lett.*, 86:2834–2837, 2001. doi: 10.1103/PhysRevLett.86.2834. 15

[71] R. Baer, E. Livshits, and U. Salzner. Tuned range-separated hybrids in density functional theory. *Annu. Rev. Phys. Chem.*, 61(1):85–109, 2010. doi: 10.1146/annurev.physchem.012809.103321. 15, 67

[72] H. Iikura, T. Tsuneda, T. Yanai, and K. Hirao. A long-range correction scheme for generalized-gradient-approximation exchange functionals. *J. Chem. Phys.*, 115:3540–3544, 2001. 15, 34, 49

[73] J. P. Perdew, R. G. Parr, M. Levy, and J. L. Balduz. Density-functional theory for fractional particle number: Derivative discontinuities of the energy.

Phys. Rev. Lett., 49:1691–1694, 1982. doi: 10.1103/PhysRevLett.49.1691. 15

[74] J. P. Perdew and M. Levy. Comment on "Significance of the highest occupied Kohn-Sham eigenvalue". *Phys. Rev. B*, 56:16021–16028, 1997. doi: 10.1103/PhysRevB.56.16021. 15

[75] C. T. Kelley. *Iterative Methods for Optimization*. Society for Industrial and Applied Mathematics, Raleigh, North Carolina, 1999. 16

[76] G. Henkelman, G. Jhannesson, and H. Jnsson. Methods for finding saddle points and minimum energy paths. In S. Schwartz, editor, *Theoretical Methods in Condensed Phase Chemistry*, volume 5 of *Progress in Theoretical Chemistry and Physics*, pages 269–302. 2002. doi: 10.1007/0-306-46949-9_10. 16

[77] E. Bitzek, P. Koskinen, F. Gähler, M. Moseler, and P. Gumbsch. Structural relaxation made simple. *Phys. Rev. Lett.*, 97:170201, 2006. doi: 10.1103/PhysRevLett.97.170201. 16

[78] G. Henkelman and H. Jonsson. Improved tangent estimate in the nudged elastic band method for finding minimum energy paths and saddle points. *J. Chem. Phys.*, 113(22):9978–9985, 2000. doi: 10.1063/1.1323224. 17

[79] G. Henkelman, B. Uberuaga, and H. Jonsson. A climbing image nudged elastic band method for finding saddle points and minimum energy paths. *J. Chem. Phys.*, 113(22):9901–9904, 2000. doi: 10.1063/1.1329672. 17, 18

[80] R. Elber and M. Karplus. A method for determining reaction paths in large molecules - application to myoglobin. *Chem. Phys. Lett.*, 139(5):375–380, 1987. doi: 10.1016/0009-2614(87)80576-6. 17

[81] M. E. Casida. Time-dependent density-functional theory for molecules and molecular solids. *J. Mol. Struct. (Theochem)*, 914(1-3):3 – 18, 2009. doi: 10.1016/j.theochem.2009.08.018. 18

[82] M. A. L. Marques, C. A. Ullrich, F. Nogueira, A. Rubio, K. Burke, and E. K. U. Gross. *Time-Dependent Density Functional Theory*. Springer, Berlin, 2006. 18, 30

[83] A. Dreuw and M. Head-Gordon. Single-reference ab initio methods for the calculation of excited states of large molecules. *Chem. Rev.*, 105(11):4009–4037, 2005. doi: 10.1021/cr0505627. 18, 20, 30, 31, 49

[84] E. Runge and E. K. U. Gross. Density-functional theory for time-dependent systems. *Phys. Rev. Lett.*, 52:997–1000, 1984. doi: 10.1103/PhysRevLett.52.997. 18

[85] M. E. Casida. Time-dependent density functional response theory for molecules. In D. P. Chong, editor, *Recent Advances in Density Functional Methods, Part I*, volume I of *Recent Advances in Computational Chemistry*, chapter 5, pages 155–192. World Scientific, River Edge, NJ, 1995. 19, 20

[86] F. Furche and R. Ahlrichs. Adiabatic time-dependent density functional methods for excited state properties. *J. Chem. Phys.*, 117(16):7433–7447, 2002. doi: 10.1063/1.1508368. 20, 30

[87] F. Furche. On the density matrix based approach to time-dependent density functional response theory. *J. Chem. Phys.*, 114(14):5982–5992, 2001. doi: 10.1063/1.1353585. 20, 30

[88] J. G. Ángyán. Common theoretical framework for quantum chemical solvent effect theories. *J. Math. Chem.*, 10(1):93–137, 1992. doi: 10.1007/BF01169172. 21

[89] J. Tomasi, B. Mennucci, and R. Cammi. Quantum mechanical continuum solvation models. *Chem. Rev.*, 105(8):2999–3094, 2005. doi: 10.1021/cr9904009. 21

[90] A. Klamt and G. Schüürmann. Cosmo: a new approach to dielectric screening in solvents with explicit expressions for the screening energy and its gradient. *J. Chem. Soc., Perkin Trans. 2*, pages 799–805, 1993. doi: 10.1039/P29930000799. 21

[91] V. Barone and M. Cossi. Quantum calculation of molecular energies and energy gradients in solution by a conductor solvent model. *J. Phys. Chem. A*, 102(11):1995–2001, 1998. doi: 10.1021/jp9716997. 21

[92] M. Cossi, N. Rega, G. Scalmani, and V. Barone. Energies, structures, and electronic properties of molecules in solution with the C-PCM solvation model. *J. Comput. Chem.*, 24(6):669–681, 2003. doi: 10.1002/jcc.10189. 21

[93] M. Cossi and V. Barone. Solvent effect on vertical electronic transitions by the polarizable continuum model. *J. Chem. Phys.*, 112(5):2427–2435, 2000. doi: 10.1063/1.480808. 22, 34

[94] A. Toukmaji and J. Board. Ewald summation techniques in perspective: A survey. *Comput. Phys. Commun.*, 95(2-3):73–92, 1996. doi: 10.1016/0010-4655(96)00016-1. 23, 24

[95] P. P. Ewald. Die Berechnung optischer und elektrostatischer Gitterpotentiale. *Ann. Phys.*, 369(3):253–287, 1921. doi: 10.1002/andp.19213690304. 23

[96] L. Genovese, T. Deutsch, and S. Goedecker. Efficient and accurate three-dimensional poisson solver for surface problems. *J. Chem. Phys.*, 127(5), 2007. doi: 10.1063/1.2754685. 24

[97] A. Arnold and C. Holm. A novel method for calculating electrostatic interactions in 2d periodic slab geometries. *Chem. Phys. Lett.*, 354(34):324 – 330, 2002. doi: 10.1016/S0009-2614(02)00131-8. 24

[98] J. S. Hub, B. L. de Groot, H. Grubmller, and G. Groenhof. Quantifying artifacts in Ewald simulations of inhomogeneous systems with a net charge. *J. Chem. Theory Comput.*, 10(1):381–390, 2014. doi: 10.1021/ct400626b. 24, 63

[99] I.-F. W. Kuo and C. J. Mundy. An ab initio molecular dynamics study of the aqueous liquid-vapor interface. *Science*, 303(5658):658–660, 2004. doi: 10.1126/science.1092787. 24

[100] J. Schmidt, J. VandeVondele, I.-F. W. Kuo, D. Sebastiani, J. I. Siepmann, J. Hutter, and C. J. Mundy. Isobaric-isothermal molecular dynamics simulations utilizing density functional theory: An assessment of the structure and density of water at near-ambient conditions. *J. Phys. Chem. B*, 113 (35):11959–11964, 2009. doi: 10.1021/jp901990u. 24

[101] A. Warshel and M. Levitt. Theoretical studies of enzymic reactions: Dielectric, electrostatic and steric stabilization of the carbonium ion in the reaction of lysozyme. *J. Mol. Biol.*, 103(2):227 – 249, 1976. doi: 10.1016/0022-2836(76)90311-9. 24

[102] T. Laino, F. Mohamed, A. Laio, and M. Parrinello. An efficient real space multigrid QM/MM electrostatic coupling. *J. Chem. Theory Comput.*, 1(6): 1176–1184, 2005. doi: 10.1021/ct050123f. 25

[103] T. Laino, F. Mohamed, A. Laio, and M. Parrinello. An efficient linear-scaling electrostatic coupling for treating periodic boundary conditions in QM/MM simulations. *J. Chem. Theory Comput.*, 2(5):1370–1378, 2006. doi: 10.1021/ct6001169. 25

[104] P. K. Biswas and V. Gogonea. A regularized and renormalized electrostatic coupling Hamiltonian for hybrid quantum-mechanical–molecular-mechanical calculations. *J. Chem. Phys.*, 123(16), 2005. doi: 10.1063/1.2064907. 25

[105] P. E. Blöchl. Electrostatic decoupling of periodic images of plane-wave-expanded densities and derived atomic point charges. *J. Chem. Phys.*, 103 (17):7422–7428, 1995. doi: 10.1063/1.470314. 26

[106] A. P. Willard and D. Chandler. Instantaneous liquid interfaces. *J. Phys. Chem. B*, 114(5):1954–1958, 2010. doi: 10.1021/jp909219k. 27, 29

[107] M. J. Frisch, G. W. Trucks, H. B. Schlegel, G. E. Scuseria, M. A. Robb, J. R. Cheeseman, G. Scalmani, V. Barone, B. Mennucci, G. A. Petersson, H. Nakatsuji, M. Caricato, X. Li, H. P. Hratchian, A. F. Izmaylov, J. Bloino, G. Zheng, J. L. Sonnenberg, M. Hada, M. Ehara, K. Toyota, R. Fukuda, J. Hasegawa, M. Ishida, T. Nakajima, Y. Honda, O. Kitao, H. Nakai, T. Vreven, J. A. Montgomery, Jr., J. E. Peralta, F. Ogliaro, M. Bearpark, J. J. Heyd, E. Brothers, K. N. Kudin, V. N. Staroverov, R. Kobayashi, J. Normand, K. Raghavachari, A. Rendell, J. C. Burant, S. S. Iyengar, J. Tomasi, M. Cossi, N. Rega, J. M. Millam, M. Klene, J. E. Knox, J. B. Cross, V. Bakken, C. Adamo, J. Jaramillo, R. Gomperts, R. E. Stratmann, O. Yazyev, A. J. Austin, R. Cammi, C. Pomelli, J. W. Ochterski, R. L. Martin, K. Morokuma, V. G. Zakrzewski, G. A. Voth, P. Salvador, J. J. Dannenberg, S. Dapprich, A. D. Daniels, O. Farkas, J. B. Foresman, J. V. Ortiz, J. Cioslowski, and D. J. Fox. Gaussian 09 Revision A.1. Gaussian Inc. Wallingford CT 2009. 27, 34

[108] F. Uhlig, O. Marsalek, and P. Jungwirth. Unraveling the complex nature of the hydrated electron. *J. Phys. Chem. Lett.*, 3(20):3071–3075, 2012. doi: 10.1021/jz301449f. 29, 43, 45, 61

[109] A. Lange and J. M. Herbert. Simple methods to reduce charge-transfer contamination in time-dependent density-functional calculations of clusters and liquids. *J. Chem. Theory Comput.*, 3(5):1680–1690, 2007. doi: 10.1021/ct700125v. 31, 49

[110] S. R. Bahn and K. W. Jacobsen. An object-oriented scripting interface to a legacy electronic structure code. *Comput. Sci. Eng.*, 4(3):56–66, 2002. doi: 10.1109/5992.998641. 31

[111] TURBOMOLE V6.2 2010, a development of University of Karlsruhe and Forschungszentrum Karlsruhe GmbH, 1989-2007, TURBOMOLE GmbH,

since 2007; available from
`http://www.turbomole.com`. 32

[112] A. Wilson, T. van Mourik, and T. Dunning. Gaussian basis sets for use in correlated molecular calculations. 6. Sextuple zeta correlation consistent basis sets for boron through neon. *J. Mol. Struct. (Theochem)*, 388:339–349, 1996. doi: 10.1016/S0166-1280(96)80048-0. 32

[113] F. Neese. The ORCA program system. *WIREs Comput. Mol. Sci.*, 2(1): 73–78, 2012. doi: 10.1002/wcms.81. 32

[114] W. Hehre, R. Ditchfield, and J. Pople. Self-consistent molecular-orbital methods. 12. Further extensions of gaussian-type basis sets for use in molecular-orbital studies of organic molecules. *J. Chem. Phys.*, 56(5):2257–2261, 1972. doi: 10.1063/1.1677527. 32, 34

[115] R. Krishnan, J. Binkley, R. Seeger, and J. Pople. Self-consistent molecular-orbital methods .20. basis set for correlated wave-functions. *J. Chem. Phys.*, 72(1):650–654, 1980. doi: 10.1063/1.438955. 32, 34

[116] G. Bussi, D. Donadio, and M. Parrinello. Canonical sampling through velocity rescaling. *J. Chem. Phys.*, 126(1):014101–014108, 2007. doi: 10.1063/1.2408420. 32, 33

[117] H. J. C. Berendsen, J. P. M. Postma, W. F. van Gunsteren, A. DiNola, and J. R. Haak. Molecular dynamics with coupling to an external bath. *J. Chem. Phys.*, 81(8):3684–3690, 1984. doi: 10.1063/1.448118. 32

[118] S. Pronk, S. Páll, R. Schulz, P. Larsson, P. Bjelkmar, R. Apostolov, M. R. Shirts, J. C. Smith, P. M. Kasson, D. van der Spoel, B. Hess, and E. Lindahl. Gromacs 4.5: a high-throughput and highly parallel open source molecular simulation toolkit. *Bioinformatics*, 29(7):845–854, 2013. doi: 10.1093/bioinformatics/btt055. 32

[119] U. Essmann, L. Perera, M. L. Berkowitz, T. Darden, H. Lee, and L. G. Pedersen. A smooth particle mesh ewald method. *J. Chem. Phys.*, 103(19): 8577–8593, 1995. doi: 10.1063/1.470117. 33

[120] J. VandeVondele and J. Hutter. Gaussian basis sets for accurate calculations on molecular systems in gas and condensed phases. *J. Chem. Phys.*, 127 (11), 2007. doi: 10.1063/1.2770708. 33

[121] A. D. Becke. Density-functional exchange-energy approximation with correct asymptotic-behavior. *Phys. Rev. A*, 38(6):3098–3100, 1988. doi: 10.1103/PhysRevA.38.3098. 33

[122] C. T. Lee, W. T. Yang, and R. G. Parr. Development of the Colle-Salvetti correlation-energy formula into a functional of the electron-density. *Phys. Rev. B*, 37(2):785–789, 1988. doi: 10.1103/PhysRevB.37.785. 33

[123] R. Jonchiere, A. P. Seitsonen, G. Ferlat, A. M. Saitta, and R. Vuilleumier. Van der Waals effects in ab initio water at ambient and supercritical conditions. *J. Chem. Phys.*, 135(15), 2011. doi: 10.1063/1.3651474. 33

[124] S. Grimme, J. Antony, S. Ehrlich, and H. Krieg. A consistent and accurate ab initio parametrization of density functional dispersion correction (DFT-D) for the 94 elements H-Pu. *J. Chem. Phys.*, 132(15):154104–154123, 2010. doi: 10.1063/1.3382344. 33

[125] M. D. Baer, C. J. Mundy, M. J. McGrath, I. F. W. Kuo, J. I. Siepmann, and D. J. Tobias. Re-examining the properties of the aqueous vapor-liquid interface using dispersion corrected density functional theory. *J. Chem. Phys.*, 135(12):135–147, 2011. doi: 10.1063/1.3633239. 34

[126] H. Berendsen, J. Postma, W. Gunsteren, and J. Hermans. Interaction models for water in relation to protein hydration. In B. Pullman, editor, *Intermolecular Forces*, volume 14 of *The Jerusalem Symposia on Quantum Chemistry and Biochemistry*, pages 331–342. Springer Netherlands, 1981. ISBN 978-90-481-8368-5. doi: 10.1007/978-94-015-7658-1_21. 34

[127] Y. Tawada, T. Tsuneda, S. Yanagisawa, T. Yanai, and K. Hirao. A long-range corrected time-dependent density functional theory. *J. Chem. Phys.*, 120:8425–8433, 2004. doi: 10.1063/1.1688752. 34, 49

[128] A. D. Becke. Density-functional thermochemistry. III. The role of exact exchange. *J. Chem. Phys.*, 98:5648–5652, 1993. doi: 10.1063/1.464913. 34

[129] P. J. Stephens, F. J. Devlin, C. F. Chabalowski, and M. J. Frisch. Ab initio calculation of vibrational absorption and circular dichroism spectra using density functional force fields. *J. Phys. Chem.*, 98:11623–11627, 1994. doi: 10.1021/j100096a001. 34

[130] M. Valiev, E. J. Bylaska, N. Govind, K. Kowalski, T. P. Straatsma, H. J. J. van Dam, D. Wang, J. Nieplocha, E. Apra, T. L. Windus, and W. A. de Jong. NWChem: A comprehensive and scalable open-source solution for

large scale molecular simulations. *Comput. Phys. Comm.*, 181:1477–1489, 2010. doi: 10.1016/j.cpc.2010.04.018. 34

[131] Y. Shao, L. F. Molnar, Y. Jung, J. Kussmann, C. Ochsenfeld, S. T. Brown, A. T. Gilbert, L. V. Slipchenko, S. V. Levchenko, D. P. O'Neill, R. A. DiStasio Jr, R. C. Lochan, T. Wang, G. J. Beran, N. A. Besley, J. M. Herbert, C. Yeh Lin, T. Van Voorhis, S. Hung Chien, A. Sodt, R. P. Steele, V. A. Rassolov, P. E. Maslen, P. P. Korambath, R. D. Adamson, B. Austin, J. Baker, E. F. C. Byrd, H. Dachsel, R. J. Doerksen, A. Dreuw, B. D. Dunietz, A. D. Dutoi, T. R. Furlani, S. R. Gwaltney, A. Heyden, S. Hirata, C.-P. Hsu, G. Kedziora, R. Z. Khalliulin, P. Klunzinger, A. M. Lee, M. S. Lee, W. Liang, I. Lotan, N. Nair, B. Peters, E. I. Proynov, P. A. Pieniazek, Y. Min Rhee, J. Ritchie, E. Rosta, C. David Sherrill, A. C. Simmonett, J. E. Subotnik, H. Lee Woodcock III, W. Zhang, A. T. Bell, A. K. Chakraborty, D. M. Chipman, F. J. Keil, A. Warshel, W. J. Hehre, H. F. Schaefer III, J. Kong, A. I. Krylov, P. M. W. Gill, and M. Head-Gordon. Advances in methods and algorithms in a modern quantum chemistry program package. *Phys. Chem. Chem. Phys.*, 8:3172–3191, 2006. doi: 10.1039/B517914A. 34

[132] F. Uhlig, O. Marsalek, and P. Jungwirth. From a localized H_3O radical to a delocalized $H_3O^+ \cdots e^-$ solvent-separated pair by sequential hydration. *Phys. Chem. Chem. Phys.*, 13:14003–14009, 2011. doi: 10.1039/C1CP20764D. 36

[133] A. L. Sobolewski and W. Domcke. Hydrated hydronium: a cluster model of the solvated electron? *Phys. Chem. Chem. Phys.*, 4(1):4–10, 2002. doi: 10.1039/B107373G. 36, 39

[134] O. Marsalek, T. Frigato, J. VandeVondele, S. E. Bradforth, B. Schmidt, C. Schutte, and P. Jungwirth. Hydrogen forms in water by proton transfer to a distorted electron. *J. Phys. Chem. B*, 114(2):915–920, 2010. doi: 10.1021/jp908986z. 37, 74

[135] F. Uhlig and P. Jungwirth. Embedded cluster models for reactivity of the hydrated electron. *Z. Phys. Chem.*, 227(9-11):1583–1593, 2013. doi: 10.1524/zpch.2013.0402. 40

[136] I. A. Shkrob. The structure of the hydrated electron. Part 1. Magnetic resonance of internally trapping water anions: A density functional theory study. *J. Phys. Chem. A*, 111(24):5223–5231, 2007. doi: 10.1021/jp068278m. 40

[137] C.-G. Zhan and D. A. Dixon. The nature and absolute hydration free energy of the solvated electron in water. *J. Phys. Chem. B*, 107(18):4403–4417, 2003. doi: 10.1021/jp022326v. 40, 59

[138] E. Hart and M. Anbar. *The hydrated electron*. Wiley-Interscience, New York, 1970. 41

[139] K. Takahashi, S. Ohgami, Y. Koyama, S. Sawamura, T. W. Marin, D. M. Bartels, and C. D. Jonah. Reaction rates of the hydrated electron with N_2O in high temperature water and potential surface of the N_2O^- anion. *Chem. Phys. Lett.*, 383(56):445 – 450, 2004. doi: 10.1016/j.cplett.2003.11.050. 42

[140] P. Jungwirth and B. Winter. Ions at aqueous interfaces: From water surface to hydrated proteins. *Annu. Rev. Phys. Chem.*, 59(1):343–366, 2008. doi: 10.1146/annurev.physchem.59.032607.093749. 45, 47

[141] A. Madarász, P. J. Rossky, and L. Turi. Excess electron relaxation dynamics at water/air interfaces. *J. Chem. Phys.*, 126(23):–, 2007. doi: 10.1063/1.2741514. 45

[142] F. Uhlig, O. Marsalek, and P. Jungwirth. Electron at the surface of water: Dehydrated or not? *J. Phys. Chem. Lett.*, 4(2):338–343, 2013. doi: 10.1021/jz3020953. 45, 57

[143] R. Vácha, F. Uhlig, and P. Jungwirth. Charges at aqueous interfaces: Development of computational approaches in direct contact with experiment. *Adv. Chem. Phys.*, 155:69–96, 2014. doi: 10.1002/9781118755815.ch02. 47, 63

[144] L. Onsager and N. N. T. Samaras. The surface tension of DebyeHückel electrolytes. *J. Chem. Phys.*, 2(8):528–536, 1934. doi: 10.1063/1.1749522. 47

[145] P. Cieplak, F.-Y. Dupradeau, Y. Duan, and J. Wang. Polarization effects in molecular mechanical force fields. *J. Phys. - Cond. Matt.*, 21(33):333102, 2009. doi: 10.1088/0953-8984/21/33/333102. 47

[146] F. Uhlig, J. M. Herbert, M. P. Coons, and P. Jungwirth. Optical spectroscopy of the bulk and interfacial hydrated electron from ab initio calculations. 0(0), 2014. doi: 10.1021/jp5004243. 48

[147] J. Savolainen, F. Uhlig, S. Ahmed, P. Hamm, and P. Jungwirth. Direct observation of the collapse of the delocalized excess electron in water. *Nature Chem.*, accepted for publication, 2014. 51

[148] J. Jortner and R. M. Noyes. Some thermodynamic properties of the hydrated electron. *J. Phys. Chem.*, 70(3):770–774, 1966. doi: 10.1021/j100875a026. 59

[149] D. M. Bartels, K. Takahashi, J. A. Cline, T. W. Marin, and C. D. Jonah. Pulse radiolysis of supercritical water. 3. Spectrum and thermodynamics of the hydrated electron. *J. Phys. Chem. A*, 109(7):1299–1307, 2005. doi: 10.1021/jp0457141. 59

[150] R. M. Noyes. Assignment of individual ionic contributions to properties of aqueous ions. *J. Am. Chem. Soc.*, 86(6):971–979, 1964. doi: 10.1021/ja01060a001. 59

[151] J. V. Coe. Fundamental properties of bulk water from cluster ion data. *Int. Rev. Phys. Chem.*, 20(1):33–58, 2001. doi: 10.1080/01442350010008589. 59

[152] R. W. Zwanzig. Hightemperature equation of state by a perturbation method. I. Nonpolar gases. *J. Chem. Phys.*, 22(8):1420–1426, 1954. doi: 10.1063/1.1740409. 59

[153] M. D. Tissandier, K. A. Cowen, W. Y. Feng, E. Gundlach, M. H. Cohen, A. D. Earhart, J. V. Coe, and T. R. Tuttle. The proton's absolute aqueous enthalpy and Gibbs free energy of solvation from cluster-ion solvation data. *J. Phys. Chem. A*, 102(40):7787–7794, 1998. doi: 10.1021/jp982638r. 62

[154] C. Chipot and A. Pohorille. *Free energy calculations*. Springer, Berlin, 2007. 62

[155] G. Torrie and J. Valleau. Nonphysical sampling distributions in Monte Carlo free-energy estimation: Umbrella sampling. *J. Comput. Phys.*, 23(2): 187 – 199, 1977. doi: 10.1016/0021-9991(77)90121-8. 63

[156] C. Adamo and V. Barone. Toward chemical accuracy in the computation of NMR shieldings: The PBE0 model. *Chem. Phys. Lett.*, 298:113–119, 1998. doi: 10.1016/S0009-2614(98)01201-9. 66

[157] J. P. Perdew, K. Burke, and M. Ernzerhof. Generalized gradient approximation made simple. *Phys. Rev. Lett.*, 77:3865–3868, 1996. doi: 10.1103/PhysRevLett.77.3865. 67

List of Figures

List of Tables

List of Abbreviations

AIMD ab initio molecular dynamics, page 9

ASPC always stable predictor-corrector, page 10

BOMD Born-Oppenheimer molecular dynamics, page 9

CMD classical molecular dynamics, page 6

DF density functional, page 14

DFT density functional theory, page 6

FFMD force-field molecular dynamics, page 32

FFT fast Fourier transform, page 13

FPMD first principles molecular dynamics, page 9

GGA Generalized-gradient approximation, page 13

GGG grid of Gaussian ghosts, page 33

GTO Gaussian-type orbitals, page 13

HF Hartree-Fock, page 11

KS Kohn-Sham, page 12

LDA Local density approximation, page 13

LRC long-range corrected, page 15

LSD local spin density, page 14

MD Molecular Dynamics, page 6

MP2 second-order Møller-Plesset perturbation theory, page 32

OEPP one-electron pseudopotential, page 3

OT orbital transformation, page 10

PES photoelectron spectroscopy, page 2

PP pseudopotential, page 13

PW plane wave, page 13

SIC self-interaction correction, page 14

SIE self-interaction error, page 14

SPC simple point charge, page 34

SPC/E extended simple point charge, page 32

TDDFT time-dependent density functional theory, page 6

TDSE time-dependent Schrödinger equation, page 7

TISE time-independent Schrödinger equation, page 7

VVP velocity-Verlet propagator, page 10

XC exchange-correlation, page 12

Attached papers

This appendix contains the published papers comprising this thesis. They appear in the same order as in chap. 3.

I F. Uhlig, O. Marsalek, and P. Jungwirth. From a localized H_3O radical to a delocalized $H_3O^+ \cdots e^-$ solvent-separated pair by sequential hydration. *Phys. Chem. Chem. Phys.*, 13:14003–14009, 2011.

II F. Uhlig and P. Jungwirth. Embedded cluster models for reactivity of the hydrated electron. *Z. Phys. Chem.*, 227(9-11):1583–1593, 2013.

III F. Uhlig, O. Marsalek, and P. Jungwirth. Unraveling the complex nature of the hydrated electron. *J. Phys. Chem. Lett.*, 3(20):3071–3075, 2012.

IV F. Uhlig, O. Marsalek, and P. Jungwirth. Electron at the surface of water: Dehydrated or not? *J. Phys. Chem. Lett.*, 4(2):338–343, 2013.

V R. Vácha, F. Uhlig, and P. Jungwirth. Charges at aqueous interfaces: Development of computational approaches in direct contact with experiment. *Adv. Chem. Phys.*, 155:69–96, 2014.

VI F. Uhlig, J. M. Herbert, M. P. Coons, and P. Jungwirth. Optical spectroscopy of the bulk and interfacial hydrated electron from ab initio calculations. DOI: 10.1021/jp5004243

VII J. Savolainen, F. Uhlig, S. Ahmed, P. Hamm, and P. Jungwirth. Direct observation of the collapse of the delocalized excess electron in water. *accepted for publication in Nature Chem.*